TIP TRAJECTORY TRACKING OF

FLEXIBLE-JOINT MANIPULATORS

A Thesis Submitted to

the College of Graduate Studies and Research

In Partial Fulfillment of the Requirements

For the Degree of Doctor of Philosophy

In the Department of Mechanical Engineering

University of Saskatchewan

Saskatoon

By

HAMID SALMASI

PERMISSION TO USE

In presenting this thesis in partial fulfilment of the requirements for a postgraduate degree from the University of Saskatchewan, I agree that the Libraries of this University may make it freely available for inspection. I further agree that permission for copying of this thesis in any manner, in whole or in part, for scholarly purposes may be granted by the professor or professors who supervised my thesis work or, in their absence, by the Head of the Department or the Dean of the College in which my thesis work was done. It is understood that any copying or publication or use of this thesis or parts thereof for financial gain shall not be allowed without my written permission. It is also understood that due recognition shall be given to me and to the University of Saskatchewan in any scholarly use which may be made of any material in my thesis.

Requests for permission to copy or to make other use of material in this thesis in whole or part should be addressed to:

Head of the Department of Mechanical Engineering

College of Engineering, University of Saskatchewan

Saskatoon, Saskatchewan, Canada S7N 1L5

ABSTRACT

In most robot applications, the control of the manipulator's end-effector along a specified desired trajectory is the main concern. In these applications, the end-effector (tip) of the manipulator is required to follow a given trajectory. Several methods have been so far proposed for the motion control of robot manipulators. However, most of these control methods ignore either joint friction or joint elasticity which can be caused by the transmission systems (e.g. belts and gearboxes). This study aims at development of a comprehensive control strategy for the tip-trajectory tracking of flexible-joint robot manipulators. While the proposed control strategy takes into account the effect of the friction and the elasticity in the joints, it also provides a highly accurate motion for the manipulator's end-effector.

During this study several approaches have been developed, implemented and verified experimentally/numerically for the tip trajectory tracking of robot manipulators. To compensate for the elasticity of the joints two methods have been proposed; they are a *composite controller* whose design is based on the singular perturbation theory and integral manifold concept, and a *swarm controller* which is a novel biologically-inspired controller and its concept is inspired by the movement of real biological systems such as flocks of birds and schools of fishes. To compensate for the friction in the joints two new approaches have been also introduced. They are a composite compensation strategy which consists of the non-linear dynamic LuGre model and a Proportional-Derivative (PD) compensator, and a novel friction compensation method whose design is based on the Work-Energy principle. Each of these proposed controllers has some

ii

advantages and drawbacks, and hence, depending on the application of the robot manipulator, they can be employed. For instance, the Work-Energy method has a simpler form than the LuGre-PD compensator and can be easily implemented in industrial applications, yet it provides less accuracy in friction compensation. In addition to design and develop new controllers for flexible-joint manipulators, another contribution of this work lays in the experimental verification of the proposed control strategies. For this purpose, experimental setups of a two-rigid-link flexible-joint and a single-rigid-link flexible-joint manipulators have been employed. The proposed controllers have been experimentally tested for different trajectories, velocities and several flexibilities of the joints. This ensures that the controllers are able to perform effectively at different trajectories and speeds.

Besides developing control strategies for the flexible-joint manipulators, dynamic modeling and vibration suppression of flexible-link manipulators are other parts of this study. To derive dynamic equations for the flexible-link flexible-joint manipulators, the Lagrange method is used. The simulation results from Lagrange method are then confirmed by the finite element analysis (FEA) for different trajectories.

To suppress the vibration of flexible manipulators during the manoeuvre, a collocated sensor-actuator is utilized, and a proportional control method is employed to adjust the voltage applied to the piezoelectric actuator. Based on the controllability of the states and using FEA, the optimum location of the piezoelectric along the manipulator is found. The effect of the controller's gain and the delay between the input and output of the controller are also analyzed through a stability analysis.

ACKNOWLEDGMENTS

DEDICATIONS

This thesis is dedicated to my father Reza Salmasi, my mother Fatemeh Y. Panah and my dear wife Haleh Salmasi.

COPYRIGHT PERMISSION OF THE PAPERS

At the time of the publication of this thesis, a paper "A biologically-inspired controller for tip trajectory tracking of flexible-joint manipulators" (Chapter 4), is under review. Other papers are accepted/published, and permissions to reprint these papers have been sought from the publisher through email or from the website of the publishers.

Permission to include paper "Tip trajectory tracking of flexible-joint manipulators driven by harmonic drives" authored by H. Salmasi, R. Fotouhi, and P. N. Nikiforuk, and was originally published in IASTED International Journal of Robotics and Automation, Vol. 24, No. 2, 2009.

Hamid Salmasi

From: Calgary [Calgary@iasted.org]
Sent: July-15-09 1:49 PM
To: 'Hamid Salmasi'
Subject: RE: Permission to use the IJRA paper

Please feel free to reuse the material. We ask that you include some acknowledgement of IASTED's right to the original paper.

Nicholas Woodard
Publications Coordinator
IASTED and ACTA Press
B6, 101 - 2509 Dieppe Avenue SW
Calgary AB T3E 7J9
CANADA

From: Hamid Salmasi [mailto:hamid.salmasi@usask.ca]
Sent: Monday, July 13, 2009 8:53 AM
To: publish
Subject: Permission to use the IJRA paper

Dear Sir/Madam,

I am the author of the paper "TIP TRAJECTORY TRACKING OF FLEXIBLE-JOINT MANIPULATORS DRIVEN BY HARMONIC DRIVES" (paper No. 206-3283), accepted for publication at "Int. journal of robotics and automation".

I am now writing my PhD dissertation and would appreciate if you give me the permission to have this paper as a part of my PhD thesis.

Hamid Salmasi,

PhD student
Robotic Laboratory
Mechanical Engineering Department
University of Saskatchewan, Saskatoon, SK, Canada
Phone: (306) 966-5817
Fax: (306) 966-5427
Email:hamid.salmasi@usask.ca

Permission to include paper "A manoeuvre control strategy for flexible joint manipulators with joint dry friction" authored by H. Salmasi, R. Fotouhi, and P. N. Nikiforuk, and to be published in the Cambridge journal of Robotica, (doi:10.1017/S0263574709990373).

Permission to reprint the paper "Vibration control of a flexible link manipulator using smart structure" authored by H. Salmasi, R. Fotouhi, and P. N. Nikiforuk, and originally was published in the Proceedings of the International Federation of Automatic Control (IFAC) World Congress, Seoul, South Korea, p 11787-11792. The following statement has been copied from the website of Elsevier Ltd.[1], the official, sole publisher of IFAC publications, on September 3, 2009.

> *"As an author, you retain rights for a large number of author uses, including use by your employing institute or company. These rights are retained and permitted without the need to obtain specific permission from Elsevier. These include:*
>
> *... the right to include the article in full or in part in a thesis or dissertation (provided that this is not to be published commercially);"*

Permission to reprint paper "Dynamic modeling of a manipulator with flexible links and flexible joints" authored by H. Salmasi, R. Fotouhi, and P. N. Nikiforuk, and published in the Proceedings of 21st Canadian Congress of Applied Mechanics, Ryerson University, Toronto, ON, Canada, June 3-7, 2007, (CD Rom). The following statement has been copied from the first page of the proceedings.[2]

> *"Reprints from this publication may be made provided credit is given to the authors and the reference made to the Proceedings of 21st Congress of Applied Mechanics, Ryerson University, Toronto, Ontario, Canada, 2007 (CANCAM 2007)."*

---

[1] http://www.elsevier.com/wps/find/supportfaq.cws_home/rightsasanauthor (accessed September 9, 2009).

[2] http://www.ryerson.ca/cancam07/Proceedings.pdf (accessed September 12, 2009).

TABLE OF CONTENTS

TABLE OF FIGURES

Chapter 1:

Chapter 4:

Chapter 1.   Introduction

The first chapter of thesis provides a brief background regarding flexible robot manipulators, the research objectives and a summary of the papers included in this thesis. Out of this study eleven research papers have been submitted/published in technical journals and the proceedings of international conferences [1]-[11]. However, because of the need for brevity, only five of these papers have been included in the following Chapters 2-6.

1.1 Background

The concept of robotics came from "Robota", meaning serf labour. This concept was first introduced by a science fiction author, Karel Capek, in his play *Rosum's Universal Robots* where it was used to refer to autonomous capable of performing a range of human activities [12]. After about a century, robots are now utilized almost everywhere: oceans, factories, hospitals and even on Mars. An important class of robots are robot manipulators that are employed in a variety of tasks, from automotive industries to aerospace applications. As shown in Fig. 1, a robot manipulator generally includes four main components:

i. Links: ideally links can be considered rigid for slow motion and small interacting forces. However, for links with a small width-length ratio, the flexibility must be considered in both dynamic modeling and control of these manipulators.

ii. Actuators: the motors, hydraulic or pneumatic pistons or other elements that cause the links to move are called actuators [13].

iii. Joints: transmission systems such as belts and gearboxes which connect the links to the actuators.

iv. End-effector: the end part of the manipulator that interacts with the environment. For instance it can be a gripper, welding tool, etc.
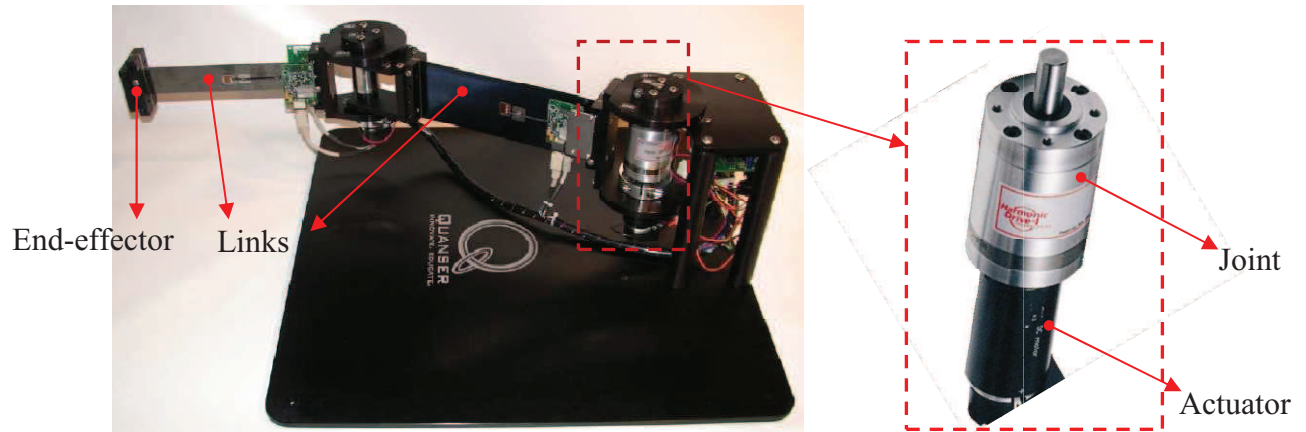
Fig. 1. Components of a two-link robot manipulator

The motion of the end-effector is controlled through the torques applied by the actuators to the links. Therefore, to move the end-effector along a desired path, a controller is required to adjust the torques applied by the motors. In the case that the body of the robot (links and joints) is rigid, the design of the controller will not be very complicated, and a large number of control strategies have been proposed to control the rigid robot manipulators. However, in reality flexibility exists in two components of the robot manipulators: links and joints. For manipulators that have links with a slender design and lightweight material, the flexibility of the links must be considered in the dynamics and control procedure. The flexibility of the joints is produced by the motion transmission/reduction systems such as the belts and harmonic drives.

Recent studies have shown that the joint flexibility has a significant effect on the performance of industrial robot manipulators [14-18]. This effect becomes more important in robot applications in which high-precision is required in the performance of the manipulator [19-23]. For instance, many robots use a harmonic drive as the transmission system to increase the applied torque to the links [24]. Harmonic drives are fascinating to designers due to their high torque transmissibility and small size [25-26]. However, torsional elasticity in flexible parts

of harmonic drives produces undesired oscillations during the performance of the manipulator. Therefore, for robot manipulators driven by harmonic drives, it is necessary to take into account the effect of the flexibility of the joints in the design procedure of the controller. On the other hand, considering flexibilities in the joints contributes to complexity in the dynamics and control of the manipulator. The main complexity is due to the fact that flexible-joint manipulators are under-actuated; that is, the number of actuators is lower than the degrees of freedom. Several controller strategies have been proposed so far to overcome the difficulty of under actuation in flexible-joint manipulators; however, important factors such as joint friction and inertia of the rotors are ignored in these control methods. This deteriorates the performance of the controller and affects the accuracy of the end-effector motion. Therefore, a more comprehensive method which considers different aspects of dynamics and control of flexible-joint manipulator is needed especially in robots performing high-speed high-precision tasks.

1.2   Research objectives

This thesis aims to develop a comprehensive control strategy for the flexible-joint (elastic-joint) manipulators. The controller must take into account the flexibility and friction in the joints, while it provides a precise motion for the manipulator's end-effector. Besides the control of flexible-joint manipulators, dynamic modeling of flexible-link flexible-joint and vibration suppression of flexible-link manipulators are other objectives of this research. Therefore, the objectives of this research can be summarized as follows:

1- Precise tip trajectory tracking of flexible-joint manipulators during and at the end of manoeuvre (Chapters 2, 3 and 4)

2- Friction compensation in harmonic drives (Chapters 2 and 3)

3- Experimental validation of the proposed controller for flexible-joint manipulators

(Chapters 2, 3 and 4)

4- Vibration suppression of flexible-link manipulators using piezoelectric actuators

(Chapter 5)

5- Dynamic modeling of flexible-link flexible-joint manipulators (Chapter 6)

A summary of the methodologies used to accomplish these objectives is explained in Section 1.3. The details of these approaches can be found in Chapters 2-6.

Remark: Because of the manuscript nature of this thesis, equations, figures and references might be repeated in the thesis.

1.3   Summary of manuscripts

The papers published or submitted by the candidate are cited in the reference list [1]-[11]. For brevity, five of these papers have been selected and explained in this thesis.

The first three papers, given in Chapters 2-4, describe different control strategies used for the tip trajectory tracking of the flexible-joint manipulators. In these control strategies, the controller had two parts: the first part was designed to compensate for the flexibility of the joints, and the second part was to compensate for the joints' friction. Different combinations of these controllers were examined and experimentally verified. Table 1 shows the structure of the proposed controllers. The performance of these controllers was tested using the experimental setups of a single-rigid-link flexible-joint (SRLFJ), shown in Fig. 2, and a two-rigid-link flexible-joint manipulator (TRLFJ), shown in Fig. 3, available at the Robotics Laboratory of the University of Saskatchewan.

Table 1. Different control strategies employed and experimentally verified for flexible-joint manipulators

Controller components	Explained in
Composite controller based on the SPT*+ LuGre-PD friction compensator	Chapter 2
Composite controller based on the SPT*+ friction compensator based on Work-Energy method	Chapter 3
Swarm controller+ LuGre-PD friction compensator	Chapter 4

*SPT: Singular Perturbation Theory
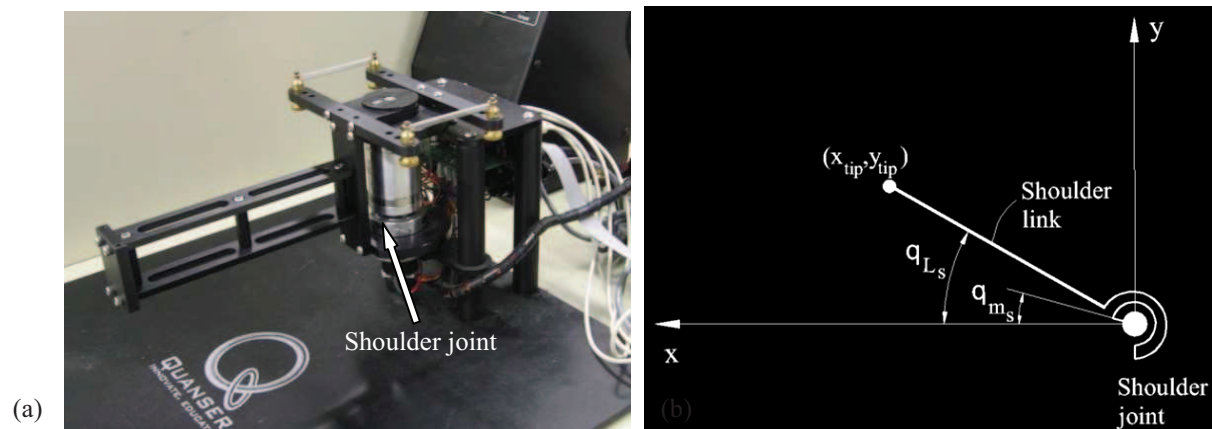
(a)   (b)

Fig. 2. (a) Experimental module of the single rigid-link flexible-joint manipulator available in the Robotics Laboratory of the University of Saskatchewan, (b) schematic of the top-view of the experimental setup showing the angles of the joint and the link (subscripts s stands for shoulder)
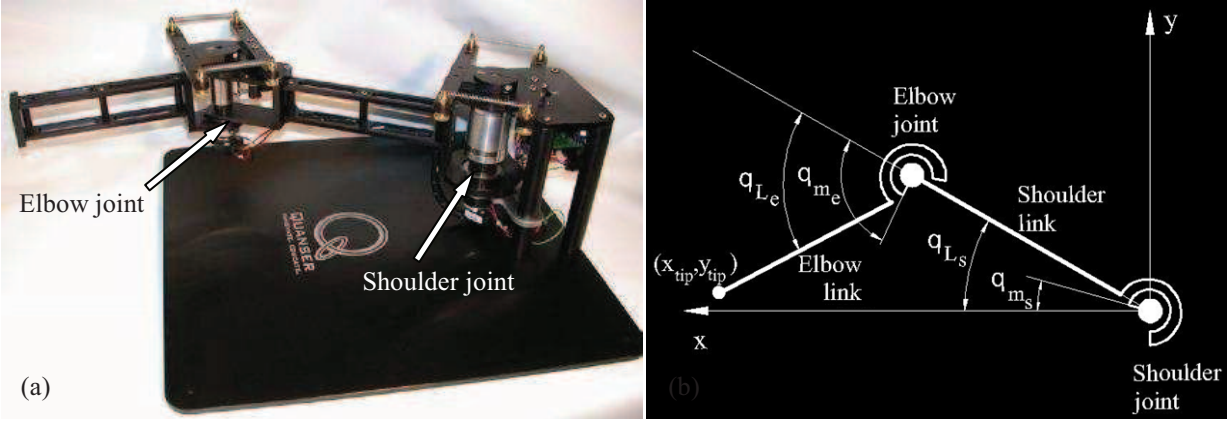
Fig. 3. (a) Experimental module of the two-rigid-link flexible-joint manipulator available in the Robotics Laboratory of the University of Saskatchewan, (b) schematic of the top-view of the experimental setup showing the angles of the joints and the links (subscripts e and s stand for elbow and shoulder, respectively)

To validate the developed control strategies, approximately 120 experiments were performed at different temperatures, humidities, flexibilities (elasticity) of the joints, trajectories and velocities. It is noteworthy that the experimental verification was an indication that the proposed controllers can be implemented in the applications. A list of the experiments carried out using the experimental setup of the SRLFJ can be found in Appendix I. In total, the results of 57 experiments were recorded for the SRLFJ, some of which are presented in Chapter 3. Three friction compensation strategies, the LuGre method, work-energy method, and LuGre-PD method, were examined at four different desired trajectories, and for low and high flexibilities of the joint ($K = 3.93\,N.m$ and $K = 10.33\,N.m$). Based on the experimental results, it was concluded that the best controller was a combination of the composite controller to compensate for the flexibility of the joints and the LuGre-PD method to compensate for the friction. This strategy was then employed to control the TRLFJ shown in Fig. 3a.

For the TRLFJ, the experiments were carried out using the composite and swarm controllers along with the LuGre-PD method. Some of these experimental results are given in Chapters 2 and 4, and also in [4]. The list of these experiments is given in Appendix I.

The paper included in Chapter 5 describes the application of a piezoelectric actuator to suppress the vibration of a flexible-link manipulator. This method has been used for vibration suppression of a cantilever beam and a single-link flexible link manipulator. The fifth paper, given in Chapter 6, presents the dynamic modeling of flexible-link flexible-joint manipulators. Lagrange's method along with the assumed mode shapes method is employed to derive the dynamic equations. The simulation results are then verified by finite element analysis. The following sections give more details of each paper presented in Chapters 2-6.

1.3.1 Tip trajectory tracking of flexible-joint manipulators driven by harmonic drives

In this paper, a new control strategy has been proposed for the tip trajectory tracking of flexible-joint manipulator [1]. The motion control of the end-effector of the manipulator is the main concern in most robot applications, such as spacecraft and automotive industries. In these applications, a desired trajectory is usually specified in the task-space and the robot tip (end-effector) is required to follow this prescribed trajectory. A mapping is first determined between the location of the robot end-effector and the rotations of the joints, and based on the desired trajectory of the end-effector, the desired rotations of the joints are computed. A control approach is then designed such that the error between rotations of the joints and their desired trajectories are minimized.

The proposed control strategy in [1] had two main advantages compared with other controllers developed for the tip trajectory tracking of robot manipulators. These advantages were: (a) taking into account the flexibility of the joints, (b) considering the effect of the joints'

friction. The control strategy was a two-part controller. The first part was a composite controller to compensate for the flexibilities of the joints, and the second part was a friction compensation torque to compensate for the friction in the joints. The following describes these two parts of the controller.

The first part of the controller was developed using singular perturbation theory along with the integral manifold concept. As discussed in Section 1.1, the main problem in the trajectory tracking of flexible joint manipulators was that these systems were under-actuated. A serial flexible joint manipulator with *n* links had *2n* degrees of freedom, *n* motor rotations and *n* link rotations, while it had only *n* actuators which were the motor torques. Employing the singular perturbation theory allowed for the dividing of the dynamics of flexible-joint manipulator into two subsystems: one corresponding to the fast dynamics (high frequency vibration due to flexibility) and the other to the slow dynamics (low-frequency motion). For each of these subsystems, a controller was then designed.

The second part of the proposed control strategy was to compensate for the friction in the joints. Two methods were developed in this research for friction compensation. In the first method, a linear feed-forward torque was designed using the Work-Energy principle [2]. This method was easy to implement and did not need any feedback from the system. However, it could not model such friction characteristics as the Stribeck effect. To overcome the disadvantages of the Work-Energy method, a more general friction compensating strategy was proposed. This compensating torque was a combination of a torque identified based on the LuGre method[3] and a PD compensator. To identify the friction in the joints based on the LuGre

---

[3] The LuGre model is a comprehensive friction model developed based on the deflection of the microscopic asperities of the rubbing surfaces. In this thesis, a simplified form of this model was obtained for the steady-state

method, 57 tests were carried out to determine the friction at different velocities. By interpolating

the data, the friction torques were obtained as functions of the velocity. The experimental data

and the estimated functions for the shoulder and the elbow joint motors, are shown Fig. 4.
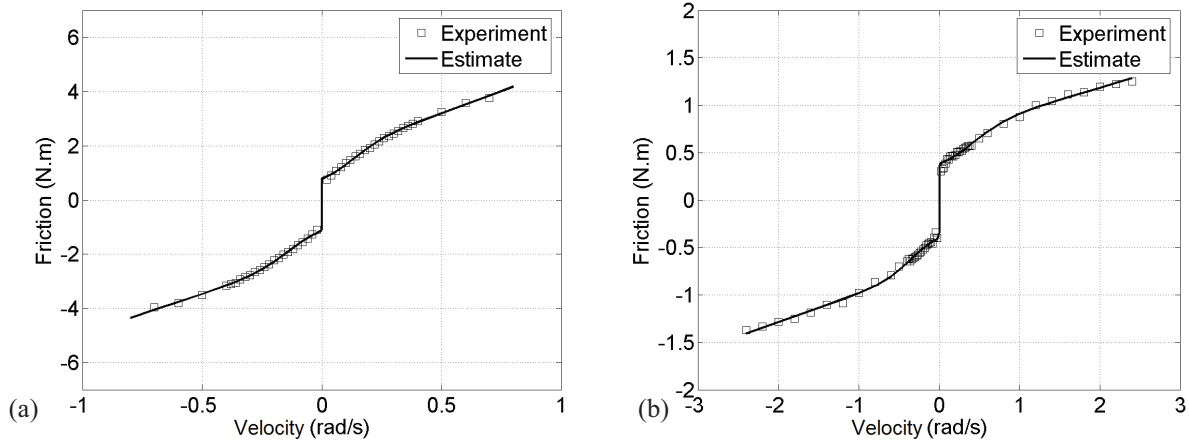
Fig. 4. Experimental results obtained for steady state conditions and estimation function obtained

based on the LuGre model for (a) shoulder joint motor, (b) elbow joint motor

In ideal situations, the counterbalancing estimated joint friction torque shown in Fig. 4

was equal to the real friction of the joints, and, hence, the friction of the joints would be

compensated completely. However, practically there was always some error in the estimation of

joint friction torque, for example due to change in the oil temperature, load, humidity and

actuator wear. To remove this error, a PD compensator along with the friction torque based on

the LuGre method was used. Therefore, the friction compensating torque τ_f was

$$\tau_f = \tau_{f_L} + K_d(\dot{q}_d - \dot{q}_m) + K_p(q_d - q_m) \tag{1}$$

where τ_{f_L} was the joint friction torque identified based on the LuGre method. Parameters K_d

and K_p were the gains of the PD compensator, and q_d and $\dot{q}_d$ were, respectively, the desired

conditions and employed to estimate the friction of the joints. For brevity, the simplified LuGre model obtained for

the steady-state conditions is referred to as the LuGre model in this thesis.

trajectory and its derivative. The first term of the friction compensating torque in (1) was identified based on the LuGre model. The schematic of the entire friction compensation strategy which incorporated a PD compensator combined with the LuGre friction model is shown in Fig. 5. It was experimentally found that the friction was successfully compensated for by employing the proposed friction compensating, though it led to a steady-state error at the end of the manoeuvre. This steady-state error in the friction compensation was bounded according to a stability analysis carried out based on the Lyapunov theory [4]. Also, it was shown that the range of the steady-state error was dependent on the friction parameters and gain controllers.
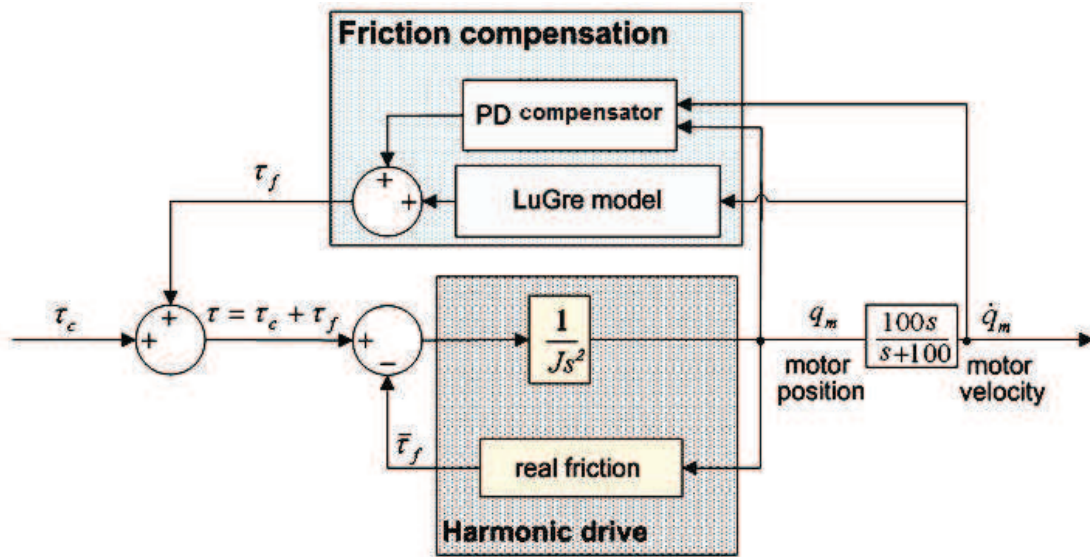
Fig. 5. Model based friction compensation strategy used for experimental setup of two-rigid-link flexible-joint manipulator

The experimental setup used for verification is shown in Fig. 3. As shown in this figure, the first link (shoulder link) was coupled to the first joint (shoulder joint) by means of a flexible joint. At the end of the shoulder link a second harmonic drive was connected to the elbow link via the flexible elbow joint. Also, in Fig. 3 angles   and   were rotations of the shoulder

and elbow motors[4], and angles q_{l_s} and q_{l_e} were rotations of the shoulder and elbow links, respectively. Both motors and both flexible joints were instrumented with quadrature optical encoders whose resolutions were 0.0015 *rad/count* [27]. The experimental results indicated the superiority of the proposed control strategy compared to other typical controllers such as inverse dynamics torque control. For instance, as shown in Fig. 6, the tracking error between actual and desired rotations of the shoulder and elbow links was almost zero when the composite controller was used for two different types of trajectory. The desired trajectories for the shoulder and elbow links were ninth order and third order polynomials, respectively.
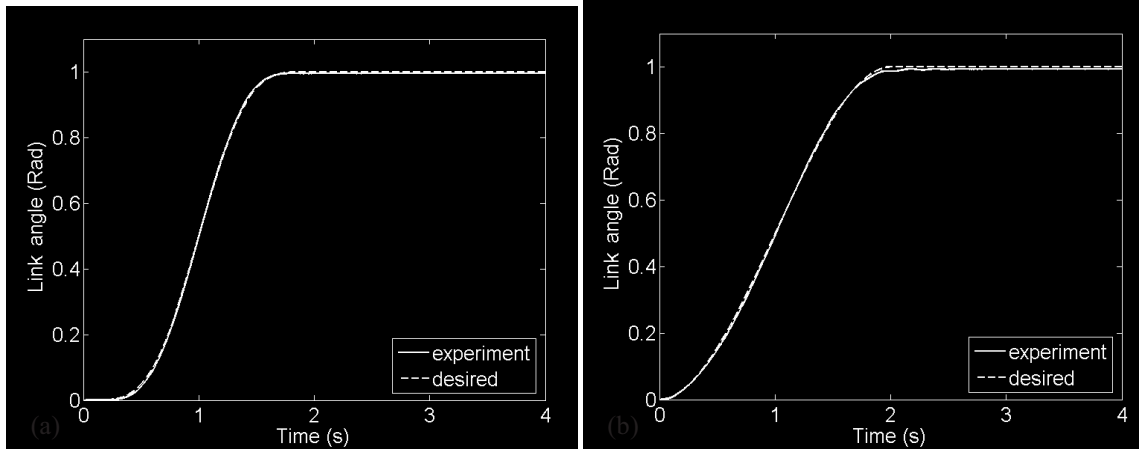
Fig. 6. Experimental verification of the links' rotations for $[q_{f_s}, q_{f_e}]_1 = [1.0\,rad, 1.0\,rad]$ and $[K_s, K_e] = [7.93\,N \cdot m/rad, 2.94\,N \cdot m/rad]$ using the composite controller, (a) shoulder link (b) elbow link trajectory.

1.3.2 A manoeuvre control strategy for flexible joint manipulators with joint dry friction

Chapter 3 presents another control strategy for the tip trajectory tracking of flexible-joint manipulators [2]. The first part of this control strategy was similar to the composite controller developed for the control of TRLFJ manipulator and explained in the previous section. The

---

[4] Subscripts e and s stand for elbow and shoulder, respectively.

second part of the control strategy was a novel friction compensating torque whose design was based on the Work-Energy principle. Compared to the LuGre friction model described in the previous section, the Work-Energy method had several advantages. The LuGre friction torque was obtained based on the assumption of steady-state conditions. Therefore, the pre-sliding regime in which stick-slip motion occurred at very low velocities was not modelled in the LuGre model. Another disadvantage of the LuGre model was that the stiction was assumed to be the same at the beginning and end of the motion of the manipulator, while in practice the stiction at the beginning of the manoeuvre was usually greater than that of at the end. In the LuGre model, and most friction models developed to predict the joint friction, an experimental identification procedure was necessary to determine the friction model parameters. This identification procedure involved several experiments which needed to be carried out at different velocities and required a considerable amount of time. However, the friction compensating torque based on the Work-Energy principle could be identified in only two steps and, hence, the proposed model was more cost-effective in terms of the experimental time required to identify the parameters of the controller.

According to the Work-Energy principle, the work done during the motion of the flexible joint robot manipulator included the work done by the motor torque, W_I, the energies dissipated by the viscous damping, W_d, and the Coulomb friction torque, W_{df}. The total work done by the output controller was composed of two parts, the work of the composite controller torque τ_c, which is W_{I_c}, and the work of the compensating torque of dry friction τ_{fd}^{WE}, which was W_{I_f}. These works were written as

$$W_I = \int_0^{\theta_f} \tau \, dq_m = \int_0^{t_f} \tau \, \dot{q}_m \, dt = \int_0^{t_f} (\tau_c + \tau_{fd}^{WE}) \dot{q}_m \, dt = \int_0^{t_f} \tau_c \dot{q}_m \, dt + \int_0^{t_f} \tau_{fd}^{WE} \dot{q}_m \, dt = W_{I_c} + W_{I_f} \quad (2)$$

where θ_f and t_f were the final rotation of the joint and the time at which link reached its final position, respectively. The energy dissipated by the viscous damping was $W_d = \int_0^{\theta_f} c_m \dot{q}_m \, dq_m = \int_0^{t_f} c_m \dot{q}_m^{\,2} \, dt$ and the energy dissipated by the dry Coulomb friction, τ_{fc}, was $W_{df} = \int_0^{\theta_f} \tau_{fc} \, dq_m = \int_0^{t_f} \tau_{fc} \dot{q}_m \, dt$. The principle of work and energy for a general system was

$$K_2 = \sum W_{1 \to 2} + K_1 \tag{3}$$

where $\sum W_{1 \to 2}$ expressed the total work done by the forces (conservative and non-conservative) on the system from the initial position 1 to the final position 2, and K_1 and K_2 were the total kinetic energy of the system at the initial and final positions, respectively. Since the velocity was zero at the initial and final positions, K_1 and K_2 were zero and equation (3) reduced to $\sum W_{1 \to 2} = 0$, and thus

$$\sum W_{1 \to 2} = W_{I_c} + W_{I_f} - W_d - W_{df} = 0 \tag{4}$$

From (4), the work done by τ_{fd}^{WE} was obtained as

$$W_{I_f} = -W_{I_c} + W_d + W_{df} \tag{5}$$

and therefore,

$$\int_0^{t_f} \tau_{fd}^{WE} \dot{q}_m \, dt = -W_{I_c} + W_d + W_{df} \tag{6}$$

The friction compensating torque, τ_{fd}^{WE}, was then determined from (6). There were many candidates for the friction compensating torque function which satisfied (6). For convenience, the friction compensating torque was assumed to be linear; that is

$$\tau_{fd}^{WE} = \begin{cases} a + bt & 0 < t < -(a/b) \\ 0 & t > -(a/b) \end{cases} \tag{7}$$

Thus, equation (6) became

14

$$\int_0^{t_f} (a + bt)\,\dot{q}_m\,dt = -W_{I_c} + W_d + W_{df} \tag{8}$$

Parameter a was the torque required to overcome the stiction and initiate the motion of the manipulator from the rest position. This parameter, referred to as the breakaway force, was obtained experimentally by increasing the torque gradually, until the manipulator started to move. Once the parameter a was identified, the parameter b was computed using equation (8) and the friction torque was determined in (7).

The proposed controller was verified using the experimental setup of a single rigid-link flexible-joint manipulator shown in Fig. 2. According to the experimental results, the controller was successful in the tip trajectory tracking such that the tracking error during and at the end of the manoeuvre was found to be small. The experimental results are given in Chapter 3.

1.3.3 A biologically-inspired controller for tip trajectory tracking of flexible-joint manipulators

In Chapter 4 a novel biologically-inspired controller is introduced for the tip trajectory tracking of the manipulators [3]. The main concept of this controller was inspired by real biological systems. Populations such as swarms of birds or schools of fish often move in coordinated but localized efforts toward a particular target [28]. In fact, by simply adjusting the trajectory of each individual toward its own best location the swarm finds its best position at each time step [29]. For instance, when a swarm of birds (or a school of fish) is moving towards a specific destination, each bird (or fish) has to follow a desired path so that the entire group moves towards the target. As shown in Fig. 7, the movement of a flock of birds (or a school of fishes) can be modelled as a group of particles that moves from an initial location (origin) towards a specified destination. Each bird (or fish) is symbolically modelled by a particle, and the center of the swarm is located at the center of the group. The swarm's center can be easily

15

found as the average of the positions of the particles in the space; that is $X = \sum_{i=1}^{n} x_i/n$ and $Y = \sum_{i=1}^{n} y_i/n$ where (X, Y) denotes the Cartesian coordinate of the swarm's center, (x_i, y_i) denotes each particle's location and n is the number of particles (e.g. $n = 8$ for the model of Fig. 7). The local error is defined as the error between the actual path of each particle and its desired path, and the global error shows the deviation of the group from its desired path. Each particle has a memory and intelligence and, hence, is able to correct its position such that the local and global errors are minimized during the motion of the swarm. Therefore, the swarm movement can be resembled by an optimization problem in which the objective function constitutes the local and the global errors. The optimum movement is achieved when the objective function is minimized.
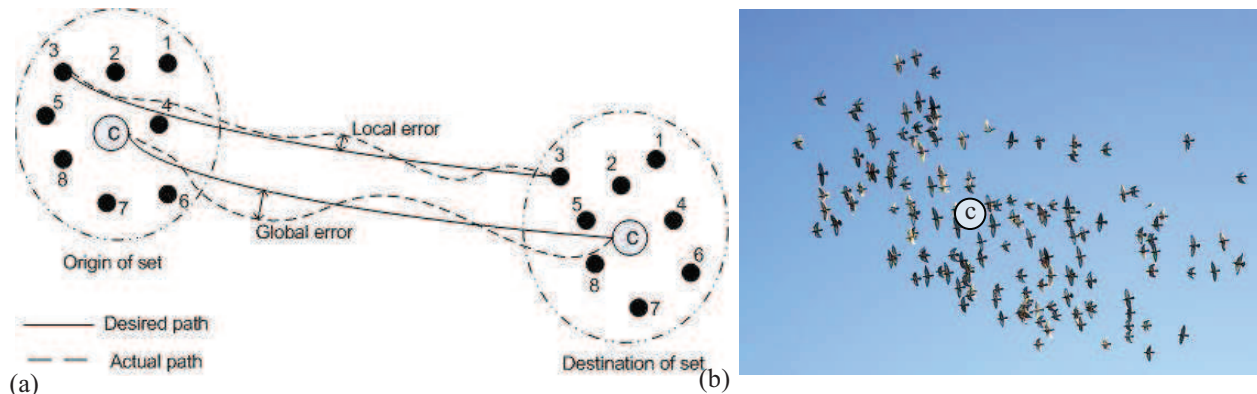
Fig. 7. (a) Schematic of a swarm movement; each particle is shown by a solid circle (b) an actual swarm of birds; the centre of the swarm is denoted by c.

In this research study, the concept of swarm movement was applied to control the flexible-joint manipulators. For this purpose, each link was represented by a particle and the robot end-effector was represented by the swarm's center. For the tip trajectory tracking, each link (particle) had to move along its desired path so that the end-effector (swarm's center) could follow the swarm desired trajectory. Therefore, the local error was defined as the difference between the rotation of each link and its desired rotation and the global error was the difference

16

between the position of the end-effector and its desired position. The block-diagram of the swarm control scheme is shown in Fig. 8 which consisted of four principle parts:

1-Variable-gain PID controller: In this component, the applied torques to the motors were evaluated using the following equation

$$\tag{9}$$

where , and were, respectively, the derivative, proportional and integrative gains of the PID controller, and the difference between the rotation of each link and its desired rotation. The main reason to choose the PID controller to compute torque was due to its simplicity and clear physical meaning. Especially, in industrial applications, simple controllers are preferred to complex controllers, if the performance enhancement by employing complicated control methods are not significant enough [13].

2- Gain generator: This component produced proportional, derivative and integrative gains every time-step.

3- Memory: After computing gains in the gain generator, they were stored in a memory. These values were then employed in the gain generator in the next time-step to evaluate proportional, derivative and integrative gains.

4- Error evaluator: In this component, local errors (links' errors) and global error (end-effector-error) were calculated based on the feedback signals of link rotations.
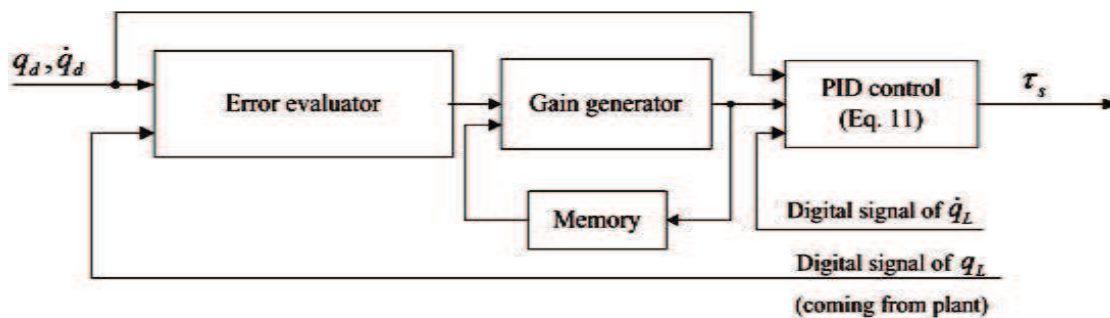
Fig. 8. Block diagram of the swarm torque controller for the tip-trajectory tracking of flexible-joint manipulators

17

The key advantage of this control strategy was that the positions of the joints and the robot end-effector were controlled simultaneously. In most controllers developed for the flexible-joint manipulators, the joints were controlled separately, and the error in the end-effector position was not taken into account in the control procedure. Therefore, it was possible that while the error in the joint rotations was kept small, the error at the end-effector position became very significant. This could happen for serial robot manipulators, because the end-effector position was a trigonometric function of the joints position, and not a linear function of the rotations of the joints.

To verify the proposed approach, the experimental setup of the TRLFJ manipulator shown in Fig. 3 was employed. The experimental results indicated that the controller was successful in the tip trajectory task for different final rotations and different manipulation speeds. An experimental comparison between the swarm controller and a typical controller used for rigid robots, inverse dynamic torque control, demonstrated the superiority of the proposed swarm control strategy. Furthermore, to analyze the effects of the initial gains of the time-variable-gain controller, a sensitivity analysis was experimentally performed and it was shown that tracking and the steady-state errors did not change significantly for different initial gains of the controller. The details of the swarm control strategy and the corresponding experimental results are given in Chapter 4.

1.3.4 Vibration suppression of a flexible link manipulator using piezoelectric actuator

The active vibration suppression of a flexible link manipulator using a smart structure (piezoelectric actuator) is presented in Chapter 5 and [8]. The control strategy was a proportional control scheme in which the applied voltage to the piezoelectric actuator was adjusted based on the deflection of the manipulator so that the vibration of the beam was suppressed. One of the

advantages of this control method was that in contrast to many other controllers developed for vibration suppression of flexible link manipulators, the proposed control strategy was a velocity-free scheme and used only position as the feedback. It noteworthy that velocity measurement is generally not desirable as most flexible manipulators have only strain gauges to measure the deflection along the beam [30]. Also, taking the derivative from the position signal to obtain the velocity signal was not a good approach since it resulted in generating noise in the velocity signal which deteriorated the performance of the controller.

A finite-element model was first developed for a cantilever beam with a piezoelectric actuator. To start the simulation, the beam was deflected one centimetre from its horizontal position, and then it was released from its deflected position. Since the piezoelectric actuator was inactive, and the effect of the material damping was not considered in modeling procedure[5], the beam oscillated with a constant amplitude. The piezoelectric actuator was then activated, and the applied voltage to the piezoelectric actuator was adjusted proportionally to the deflection of the beam. The deflection of the beam was measured using a sensor placed at the location of the piezoelectric actuator. The actuator and sensor were located at the same location to avoid instability due to the non-collocation of sensor and actuators [31]. It was shown in [32] that non-collocation of the sensor and actuator can lead to the instability of the controller. The simulation results for the cantilever beam indicated that the piezoelectric actuator was very successful in

---

[5] The material damping was ignored so that the effect of the piezoelectric actuator in vibration suppression was only analyzed. Otherwise, the vibration was suppressed due to both piezoelectric actuator performance and the material damping, and it was not possible to determine which portion of the vibration was eliminated because of piezoelectric actuator.

vibration suppression of the cantilever beam such that the amplitude of vibration was reduced from one centimetre at the beginning to two millimetres after one second.

Finding the optimum placement of the piezoelectric actuator along the cantilever beam was another part of this study. The best location was found based on the controllability of the system states and using FE analysis. To determine the optimum location in FE, two criteria were defined based on the deflection of the beam as given in equations (14)-(15) in Chapter 5. The simulation results showed that the piezoelectric actuator had the best performance when it was located at $\frac{L_s}{L_b} = 0.3$ where L_s was the distance of the piezoelectric from the base of the manipulator and L_b was the length of the link (See Fig. 9). The optimum placement of the piezoelectric was then validated based on the controllability of the system states.

The control method was then extended to suppress the vibration the flexible-link manipulator shown in Fig. 9. The simulation results indicated that the piezoelectric actuator was successful in suppressing the oscillations of the manipulator during and after the manoeuvre. For instance, as shown in Fig. 10, the deflection of the manipulator was reduced considerably by employing the piezoelectric actuator with controller's gain $K_c = 4 \times 10^5$, and when the piezoelectric actuator was located at $\frac{L_s}{L_b} = 0.3$.

The effect of the controller's gain on the performance of the piezoelectric actuator was also analyzed. To determine the best controller's gain, four different evaluation criteria were used. Three of these criteria, E_{0-4}, E_{0-1} and E_{1-4}, were based on the deflection of the manipulator, and defined respectively for the total manoeuvre time ($0 < t \leq 4$), before the manipulator reached the final rotation ($0 < t \leq 1$), and after the manipulator reached its final rotation ($1 < t \leq 4$). The fourth criterion was defined based on the amplitude of the dominant frequencies contributing in the deflection response. This criterion was determined from the

Power Spectrum Density (PSD) of deflection responses for different gains. According to these four criteria, the best performance was obtained when the controller's gain was   . The details of this approach are given in Chapter 5 and in the paper published in the WIT Transactions on the Built Environment: Computer Aided Optimum Design in Engineering X [9].
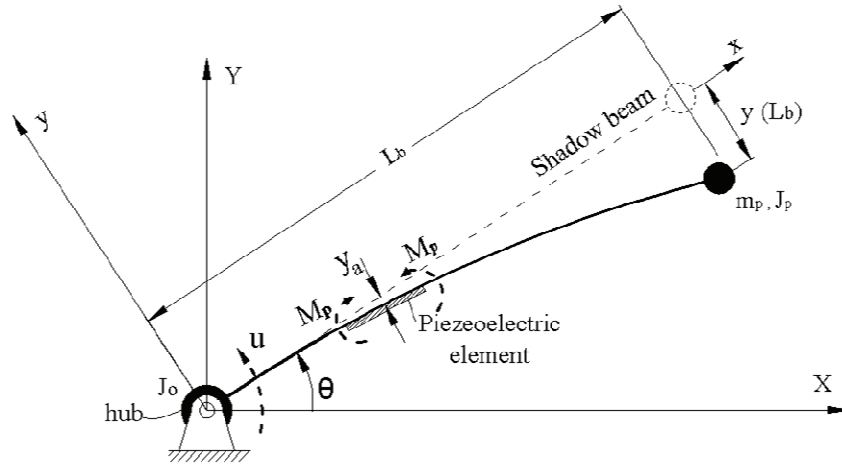
Fig. 9. Schematic of flexible-link manipulator with piezoelectric actuator
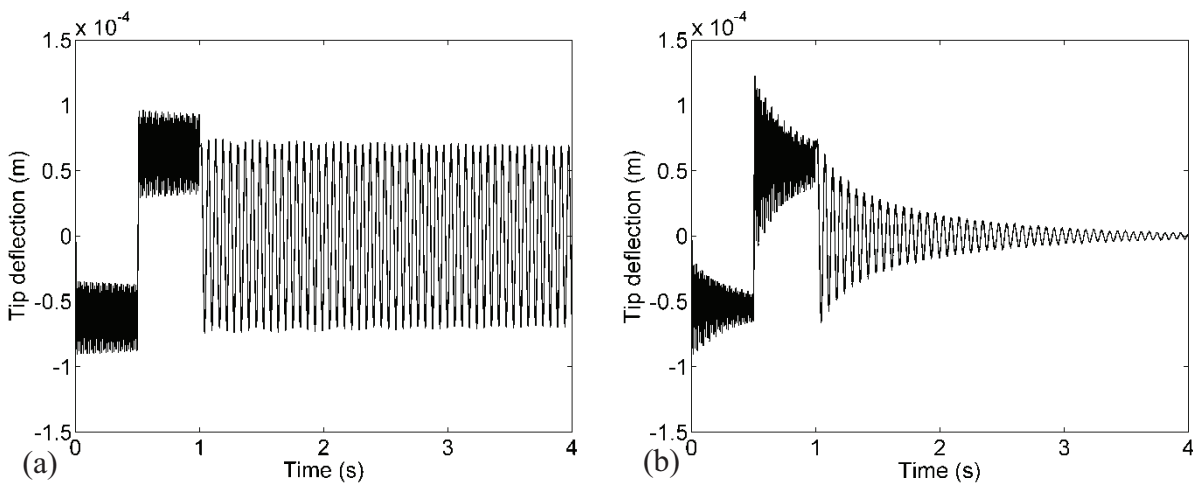
Fig. 10. Deflection of the manipulator when (a) the piezoelectric actuator was inactive, (b) the piezoelectric actuator was activated and located at ─ 0.3.

In another research study carried out by the candidate in [5], the effect of the time delay between the input and output of the controller was investigated. The stability of the controller was analyzed for different gains and time-delays. It was concluded that by increasing the controller's gain greater than a certain value the system became unstable. This value was called the critical gain and was proportional to the time delay of the system; that is, by increasing the time delay, critical gains generally became larger. This was consistent with the simulation results in which a flexible-link manipulator was modeled using a finite element model. The simulation was performed for different time delays and gains and it was shown that the vibration of the manipulator was successfully suppressed provided that the proper time delays and controller's gains were used.

1.3.5 Dynamic modeling of a manipulator with flexible links and flexible joints

Dynamic modeling of the manipulators with flexibility in the joints and links is presented in Chapter 6 and [10]. A schematic of a manipulator consisting of two flexible links interconnected with flexible joints is shown in Fig. 11. In this figure, y_i is the link deflection, where $(0 \leq x_i < l_i)$ and l_i is the length of the ith link, the frame $(\hat{X}_i, \hat{Y}_i)$ is attached to the rigid-like links and $(\hat{x}_i, \hat{y}_i)$ represents the rotating frame. To derive the dynamic equations for the manipulator shown in Fig. 11, two methods were employed. The first method was a combination of the Lagrange method and assumed mode shapes method (LAMM), and the second method was non-linear finite element analysis.
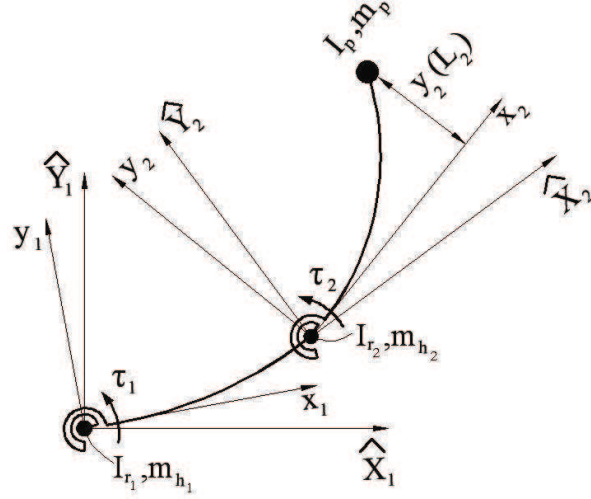
Fig. 11. Schematic of a two flexible-link flexible-joint manipulator (TFLFJ)

In the first approach, the assumed mode shapes method was used to approximate the link deflection as follows

$$y_i(x_i, t) = \sum_{j=1}^{m} \varphi_{ij}(x_i)\, \delta_{ij}(t) \tag{10}$$

where m is the number of mode shapes used for each link, and δ_{ij} is the weight of the assumed mode shape φ_{ij}. To obtain the equations of the motion Lagrange's equations were used. For a system with n degrees of freedom Lagrange's equations were

$$\frac{d}{dt}\frac{\partial}{\partial \dot{q}_i}T - \frac{\partial}{\partial q_i}T + \frac{\partial}{\partial q_i}U = \tau_i, \quad i = 1,2,\cdots,n \tag{11}$$

where T, U and τ_i were respectively the kinetic and potential energies of the system, and the torque applied to the ith motor, and q_i is the ith generalized coordinate. By assuming two mode shapes for each link, two rotations for the motors and two rotations for the links, it was seen that eight degrees of freedom contributed to the dynamics of the TFLFJ. The kinetic energy of a flexible-link flexible-joint manipulator, T, was composed of the kinetic energies of the rotors, T_r, links, T_l, hubs, T_h, and the payload mass, T_p; that is,

$$T = T_r + T_l + T_h + T_p \tag{12}$$

23

The potential energy was the sum of the elastic energies stored in the links and the potential energy due the flexibility of the joints

$$U = \frac{1}{2}\sum_{i=1}^{n}\int_{0}^{l_i}(EI)_i\left[\frac{d^2 y_i(x_i)}{dx_i^2}\right]^2 dx + \frac{1}{2}\sum_{i=1}^{n} k_i(\theta_i - \alpha_i)^2 \tag{13}$$

where $(EI)_i$ and k_i are respectively the rigidity of the ith link and stiffness of the ith joint. Also, angles α_i and θ_i are the motor and link angles measured with respect to the rigid frame $(\hat{X}_i, \hat{Y}_i)$ shown in Fig. 11. By substituting the values of the kinetic and potential energies from equations (14) and (15) into (13), the dynamic equation of system can be obtained. The details of derivation of dynamic equations are given in Chapter 6 and Appendix II. The simulation results of the developed dynamic model are shown in Fig. 12. As shown in this figure, the results obtained by LAMM approach were in an excellent agreement with the FEA results.
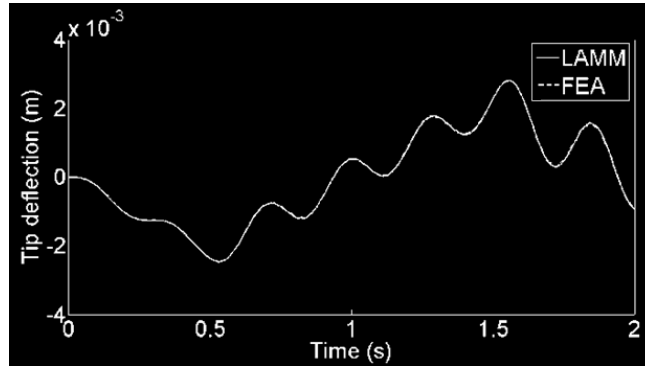
Fig. 12. Tip deflection of the manipulator $(y_2(L_2))$

1.4 References

Candidate's references:

1. H. Salmasi, R. Fotouhi & P. N. Nikiforuk, Tip trajectory tracking of flexible-joint manipulators driven by harmonic drive, *International Journal of Robotics and Automation, 24*(2), 2009.

2. H. Salmasi, R. Fotouhi & P. N. Nikiforuk, A manoeuvre control strategy for flexible joint manipulators with joint dry friction, *Robotica*, *In press*, doi: 10.1017/S0263574709990373, 2009.

3. H. Salmasi, R. Fotouhi & P. N. Nikiforuk, A biologically-inspired controller for tip trajectory tracking of flexible-joint manipulators, *Submitted to International Journal of Robotics and Automation*, 2009.

4. H. Salmasi, R. Fotouhi & P. N. Nikiforuk, On the stability of a friction compensation strategy for flexible-joint manipulators, *Submitted to Advanced Robotics*, 2009.

5. H. Salmasi, R. Fotouhi & P. N. Nikiforuk, Stability analysis of time delay control of flexible link manipulators using piezoelectric actuators, *Submitted to Journal of Advances in Acoustics and Vibration*, 2009.

6. R. Fotouhi, H. Salmasi, S. Dezfulian & R. Burton, Design and control of a hydraulic simulator for a flexible joint robot, *Advanced Robotics*, *21*(6), 2008, 655-679.

7. M. Vakil, R. Fotouhi, P. N. Nikiforuk & H. Salmasi, A constrained Lagrange formulation of multi-link planar flexible manipulator," *Transactions of the ASME, Journal of Vibration and Acoustics,130*(3), 2008, 31007-16.

8. H. Salmasi, R. Fotouhi & P. N. Nikiforuk, Vibration control of a flexible link manipulator using smart structures, *Proceedings of 17th World Congress International Federation of Automatic Control (IFAC)*, Seoul, South Korea, 2008, 11787-11792.

9. H. Salmasi, R. Fotouhi & P. N. Nikiforuk, Active vibration suppression of a flexible link manipulator using piezoelectric actuator, *WIT Transactions on the Built Environment: Computer Aided Optimum Design in Engineering X*, *91*, 2007, 199-208.

10. H. Salmasi, R. Fotouhi & P. N. Nikiforuk, Dynamic modeling of a manipulator with flexible links and flexible joints, *Proceedings of the 21st Canadian Congress of Applied Mechanics*, Toronto, Canada, 2007, (CD Rom).

11. H. Salmasi, R. Fotouhi & P. N. Nikiforuk, Gain analysis of the swarm controller for the tip trajectory tracking of flexible-joint manipulators. To submit to *IEEE/ASME International Conference on Advanced Intelligent Mechatronics*, Montreal, Canada, 2010.

Other references:

12. N. Slack, *The Blackwell Encyclopedic Dictionary of Operations Management* (Blackwell Publishers, Oxford, UK, 1999).

13. B. Siciliano & O. Khatib, *Springer Handbook of Robotics* (Springer, Berlin, Germany, 2008).

14. M. W. Spong, *Control of flexible joint robots: a survey*, Coordinate Science Laboratory, College of Engineering, University of Illinois, UILU-ENG-90-2203, February 1990.

15. H. Diken, Frequency-response characteristics of a single-link flexible joint manipulator and possible trajectory tracking, *Journal of Sound and Vibration*, *233*(2), 2000, 179-194.

16. B. O. Al-Bedoor & A. A. Almusallam, Dynamics of flexible-link and flexible-joint manipulator carrying a payload with rotary inertia, *Mechanism and Machine Theory, 35*(6), 2000, 785-820.

17. S. K. Spurgeon, L. Yao & X. Y. Lu, Robust tracking via sliding mode control for elastic joint manipulators, *Journal of Systems and Control Engineering*, *215*(4), 2001, 405-417.

18. A. Benallegue, Adaptive control for flexible joint robots using a passive systems approach, *Control Engineering Practice, 3*(10), 1995, 1393-1400.

19. K. Khorasani, Adaptive control of flexible joint robots, *Proceedings of IEEE International Conference on Robotics and Automation*, Sacramento, CA, USA, *3*, 1991, 2127-2134.

20. M. C. Han & Y. H. Chen, Robust control design for uncertain flexible-joint manipulators: A singular perturbation approach, *Proceedings of the IEEE Conference on Decision and Control*, San Antonio, TX, USA, *1*, 1993, 611-616.

21. D. Wang, A simple iterative learning controller for manipulators with flexible joints, *Automatica*, *31*(9), 1995, 1341-1344.

22. C. J. B. Macnab & G. M. T. D'Eleuterio, Neuroadaptive control of elastic-joint robots using robust performance enhancement, *Robotica, 19*(6), 2001, 619-629.

23. N. Jalili, An infinite dimensional distributed base controller for regulation of flexible robot arms, *Journal of Dynamic Systems, Measurement and Control, 123*(4), 2001, 712-719.

24. H. D. Taghirad & P. R. Bélanger, H_∞-Based robust torque control of harmonic drive systems, *Journal of Dynamic Systems, Measurement and Control, 123*(3), 2001, 338-345.

25. A. Albu-Schaffer, C. Ott & G. Hirzinger, A unified passivity-based control framework for position, torque and impedance control of flexible joint robots, *International Journal of Robotics Research, 26*(1), 2007, 23-39.

26. M. Spong, K. Khorasani & P. Kokotovic, An integral manifold approach to the feedback control of flexible joint robots, *IEEE Journal of Robotics and Automation, 3*(4), 1987, 291-300.

27. Reference manual of 2-DOF serial flexible joint, Quanser Company, Toronto, revision 1, 2006.

28. D. S. Morgan & I. B. Schwartz, Dynamic coordinated control laws in multiple agent models, *Physics Letters A*, *340,* 2005, 121-131.

29. A. Ratnaweera, S. K. Halgamuge & H. C. Watson, Self-organizing hierarchical particle swarm optimizer with time-varying acceleration coefficients, *IEEE Transactions on Evolutionary Computation*, *8*(3), 2004, 240-255.

30. G. Besançon, Global output feedback tracking control for a class of Lagrangian systems, *Automatica*, *36*(12), 2000, 1915-1921.

31. W. B. Gevarter, Basic relations for control of flexible vehicles. *AIAA Journal 8*(4), 1970, 666-672.

32. A. Preumont, Vibration control of active structures, (Kluwer Academic Publishers, Boston, 1997)

Chapter 2.   Tip Trajectory Tracking of Flexible-Joint Manipulators Driven by Harmonic Drives

TIP TRAJECTORY TRACKING OF FLEXIBLE-JOINT MANIPULATORS DRIVEN BY HARMONIC DRIVES

H. Salmasi, R. Fotouhi and P. N. Nikiforuk

Mechanical Engineering Department, University of Saskatchewan, Saskatoon, Canada

Email: {hamid.salmasi, reza.fotouhi, peter.nikiforuk}@usask.ca

Abstract: In this paper a new control strategy is introduced for tip trajectory tracking of flexible-joint manipulators driven by harmonic drives. The proposed controller incorporates friction compensating torque (FCT) and composite controller torque (CCT), which compensate for the friction in the harmonic drives and the flexibility of the joints, respectively. The FCT is a new controller which includes a non-linear one-state LuGre model and a proportional-derivative (PD) controller. The CCT's design is based on the singular perturbation method and integral manifold concept. An experimental setup of a two-rigid-link flexible-joint (TRLFJ) manipulator was used to verify the proposed controller. The experimental results demonstrated the effectiveness of the controller at slow and fast motions of the manipulator for different trajectories. In particular, the tracking error was reduced significantly by using the proposed controller compared to the results obtained using traditional methods such as the inverse dynamics method for the control of flexible-joint manipulators.

Key Words: Flexible joint manipulator, harmonic drive, joint friction

1. Introduction

Because of their small size and high controllability, electric motors are ideal for use in robot manipulators, but have the disadvantage of having high velocity and low torque. To overcome this drawback, electrically actuated robots use a gear transmission to decrease the operating speed and increase the torque [1]. Among gear transmission systems harmonic drives have such unique features that they have captured designers' attention. They have zero backlash, high torque transmissibility and compact size [2]. On the other hand, it has been determined experimentally [3] that torsional elasticity in harmonic drives results in lightly damped oscillatory vibrations, which limit the application of the harmonic derives especially in robot manipulators performing high precision tasks such as those used in the manufacture of circuit boards. The performance of harmonic drives also deteriorates due to the high friction between the teeth of flexsplines and circular splines. This friction, which is called joint friction, is one of the main limitations in achieving high accuracy manipulation tasks.

Two main concerns in designing controllers for robot manipulators driven by harmonic drives are therefore joint friction and joint flexibility. However, most control strategies developed so far (e.g. [4]) for robot manipulators do not address these concerns and consequently using these control methods may lead to a significant trajectory tracking error which is especially crucial in high-precision tasks. In other works, the dynamic equations of the motion of the links and joints are written as two separate dynamically decoupled equations without considering the reaction of the joint torques on the links [5]. In these models, the equations of rotations of the links and motors are decoupled while the forces related to the rotations of links are assumed as zero. One example of this is ignoring the reaction of the elbow torque on the shoulder link for a two link serial manipulator.

In this paper, a new control strategy for the Tip Trajectory tracking (CSTT) of flexible joint manipulators is presented. While this controller overcomes the shortcomings of the previously developed controllers, it also provides high accuracy in robotic manipulation tasks. In particular, it is experimentally shown that the controller is very precise in the trajectory tracking of manipulators driven by harmonic drives. Two main components of this controller are: A friction compensating torque (FCT) which is designed to compensate for the friction effect, and a composite controller torque (CCT) which is designed to compensate for the flexibility effect in the joints. The FCT is based on the LuGre model which is a dynamic model of nonlinear friction, and to compensate for the flexibility in the joints, the CCT is designed based on the singular perturbation theory and the integral manifold concept.

The outline of this paper is as follows. An overall picture of the experimental setup and the developed control strategy are given in Section 2. The procedures used to obtain controller components, the FCT and the CCT, are described in Sections 3 and 4. Section 5 includes the experimental results obtained using different control strategies for different trajectories, and Section 6 contains the conclusions.

2. Description of the Experimental Setup

Fig. 1 shows the schematic of the control strategy that was used in the control of the two-rigid-link flexible-joint manipulator (TRLFJ). The desired trajectory q_d and its derivatives, $\dot{q}_d$ and $\ddot{q}_d$ were the inputs to the controller and the rotation and velocity of the motor and link were used as feedback to the controller. The positions of the motor and link, q_L and q_m, were measured using the encoders implemented in the experimental setup and the velocities were then obtained by taking the derivatives of the position signals using a first-order low-pass filter which

attenuated high-frequencies noise in the velocity signal. This filter was used which cancelled out high-frequency noises due to differentiation of the position signal. The applied torque τ had two parts; the friction torque τ_f and the composite torque τ_c, i.e. $\tau = \tau_f + \tau_c$. The procedures of obtaining these torques are described in the following sections. To calculate the current required by the motor, the resultant torque τ was multiplied by the inverse of the torque constant of the motor, K_t, and the current was then fed into the D/A card. To obtain the velocity signal, The motor torque constants for the experimental setup were $K_{t,shoulder} = 8.92\,N.m\,/\,A$ and $K_{t,elbow} = 1.31\,N.m\,/\,A$ [1].

The experimental setup which was used for experimentation is shown in fig. 2. As shown in this figure, the first link (shoulder link) was coupled to the first joint (shoulder joint) by means of a flexible joint. At the end of the shoulder link was a second harmonic drive which was connected to the elbow link via the flexible elbow joint as shown in fig. 2(b). In this figure, angles q_{m_s} and q_{m_e} were rotations of the shoulder and elbow motors, and angles q_{l_s} and q_{l_e} were rotations of the shoulder and elbow links, respectively. Both motors and both flexible joints were instrumented with quadrature optical encoders whose resolutions were 0.0015 *rad/count* [6]. Other physical parameters of the manipulator are given in Table 1.

3. Design of FCT

The design procedure of the friction compensating torque (FCT) is explained in this section. The friction properties of the harmonic drives were modeled and experimentally

---

[1] It is noteworthy that the DC permanent magnet motors usually have a linear relationship to motor torque.

identified in Sections 3.1 and 3.2, and the method used to obtain the FCT is explained in Section 3.3.

3.1. Friction Modeling

A well-known friction model which describes different aspects of the friction torque is the LuGre model [7]. In this model, on the microscopic scale, surfaces sliding on each other are modeled as two rigid bodies that make contact through their elastic bristles which model the random asperities of the surfaces (see fig. 3). The proposed model has the mathematical form:

$$\frac{dy}{dt} = \dot{q}_m - \sigma_0 \frac{|\dot{q}_m|}{g(\dot{q}_m)} y, \tag{1}$$

$$\tau_f = \sigma_0 y + \sigma_1 \frac{dy}{dt} + c_m \dot{q}_m, \tag{2}$$

where y is the average deflection of the bristles (see fig. 3), $\dot{q}_m$ the relative velocity between surfaces, σ_0 the stiffness of the bristles, σ_1 the damping of the bristles, and c_m the viscous damping coefficient. Also, τ_f is the friction torque between the sliding surfaces. The function $g(\dot{q}_m)$ represents the Stribeck effect. Since the average deflection of the bristles can not be measured directly, finding the exact solution to predict the friction behavior is not possible. However, (1) and (2) can be simplified for the steady-state condition (sliding regime) in which the deformation rate of the bristles is zero ($dy/dt = 0$). Thus, from (1) for steady-state conditions:

$$\sigma_0 y_{ss} = g(\dot{q}_m) \frac{\dot{q}_m}{|\dot{q}_m|} = g(\dot{q}_m) \operatorname{sgn}(\dot{q}_m) \tag{3}$$

where y_{ss} is the steady-state value of the bristles deformation and $\operatorname{sgn}(\dot{q}_m) = 1$ for $\dot{q}_m > 0$ and $\operatorname{sgn}(\dot{q}_m) = -1$ for $\dot{q}_m < 0$. Substituting (3) in (2) results in:

$$\tau_f = \mathrm{sgn}(\dot{q}_m)g(\dot{q}_m) + c_m\dot{q}_m \tag{4}$$

A typical proposed form for the function $g(\dot{q})$ which describes the Stribeck effect is

$g(\dot{q}_m) = \tau_{f,c} + (\tau_{f,s} - \tau_{f,c})e^{-(\dot{q}_m/v_s)^2}$ where $\tau_{f,c}$ and $\tau_{f,s}$ are the Coulomb friction and stiction

torques respectively, and v_s is the Stribeck velocity. By replacing this function in (4), the friction

torque based on the LuGre model is obtained as:

$$\tau_f = [\tau_{f,c} + (\tau_{f,s} - \tau_{f,c})e^{-(\dot{q}_m/v_s)^2}]\mathrm{sgn}(\dot{q}_m) + c_m\dot{q}_m \tag{5}$$

The first two terms of the friction torque in (5) represent the Coulomb friction and Stribeck

effect, respectively, and the last term accounts for the viscous damping. To determine the friction

torque as a function of the velocity in (5) four parameters $\psi = [\tau_{f,s}, \tau_{f,c}, v_s, c_m]$ must be

identified. The experimental procedure which was designed and used to identify these

parameters is described in the following section.

3.2. Parameter Identification of Friction Model

The schematic of the experiment procedure which was used to identify the friction torque in

joints is shown in fig. 4. The dynamic equations of the motors are expressed as:

$$J\ddot{q}_m = \tau - \bar{\tau}_f \tag{6}$$

where J is the matrix of mass moment of inertias of the motors. Torques τ and $\bar{\tau}_f$ are the

vectors of the applied torque and the joint friction torque, respectively, and $\ddot{q}_m$ is the vector of

accelerations of the motors. The motor position was controlled by a proportional-integrator-

derivative (PID) controller to follow a triangle wave position reference. Since the reference

trajectory is a constant-velocity trajectory, if the motor follows the reference trajectory, the

motor acceleration, $\ddot{q}_m$, will become zero and as a result the applied torque will be equal to the

friction torque in the above equation, i.e. $\tau = \bar{\tau}_f$. Therefore, the friction torque was determined

by measuring the applied torque. In total, 57 experiments were carried out at different velocities to estimate the friction function for the shoulder and elbow joints. The experimental data of the shoulder and elbow joint motors are shown in fig. 5. These data were then interpolated (curve-fitted) using the function $\tau_f(\dot{q}_m)$ given in (5), and the friction torques were obtained as functions of the velocity for the shoulder joint motor:

$$
\begin{aligned}
\tau_f &= 1.5729 - 0.7919\, e^{-(\dot{q}_m/0.1900)^2} + 3.2587\, \dot{q}_m, \quad \dot{q}_m > 0 \\
\tau_f &= -1.9882 + 0.8465\, e^{-(\dot{q}_m/0.1991)^2} + 2.9333\, \dot{q}_m, \quad \dot{q}_m < 0
\end{aligned}
\tag{7}
$$

and for the elbow joint motor:

$$
\begin{aligned}
\tau_f &= 0.6761 - 0.2992\, e^{-(\dot{q}_m/0.6050)^2} + 0.2532\, \dot{q}_m, \quad \dot{q}_m > 0 \\
\tau_f &= -0.6826 + 0.2802\, e^{-(\dot{q}_m/0.4824)^2} + 0.3007\, \dot{q}_m, \quad \dot{q}_m < 0
\end{aligned}
\tag{8}
$$

According to the functions of the friction torques given in (7) and (8), the Stribeck effect in the elbow joint motor is greater than in the shoulder joint motor. However, the shoulder joint has larger viscous damping and stiction than the elbow joint.

3.3. Friction Compensation in Harmonic Drives

There are different ways to compensate for the friction in robot manipulators. A simple well known method is that of adding a high frequency dither signal to the control signal, but this method cannot be used in applications with high precision [8]. Another non-model-based friction compensating method is using a stiff PD controller which is suitable for regular tasks, however, it results in steady-state errors and might lead to the stick-slip oscillations at low velocities [9].

The method which was used in this investigation was a model-based friction compensation strategy. In this method, friction was compensated by applying an equivalent torque in the opposite direction of the friction torque. The equivalent torque was found based on (7) and (8). Ideally, the counterbalancing estimated friction torque, τ_f, was equal to the real friction of the

system, $\overline{\tau}_f$, and, hence, the friction of the system would be compensated completely. However, practically there was always an error between the estimated friction torque and the actual friction torque, because the friction torque defined in (7) and (8) was obtained based on the assumption of steady-state conditions. Also, the effects of the oil temperature, load, humidity and actuator wear were not considered in modeling joints friction [10]. To overcome these deficiencies of the friction torques obtained in (7) and (8), a linear PD controller was added to the LuGre model. Using a PD controller along with the friction compensating torque given in (7) and (8) guarantees that the error in friction compensation is bounded and the system remains stable provided that the gains are chosen properly. In this research, the gains of PD controller for shoulder joint were chosen as $K_p = 500$ and $K_v = 40$. These values for elbow joint were $K_p = 15$ and $K_v = 8$.

4. Design of Composite Controller Torque

The second part of the controller was a composite controller which was designed to compensate for the effect of the flexibility of the joints. The singular perturbation theory and integral manifold concept were used in the design procedure of the composite controller torque (CCT). Using singular perturbation theory allows dividing the dynamics of flexible-joint manipulator into two subsystems: one corresponding to the fast dynamics (high frequency vibration due to the flexibility) and the other to the slow dynamics (low-frequency motion). The standard governing equations of a singularly perturbed system are [11]:

$$\dot{X} = f(X, Z, \varepsilon, t), \quad X(t_0) = X^0, \quad X \in R^n \tag{9}$$

$$\varepsilon \dot{Z} = g(X, Z, \varepsilon, t), \quad Z(t_0) = Z^0, \quad Z \in R^m \tag{10}$$

where ε represents a small parameter, X and Z are state vectors of dimensions n and m, respectively, $f \in R^n$, $g \in R^m$, and $\dot{X}$ and $\dot{Z}$ represent the derivatives of X and Z with respect to time, respectively. The above equations represent a two-time-scale system in which the state Z is the fast parameter of the system because ε is a small parameter and $\dot{Z}$ is very large in (10). The state X is the slow state of the system because it has a slower time derivative than state Z.

Another useful concept which can be used in the context of the singular perturbation theory is the integral manifold. By means of the integral manifold, it is possible to reduce the order of the singular system presented in (9) and (10) from $(n+m)$ to n. The implementation of integral manifold concept for singularly perturbed systems includes the following steps:

Step 1 (Integral manifold implementation): The fast states, Z, are approximated as a set of functions of the slow states and the singular perturbation parameter, i.e. $Z \approx \overline{Z} = \varphi(X, \varepsilon)$ where φ is an approximation function for the fast states.

Step 2 (Composite controller design): The composite controller, τ_c, includes the slow and fast controllers. The slow controller, $\tau_{c,s}$, is designed to control the reduced-order model and the fast controller, $\tau_{c,f}$, guarantees that the approximation error made in step 1 between the fast states and the integral manifold, $Z - \varphi$ exponentially goes to zero and the fast states are on the integral manifold (see fig. 6(a)). As long as Z is on the integral manifold φ, the slow state X approaches the reduced-order model (see fig. 6(b)). Thus, provided that the fast state Z is restricted to move along the integral

manifold, the slow controller can only be designed for the reduced-order model to control the slow state X.

In the following the application of the singular perturbation theory and the integral manifold concept is used to design a composite controller for flexible joint manipulators.

4.1. Singularly Perturbed Equations of Flexible-Joint Manipulators

The dynamic equations of a serial manipulator consisting of n-rigid links connected by $(n-1)$ elastic joints are described by the following set of differential equations:

$$D(q_L)\ddot{q}_L + C_l(q_L,\dot{q}_L)\dot{q}_L + K(q_L - q_m) = H(\tau - \bar{\tau}_f) \tag{11}$$

$$J\ddot{q}_m - K(q_L - q_m) = \tau - \bar{\tau}_f \tag{12}$$

where $D(q_L) \in R^{n \times n}$ is the inertia matrix of the links and $C_l(q_L,\dot{q}_L)\dot{q}_L$ represents the Coriolis and centrifugal vectors. The diagonal matrix $K = diag(k_1,k_2,\cdots,k_n)$ represents the stiffness of the joints. $J \in R^{n \times n}$ is the inertia matrix of the motors, τ is the vector of the applied torques to the motors, and $\bar{\tau}_f$ is the friction joint torques. Also, $q_L \in R^n$ and $q_m \in R^n$ represent, respectively, the rotations of the links and the motors. The components of the matrix H are defined as $H_{ij} = -1$ when $i = j-1$, and $H_{ij} = 0$ when $i \neq j-1$ $i,j = 1,2,\cdots,n$. As defined in Section 2, the applied torque τ is the summation of the friction compensating torque $,\tau_f$, and the composite controller torque τ_c; i.e. $\tau = \tau_f + \tau_c$. Assuming that the friction compensating torque τ_f counterbalances the real friction of the joints $\bar{\tau}_f$ completely; that is, $\bar{\tau}_f = \tau_f$, the joints friction can be eliminated from the dynamic equations of the manipulator. Thus:

$$D(q_L)\ddot{q}_L + C_l(q_L,\dot{q}_L)\dot{q}_L + K(q_L - q_m) = H\tau_c \tag{13}$$

$$J\ddot{q}_m - K(q_L - q_m) = \tau_c \tag{14}$$

To define the singular perturbation parameter, all the joint stiffness k_i, $i = 1, 2, \cdots, n$ are assumed to have the same order of magnitude and they can be written as a multiple of a single large parameter $\bar{k}$; that is $k_i = \bar{k}\,\tilde{k}_i$, $i = 1, \cdots, n$. The elastic joint torques are then written as:

$$\xi = K(q_L - q_m) = \bar{k}\tilde{K}(q_L - q_m) \tag{15}$$

where $\tilde{K} = diag(\tilde{k}_1, \cdots, \tilde{k}_n)$. Without loss of generality (by rescaling the ξ variables if necessary), the matrix $\tilde{K}$ is chosen as $\tilde{K} = I$. The singular perturbation parameter can now be defined as $\mu = 1/\bar{k}$, and (15) becomes $\mu\xi = q_L - q_m$. After some mathematical manipulation, the state-space representation of the singularly perturbed system (13) and (14), is obtained as:

$$\dot{X} = A_1 + A_2 Z + A_3 \tau_c \tag{16}$$

$$\varepsilon\dot{Z} = B_1 X + B_2 Z + B_3 \tau_c \tag{17}$$

where $X = [q_L \quad \dot{q}_L]^T$, $Z = [\xi \quad \varepsilon\dot{\xi}]^T$, $\varepsilon = \sqrt{\mu}$, $A_1 = \begin{bmatrix} \dot{q}_L \\ -D^{-1}C_l\dot{q}_L \end{bmatrix}$, $A_2 = \begin{bmatrix} O_{n\times n} & O_{n\times n} \\ -D^{-1} & O_{n\times n} \end{bmatrix}$,

$A_3 = \begin{bmatrix} O_{n\times n} \\ D^{-1}H \end{bmatrix}$, $B_1 = \begin{bmatrix} O_{n\times n} & O_{n\times n} \\ O_{n\times n} & -D^{-1}C_l \end{bmatrix}$, $B_2 = \begin{bmatrix} O_{n\times n} & I_{n\times n} \\ -(J^{-1}+D^{-1}) & O_{n\times n} \end{bmatrix}$, $B_3 = \begin{bmatrix} O_{n\times n} \\ D^{-1}H - J^{-1} \end{bmatrix}$ and O is

a null matrix and I is the identity matrix. In the following section, the integral manifold concept is employed to obtain the composite controller τ_c. The purpose of composite controller τ_c is to track the link rotation q_L on the desired trajectory q_d.

4.2. Implementing Integral Manifold for FJMs

An integral manifold for a flexible joint manipulator in the space R^{2n} is:

$$M_\varepsilon : \bar{Z} = \varphi(X, \tau_{c,s}, \varepsilon, t); \quad X \in R^{2n} \tag{18}$$

If the fast states Z move on the integral manifold (see fig. 6(a)), then Z can be substituted by the integral manifold φ in (17), and therefore:

$$\varepsilon\,\dot\varphi = B_1 X + B_2\varphi + B_3\tau_{c,s} \tag{19}$$

Also, the reduced-order model of the system is obtained by substituting the integral manifold in (16):

$$\dot X = A_1 + A_2\varphi + A_3\tau_{c,s} \tag{20}$$

The procedures used to construct the slow and fast controllers are explained in the following section.

4.3. Construction of the Composite Controller Torque for Flexible-Joint Manipulators

The design of the composite controller torque (CCT) was based on the singularly-perturbed dynamic equations of the flexible-joint manipulators and had two parts: the slow controller, $\tau_{c,s}$, and the fast controller $\tau_{c,f}$. The slow controller was designed to control the slow subsystem representing the low-frequency motion of the manipulator. Thus, when the joint flexibility approached infinity, the slow subsystem reduced to a rigid manipulator. The fast controller, $\tau_{c,f}$, was selected to suppress the high-frequency vibration of the manipulator. Thus the composite controller τ_c can be written as the summation of slow and fast controller torques as:

$$\tau_c = \tau_{c,s} + \tau_{c,f} \tag{21}$$

The parameter η is the difference between Z and the integral manifold φ, therefore:

$$\eta = Z - \varphi \tag{22}$$

Taking the derivative of (22) and combining with (17), (19) and (21) results in:

$$\varepsilon\dot\eta = \varepsilon\dot Z - \varepsilon\dot\varphi = B_2\eta + B_3\tau_{c,f} \tag{23}$$

From (16), (22) and (23) the equations of the slow and fast subsystems in state space are:

$$\dot{X} = A_1 + A_2\varphi + A_2\eta + A_3\tau_c \tag{24}$$

$$\varepsilon\dot{\eta} = B_2\eta + B_3\tau_{c,f} \tag{25}$$

Equation (24) describes the low-frequency motion and (25) describes the high-frequency motion of the robot manipulator. It is worth noting that once the fast state, Z, meets and stays on the integral manifold φ (that is $Z = \varphi$), parameter η and its derivative $\dot{\eta}$ will be zero according to (22) and (25). This results in $\tau_{c,f}$ becoming zero in (25) since $B_3 \neq 0$, and the composite controller torque having only the slow part, i.e. $\tau_c = \tau_{c,s}$. The slow controller for flexible-joint manipulator can be obtained as:

$$\tau_{c,s} = \tau_{c,0} + \varepsilon^2(D^{-1}H - J^{-1})^{-1}\ddot{\varphi}_{0,1} \tag{26}$$

where $\tau_{c,0}$ is the *rigid controller* and it can be designed based on the conventional methods available for the rigid manipulators such as the inverse-dynamics approach [12]. Also $\ddot{\varphi}_{0,1}$ is the second time derivative of $\varphi_{0,1}$. The vector $\varphi_{0,1}$ includes the first n components of the vector $\varphi_0 \in R^{2n}$ where:

$$\varphi_0 = -B_2^{-1}(B_1X + B_3\tau_{c,0}) \tag{27}$$

The fast controller must be designed so that the deviation between the integral manifold and parameter Z asymptotically approaches zero. If the fast controller is chosen to have the state-feedback format as $\tau_{c,f} = B_4\eta$ where B_4 is a constant matrix and the parameter η is the difference between Z and the integral manifold φ, (25) becomes:

$$\varepsilon\dot{\eta} = (B_2 + B_3)B_4\eta \tag{28}$$

If the elements of matrix B_4 are chosen such that the eigenvalues of the square matrix $(B_2 + B_3B_4)$ always have negative real parts, the deviation of Z from its manifold will asymptotically goes to zero and, finally, Z will be on its invariant manifold.

5. Experimental Verification

The two-rigid-link flexible-joint (TRLFJ) manipulator shown in fig. 2 was used to verify experimentally the performance of the new controller described in the previous sections. The physical parameters are given in Table 1.The desired link trajectory was chosen as:

$$q_d = [90(t/t_f)^9 - 315(t/t_f)^8 + 540(t/t_f)^7 - 420(t/t_f)^6 + 126(t/t_f)^5]q_f \qquad (29)$$

where q_d, q_f and t_f were, respectively, the desired trajectory of the rotations of the links, the final rotation of the link and the time of total manoeuvre. The proposed trajectory was designed such that it satisfied the initial conditions of $q_d(0) = 0$ and $q_d(t_f) = q_f$, and its first four derivatives were zero at $t = 0$ and $t = t_f$.

5.1. Trajectory Tracking Results

Since the friction is very sensitive to the velocity, four different sets of trajectories were experimentally examined to determine the performance of the controller at different velocities and accelerations. The final positions of the shoulder and elbow links were:

$$[q_{f,shoulder}, q_{f,elbow}]_1 = [1.0 \, rad, 1.0 \, rad], [q_{f,shoulder}, q_{f,elbow}]_2 = [1.5 \, rad, 1.0 \, rad]$$
$$[q_{f,shoulder}, q_{f,elbow}]_3 = [1.0 \, rad, 1.5 \, rad], [q_{f,shoulder}, q_{f,elbow}]_4 = [1.5 \, rad, 1.5 \, rad] \qquad (30)$$

The manoeuvre time was the same for all sets of trajectories, i.e. $t_f = 2 \sec.$, hence, increasing the final positions resulted in more rapid motion of the manipulator. Therefore, choosing different final positions enabled the performance of the controller to be determined at both slow and fast manoeuvres of the manipulator. The rotations of the shoulder and elbow links are shown and compared with the desired trajectories in Figs. 7 to 10. As shown in these figures, the links followed the desired trajectories accurately. The tracking error values are shown in Section 5.2. Also, it was experimentally found if the friction was not considered in the design

procedure of the controller, the manipulator was not able to start its motion because of high stiction in the harmonic drives.

5.2. Comparing New Control Strategy with the Rigid Controller

To analyze the effectiveness of the proposed new control strategy for Tip Trajectory tracking (CSTT), the trajectory tracking results were compared with the results obtained when the rigid controller, $\tau_{c,0}$, was combined with the friction compensating torque τ_f. The rigid controller was obtained using the inverse-dynamic approach and based on the assumption of rigid joints (i.e. $K \rightarrow \infty$) (see appendix II for details). To have a reasonable measure for comparing the results, the tracking error percentages were normalized as:

$$error = [(q_L - q_d)/q_f] \times 100 \tag{31}$$

This error indicates the difference between experimental and the desired values of the link rotation. Also, the maximum of the normalized error during the manoeuvre is defined as:

$$error_{max} = \max \left| (q_L - q_d)/q_f \right| \tag{32}$$

The results for the four sets of trajectories given in the previous section, equation (29), are shown in Figs. 11 to 14. It can be observed that the tracking error was significantly reduced by using the CSTT compared with the results obtained using the rigid controller. For instance, according to the values of the maximum errors in Table 2, the performance of the controller improved 26% for the shoulder and 23% for the elbow by using the CSTT when the final rotations of the links were $[q_{f,shoulder}, q_{f,elbow}]_1 = [1\,rad, 1\,rad]$. Also, it is shown in Figs. 12(b) and 14(b) that by increasing the final rotation of the shoulder link from 1.0 *rad* to 1.5 *rad*, the rotations of the links, especially the elbow link, became unstable using the rigid controller. Also, the responses of the links were unstable when the final rotation of the elbow link was increased

to 1.5 *rad* in fig. 13(b). That means that the rigid controller was unable to control the rotations of the links for high-speed manoeuvres. In contrast to the results of the rigid controller, the results obtained using CSTT showed that the tracking error remained in an acceptable range of $\pm 2\%$ for high-speed and slow manoeuvres of the flexible-joint manipulator. Also, it can be observed in Figs. 13(a) to 16(a), that the elbow and shoulder links oscillated with frequencies close to their natural frequencies when they reached the final rotation, q_f. The shoulder link oscillated with a frequency of $1.08\,Hz$ the elbow link oscillated with a frequency of $3.21\,Hz$.

Furthermore, it can be seen in Figs. 13(a) and 14(a) that the response of the elbow link in the first part of the manoeuvre ($0 < t \leq 1$) was very different than that of the second part ($1 < t \leq 2$) when the CSTT was used. This property can be explained based by the fact that the friction was different during acceleration (increasing velocities) than deceleration (decreasing velocities), due to frictional lag or hysteresis [7]. In the first part of the response, whereas the velocity was increased (acceleration), the friction was compensated effectively. However, in the second part, where the velocity was decreased (deceleration), one may conclude that the estimation of friction was not very accurate. A summary of the maximum values of errors are tabulated in Table (2) for the rigid and the CSTT controllers for different trajectories.

6. Conclusions

A new control strategy was developed for the tip trajectory tracking of flexible joint manipulators which are driven by harmonic drives. The proposed controller included two parts, the friction compensating torque (FCT) to compensate for the friction effect and the composite controller (CCT) to compensate for the flexibility of the joints. The FCT was a combination of the LuGre dynamic model and a PD controller. The parameters of the dynamic model were

determined through constant-velocity closed-loop experiments, and the gain values of the PD were chosen such that the controller was stable.

The integral manifold in the context of the singular perturbation theory was used to design a new composite controller, the CCT, which included two parts, slow and fast controllers. The performance of the proposed controller was experimentally confirmed at different manipulation speeds for several trajectories. Also, comparing experimental results using the developed controller with the results of a rigid controller demonstrated the superiority of the composite controller over the rigid controller which is usually used. For instance, the maximum error was reduced significantly using the CSTT compared to the results of the rigid controller. Furthermore, when the final rotations of the links were increased from $1.0\, rad$ to $1.5\, rad$, the results of the rigid controller became unstable while the tracking error of the CSTT remained in an acceptable range.

7. References

[1]   H.D. Taghirad, & P.R. Bélanger, H_∞-Based robust torque control of harmonic drive systems, *Journal of Dynamic Systems, Measurement and Control, 123*(3), 2001, 338-345.

[2]   A. Albu-Schaffer, C. Ott, & G. Hirzinger, A unified passivity-based control framework for position, torque and impedance control of flexible joint robots, *International Journal of Robotics Research, 26*(1), 2007, 23-39.

[3]   L. Sweet, & M. Good, Redefinition of the robot motion-control problem, *IEEE Control Systems Magazine, 5*(3), 1985, 18-25.

[4]   J.G. Yim, J.S. Yeon, J.H. Park, S.H. Lee, & J.S. Hur, Robust control using recursive design method for flexible joint robot manipulator, *IEEE International Conference on Robotics and Automation,* Roma, Italy, 2007, 3805-3810.

[5]   F. Ghorbel, & M.W. Spong, Integral manifolds of singularly perturbed systems with application to rigid-link flexible-joint multibody systems, *International Journal of Non-linear Mechanics, 35*(1), 2000, 133-155.

[6]   Reference manual of 2-DOF serial flexible joint, Quanser Company, Toronto, revision 1, 2006.

[7]   C. Canudas de Wit, H. Olsson, K.J. Astrom, & P. Lischinsky, A new model for control of systems with friction, *IEEE Transactions on Automatic Control, 40*(3), 1995, 419-425.

[8]   M.A. Michaux, A.A. Ferri, & K.A. Cunefare, Effect of tangential dither signal on friction induced oscillations in an SDOF Model, *Journal of Computational and Nonlinear Dynamics 2*(3), 2007, 201-210.

[9]   R.H.A. Hensen, *Controlled mechanical systems with friction*, Ph.D. Thesis, Eindhoven University of Technology, Eindhoven, The Netherlands, 2002.

[10]   P. Lischinsky, C. Canudas-de-Wit, & G. Morel, Friction compensation of a Schilling hydraulic robot, *Proceedings of IEEE International Conference on Control Applications*, Hartford, CT, USA, 1997, 294-299.

[11]   P.V. Kokotovic, H.K. Khalil, & J. O'Reiley, *Singular perturbation methods in control: analysis and design*, (New York: Academic Press, 1986).

[12]   Y. Feng, S. Bao, & X. Yu, Inverse dynamics nonsingular terminal sliding mode control of two-link flexible manipulators, *International Journal of Robotics and Automation*, *19*(2), 2004, 91-102.
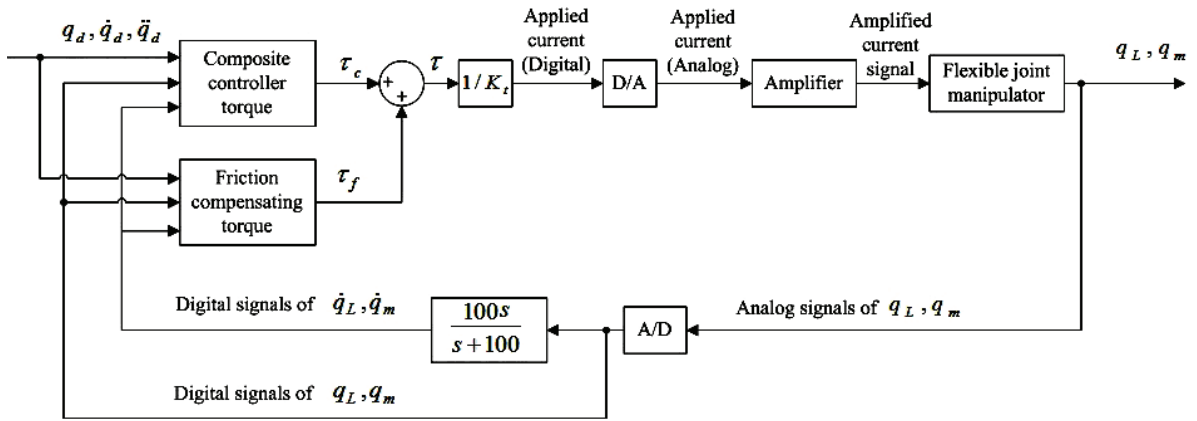
Figure 1. Control strategy designed for tip trajectory tracking of two-rigid-link flexible-joint manipulator (TRLFJ)

(a)

(b)
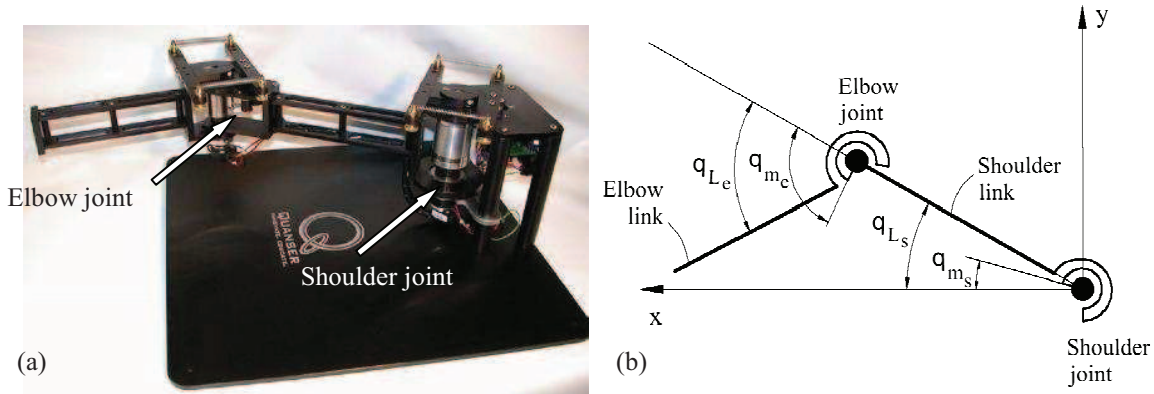
Figure 2. (a) Experimental module of two-rigid-link flexible-joint manipulator available in the Robotics Laboratory of the University of Saskatchewan, (b) the schematic of the top-view of the experimental setup showing the angles of the joints and the links

Table 2

Physical parameters of the experimental setup of TRLFJ

Parameter	Symbol	Shoulder	Elbow
Equivalent inertia of the downstream mechanism of the link^2 $(kg.m^2)$	D	0.2300	0.0107
Mass moment of inertia of the motor $(kg.m^2)$	J	0.0110	0.0094
Joint stiffness $(N.\frac{m}{rad})$	K	10.30	3.930
Length of the link (m)	l	0.2230	0.2230
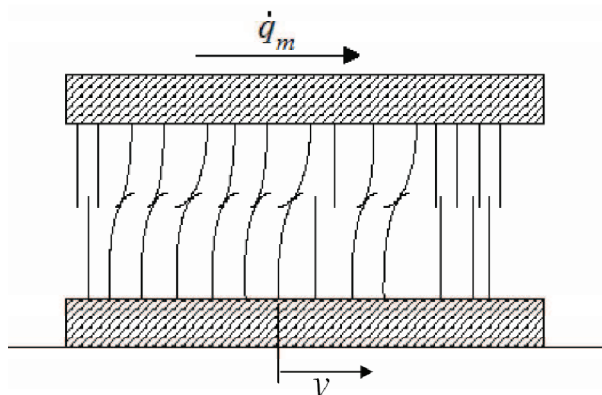
Figure 3. Two surfaces sliding on each other with relative velocity of $\dot{q}_m$; the asperities are modeled as elastic bristles attached to the rigid bodies

---

^{2} The equivalent inertia for the shoulder includes the mass moment of inertias of the shoulder and elbow links, and the elbow motor with respect to the shoulder joint. Also, the equivalent inertia for the elbow includes the mass moment of inertia of the elbow link with respect to the elbow joint.
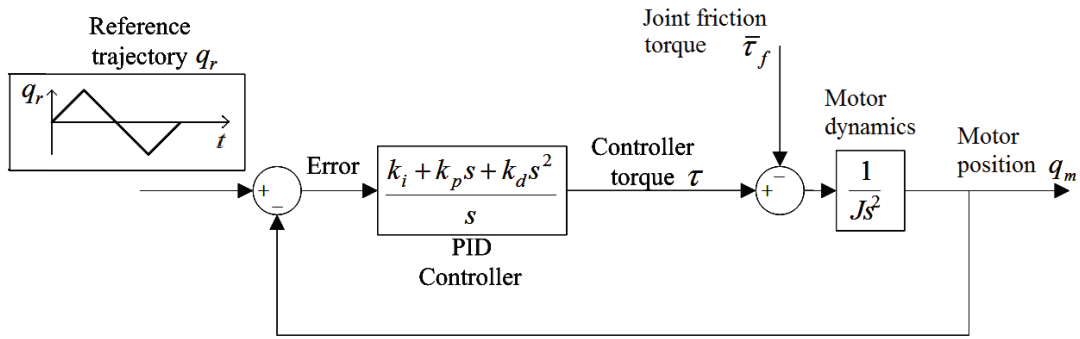
Figure 4. Schematic of the control procedure used to identify the LuGre model parameters for experimental setup shown in fig. 2
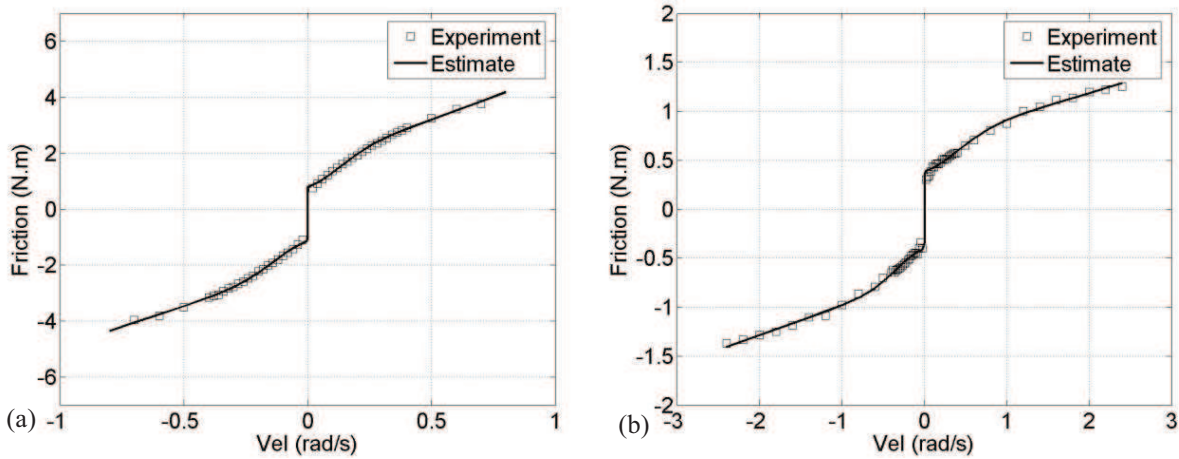
Figure 5. Experimental results obtained for steady state conditions and estimation function obtained based on the LuGre model for (a) shoulder joint motor, (b) elbow joint motor
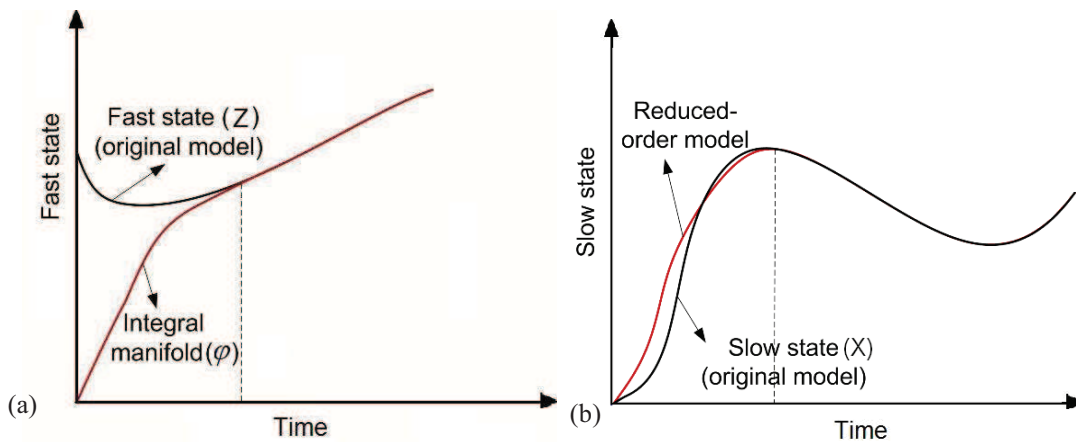
Figure 6. (a) Fast state Z approaches the integral manifold φ due to the fast controller, and (b) slow state X is equal to the reduced-order model, as long as the fast state is on the integral manifold
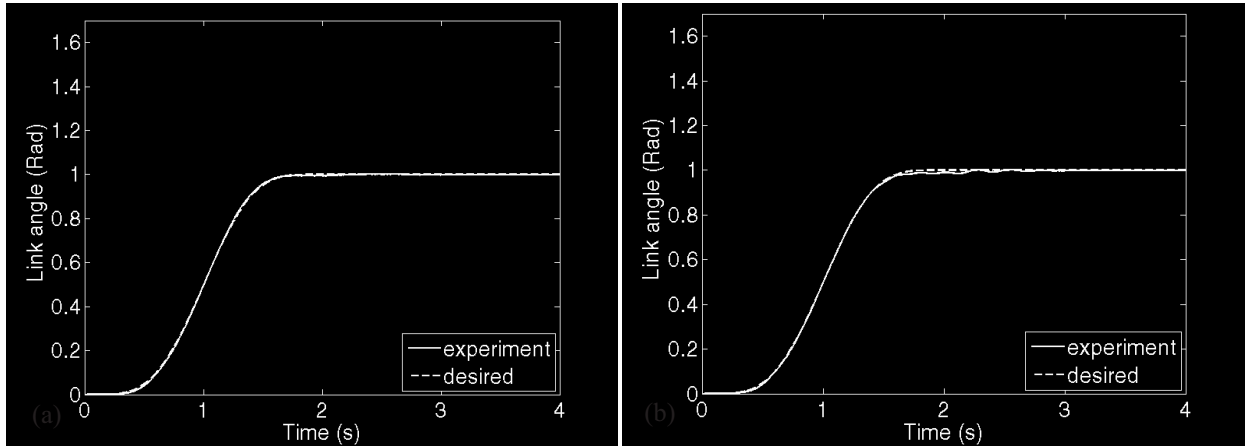
Figure 7. Experimental verification of the links' rotations for $[q_{f,shoulder}, q_{f,elbow}]_1 = [1.0\,rad, 1.0\,rad]$ **using CSTT controller, (a) shoulder link trajectory (b) elbow link trajectory**
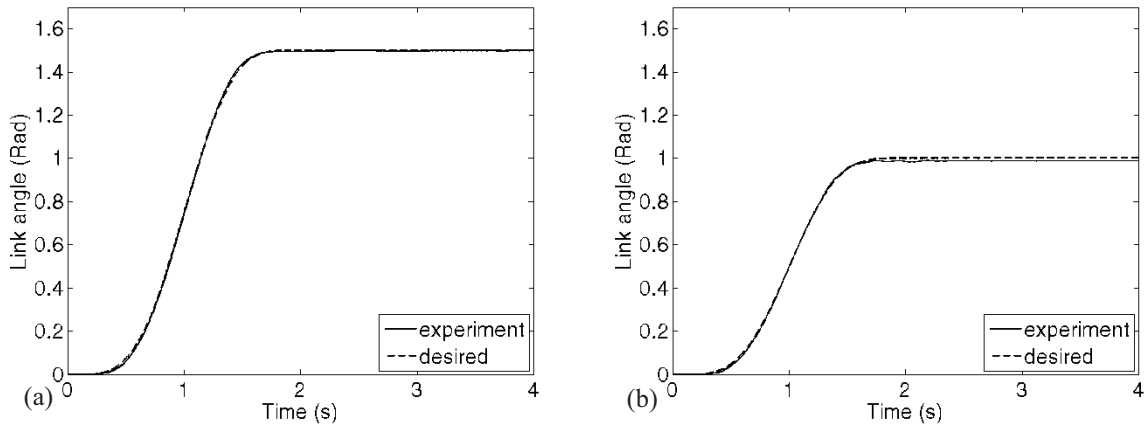
Figure 8. Experimental verification of the links' rotations for $[q_{f,shoulder}, q_{f,elbow}]_2 = [1.5\,rad, 1.0\,rad]$ **using CSTT controller, (a) shoulder link trajectory (b) elbow link trajectory**
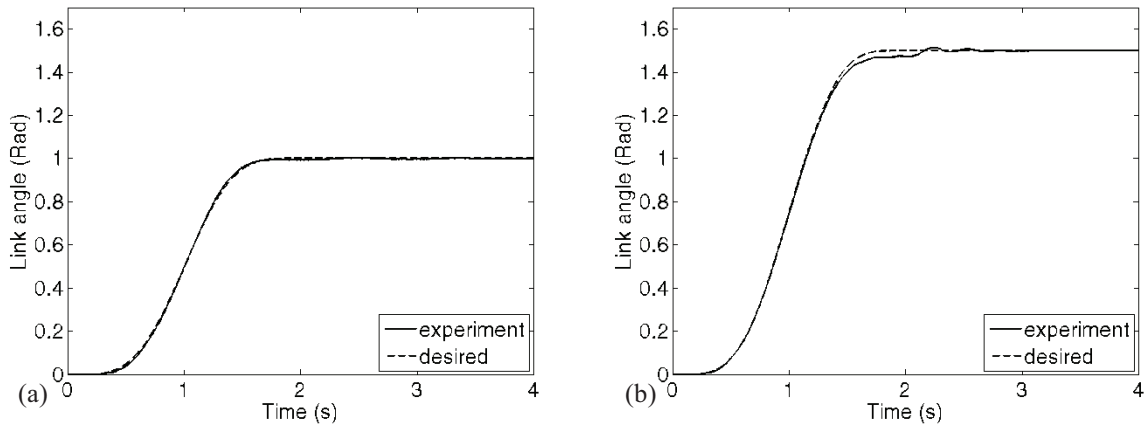
Figure 9. Experimental verification of the links' rotations for $[q_{f,shoulder}, q_{f,elbow}]_3 = [1.0\,rad, 1.5\,rad]$ **using CSTT controller, (a) shoulder link trajectory (b) elbow link trajectory**

50
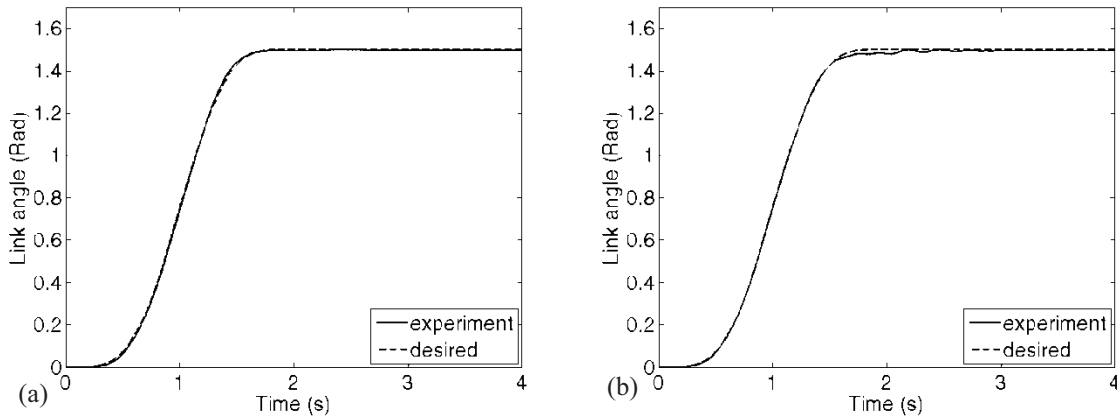
Figure 10. Experimental verification of the links' rotations for $[q_{f,shoulder}, q_{f,elbow}]_4 = [1.5\,rad, 1.5\,rad]$ **using CSTT controller, (a) shoulder link trajectory (b) elbow link trajectory**
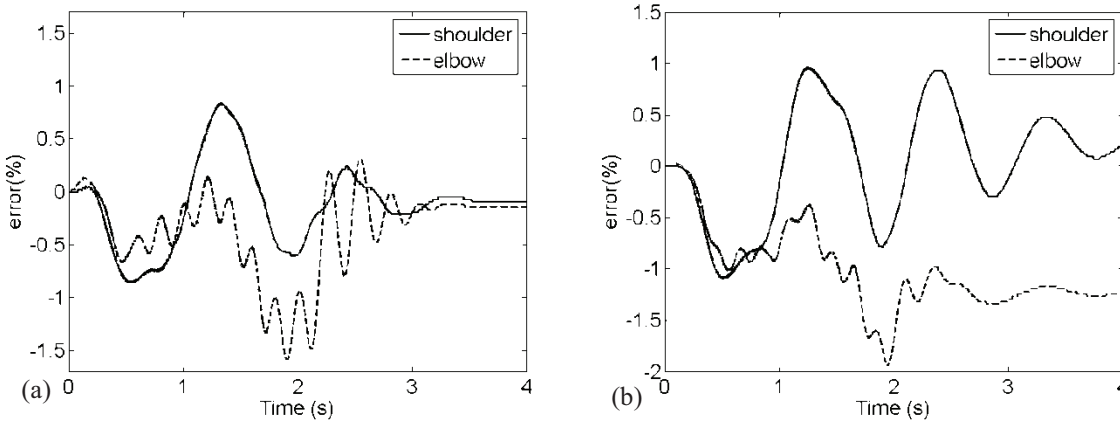
Figure 11. Experimental results: normalized tracking error for shoulder and elbow links for final rotations of $[q_{f,shoulder}, q_{f,elbow}]_1 = [1.0\,rad, 1.0\,rad]$**, using (a) CSTT controller, (b) rigid controller**
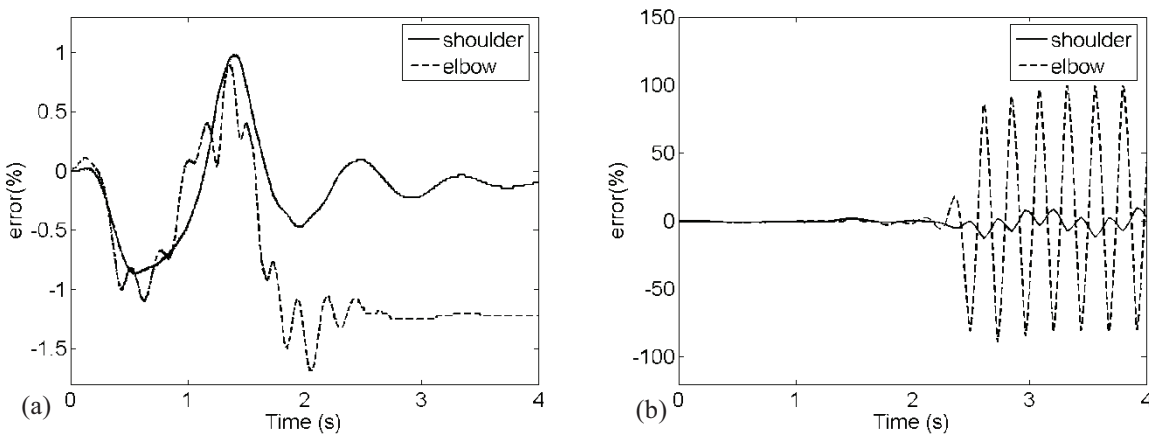
Figure 12. Experimental results: normalized tracking error for shoulder and elbow links for final rotations of $[q_{f,shoulder}, q_{f,elbow}]_2 = [1.5\,rad, 1.0\,rad]$**, using (a) CSTT controller, (b) rigid controller**
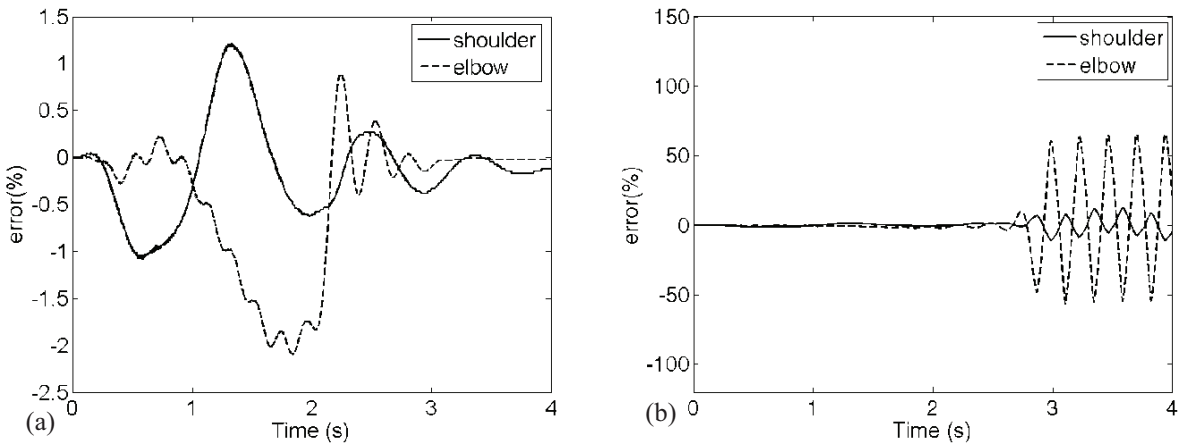
Figure 13. Experimental results: normalized tracking error for shoulder and elbow links for final rotations of
$[q_{f,shoulder}, q_{f,elbow}]_3 = [1.0\,rad, 1.5\,rad]$**, using (a) CSTT controller, (b) rigid controller**
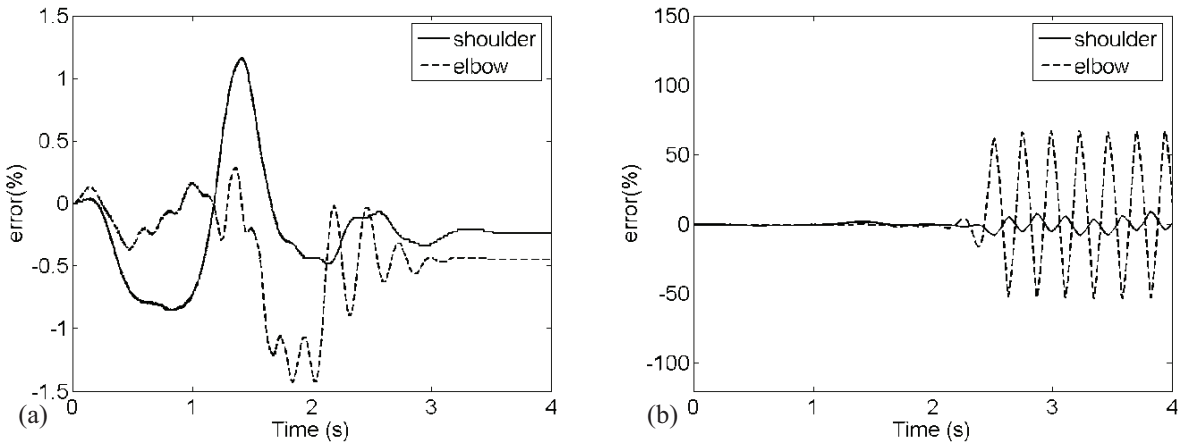
Figure 14. Experimental results: normalized tracking error for shoulder and elbow links for final rotations of
$[q_{f,shoulder}, q_{f,elbow}]_4 = [1.5\,rad, 1.5\,rad]$**, using (a) CSTT controller, (b) rigid controller**

Table 3

Experimental results: Maximum tracking error ($error_{max}$(32)) during the maneuver for the shoulder and elbow links using the CSTT and rigid controller

$[q_{f,shoulder}, q_{f,elbow}]$	Shoulder ($\times 10^{-2}$)		Elbow ($\times 10^{-2}$)	
	CSTT	Rigid	CSTT	Rigid
$[1.0\,rad, 1.0\,rad]$	0. 868	1.09	1.58	1.94
$[1.5\,rad, 1.0\,rad]$	0.984	12.6[*]	1.68	99.6[*]
$[1.0\,rad, 1.5\,rad]$	1.21	13.1[*]	2.10	65.8[*]
$[1.5\,rad, 1.5\,rad]$	1.17	8.94[*]	1.43	67.2[*]

[*]The response was unstable

Biographies

Hamid Salmasi received the B.Sc. and M.Sc. in Mechanical Engineering from the Sharif University of Technology, Tehran, Iran, in 2003 and 2005, respectively. He is currently working toward the Ph.D. degree in the Mechanical Engineering at the University of Saskatchewan, Saskatoon, Canada. His research interests include Robotics and Vibration Control.

Reza Fotouhi obtained his PhD in Mechanical Engineering from the University of Saskatchewan in Canada. He is currently a professor of Mechanical Engineering at University of Saskatchewan in Canada. His research interests include Robotics (dynamics and control), Structural Dynamics and Vibrations, Computational Mechanics, and Biomechanics.

Peter N. Nikiforuk is Dean Emeritus, College of Engineering, at the University of Saskatchewan, Canada. Previously, he was Dean of Engineering for 23 years, Head of Mechanical Engineering for 7 years and Chair of the Division of Control Engineering for 5 years. He holds the B.Sc. degree in engineering physics from Queen's University in Canada and Ph.D. degree in electrical engineering from Manchester University in England. He received the D.Sc. degree, also from Manchester University, in 1970 for research in control systems. He served as chair or member of five Councils in Canada, was recipient of seven Fellowships in Canada and England and seven other honors, and member of several Boards. His fields of research are Adaptive and Control Systems.

Chapter 3.   A manoeuvre control strategy for flexible

joint manipulators with joint dry friction

A manoeuvre control strategy for flexible joint manipulators with joint dry friction

H. Salmasi, R. Fotouhi[1] and P. N. Nikiforuk

Mechanical Engineering Department, University of Saskatchewan, 57 Campus Drive, Saskatoon, Canada, S7N 5A9

Abstract: A new control strategy based on the singular perturbation method and integral manifold concept is introduced for flexible joint manipulators with joint friction. In controllers developed so far based on the singular perturbation theory, the dynamics of actuators of flexible-joint manipulators are partially modeled, and the coupling between actuators and links are ignored. This assumption leads to inaccuracy in control performance and error in trajectory tracking which is crucial in high-precision manipulation tasks. In this paper, a comprehensive dynamic model which takes into account the coupling between actuators and links is developed and a composite controller is then designed based on the singular perturbation theorem and integral manifold concept. To overcome the joint friction, a novel method is introduced in which a linear feed-forward torque is designed using the principle of work and energy. Finally, the experimental setup of a single rigid-link flexible-joint manipulator in the Robotics Laboratory at the University of Saskatchewan was used to verify the proposed controller. Experimental results employing the new controller showed that the trajectory tracking error during and at the end of the motion of the robot manipulator was significantly reduced.

---

[1] Corresponding author

1. Introduction

A wide variety of robots is now employed in different areas such as spacecraft and vehicle manufacturing. In most of these robot manipulators, a transmission system is employed to increase the torque applied to the links and consequently to amplify the robot power. Most of controllers developed so far to control robot manipulators were based on the assumption of rigid joints; that is the transmission was assumed to be completely stiff and that there was no difference between the angular positions of the driving actuator and that of the driven link [1-6]. However, it was experimentally shown that the assumption of rigid joints generally limits a robot's ability to perform high-speed high-precision manipulations [7-12], and flexibility of the joints may produce lightly damped oscillatory motions. Especially, the effect of joint flexibility becomes more significant in robot manipulators driven by harmonic drives. While harmonic drives have zero backlash, high torque transmissibility and compact size [13-14], there is high torsional elasticity in harmonic drives which limit their capability [15]. Therefore, a more accurate control strategy in which the joint flexibility is taken into account is essential, especially in applications such as robots used in the manufacture of precision components such as circuit boards. However, because of the existence of inherent nonlinearities in the dynamic equations of flexible manipulators, developing an accurate model is difficult.

In addition to joint flexibility, another important factor which affects the performance of robot manipulators is joint friction. It has been proven that joint friction can lead to tracking errors and undesired stick-slip motion, and affects both the dynamic and static behaviours of a robot manipulator at the start, during and at the end of the motion [16-22]. Despite this, joint friction is usually neglected in modeling and control strategies developed for flexible joint manipulators, and most of the models developed for flexible joint manipulators ignore joint friction. For instance in [23] and [24] a control strategy is designed based on singular perturbation theory for tip trajectory tracking of flexible joint manipulators. However, in these works the joint friction was not considered in the dynamics of the manipulator.

In this paper a novel control strategy is introduced for the tip trajectory tracking of a flexible joint manipulator which includes two main parts:

1- Friction compensating torque which is designed so as to compensate for the friction effect.

2- Composite controller which is designed to compensate for the flexibility effect in the joints.

To compensate for the friction effect in the joints, a new friction compensation strategy is introduced in this paper. The key advantage of this strategy is that the friction compensating torque can be identified easily in two steps. In most friction models developed to predict the joint friction, an experimental identification procedure is necessary to determine the friction model parameters. This identification procedure involves a large number of experiments which need to be carried out at different velocities and requires considerable amount of time. In the proposed model, the parameters of the compensation strategy are identified in only two steps and, hence, the proposed model is more cost-effective in terms of the experimental time required to identify the parameters of the controller.

To compensate for the flexibility in the joints, a composite controller is designed based on the singular perturbation theory along with the integral manifold concept. In singular perturbation models developed for flexible-joint manipulators, e.g. in [9] and [24], the inertias of the rotors are ignored, however, ignoring any parameters in the dynamics of a system leads to inaccuracy in the performance of the controller since controllers whose design is based on the singular perturbation theory are modeled-based. This error specifically becomes more important when high precision in control is expected. In this paper, a more accurate dynamic model, which takes into account the inertias of rotors including gear reduction, is presented. While considering the effect of rotors' inertias leads to a more detailed and more complex dynamic model, it improves the precision of the controller in trajectory tracking.

Finally, the developed control strategy was experimentally verified by the experiment setup of a single rigid-link flexible-joint (SRLFJ) manipulator in the Robotics Laboratory at the University of Saskatchewan. Also, in order to assess the effectiveness of the work-energy principle based

model, experiments were performed and compared using two friction compensating strategies: a new method established based on the work-energy principle [25] and the LuGre method [18].

2. Methodology

Figure 1 shows the schematic of the control strategy that was used in the control of flexible joint manipulators. The desired trajectory q_d and its derivatives, $\dot{q}_d$ and $\ddot{q}_d$ were the inputs to the digital controller, and the rotation and velocity of the motor and link were used as feedback to the controller. The applied current was fed into the digital controller and the output digital signal to a D/A card. The analog current signal was then amplified and applied to the plant which is a flexible joint manipulator (FJM). The positions of the motor and link, q_L and q_m [2], were measured using the encoders implemented in the experimental setup and the values of the velocity were then obtained by taking the derivative of the position signals using a filter. The applied torque $\tau = \tau_f + \tau_c$ had two parts; the friction compensating torque τ_f and the composite torque τ_c. The procedures of designing these torques are described in following sections. To calculate the current required by the motor, the resultant torque τ was multiplied by the inverse of the torque constant of the motor, K_t, and the current was then fed into a D/A card. The value of the motor torque constant for the experimental setup was $K_t = 8.92\, N.m/A$ [3].

---

[2] The angle q_m measures the rotor angle after gear reduction, however, for the purpose of abbreviation, it is referred to as the motor angle in this paper.

[3] It is noteworthy that DC permanent magnet motors usually have a linear relationship to motor torque.
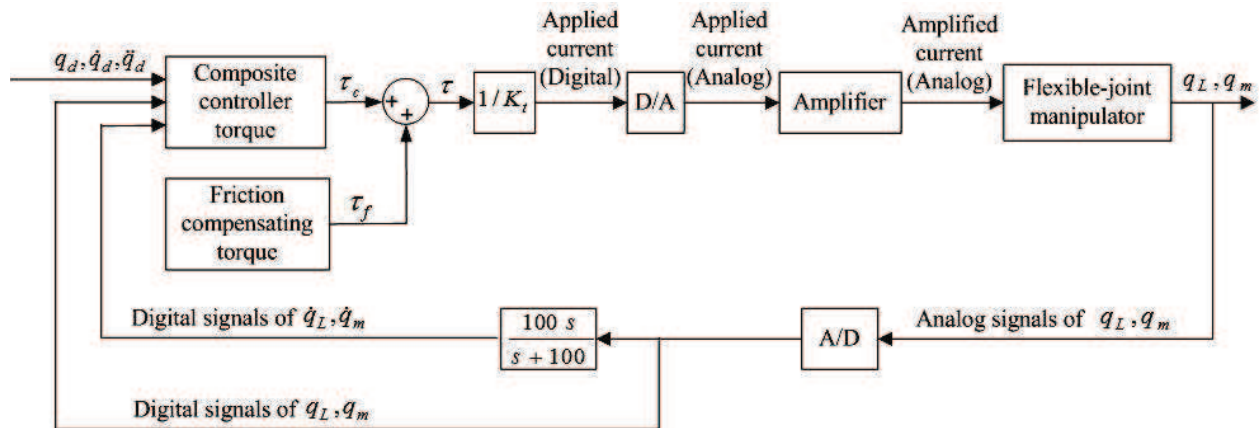
Figure 1. Control strategy designed for tip trajectory of FJM

3. Friction compensation in harmonic drives

In this section two different friction models are developed for the experimental setup of single rigid-link flexible-joint manipulator. In the first model, joint friction, τ_f, is approximated as a function of velocity based on the LuGre model, τ_f^{LG} [18]. For this purpose, the joint friction values are obtained at different velocities and the joint friction torque is then estimated as a function of velocity by the curve-fitting method. In the second model, the friction compensating torque is designed based on the work-energy principle as a feed forward linear compensating torque, τ_f^{WE}.

3.1. LuGre model

A typical friction model which describes different aspects of friction torque is the LuGre model. In this model, on the microscopic scale, surfaces sliding on each other are modeled as two rigid bodies that make contact through elastic bristles which model the random asperities[4] of the surfaces (See Figure 2). The bristles start to deflect when one surface (upper surface) starts to move and the force is then applied tangentially to the bristles of the lower surface. If the

---

[4] Regardless of how smooth a surface is, it has many random micro-scale irregularities which are called asperities.

deflection is sufficiently large, the surfaces will slide on each other. The proposed model has the mathematical form [18]

$$\frac{dy}{dt} = \dot{q}_m - \sigma_0 \frac{|\dot{q}_m|}{g(\dot{q}_m)} y, \tag{1}$$

$$\tau_f^{LG} = \sigma_0 y + \sigma_1 \frac{dy}{dt} + c_m \dot{q}_m, \tag{2}$$

where y is the average deflection of the bristles and $\dot{q}_m$ is the relative velocity between surfaces. σ_0, σ_1 and c_m are the stiffness of the bristles, damping of the bristles and viscous damping coefficient, respectively. Function $g(\dot{q}_m)$ represents the Stribeck effect which characterizes the transition between the static friction (stiction) and viscous friction, and τ_f^{LG} is the friction torque modeled based on LuGre method. Eqs. (1) and (2) are nonlinear equations describing the friction behavior based on the deflection of bristles. Since the average deflection of the bristles can not be measured directly, finding the exact solution to predict the friction behavior is not possible. However, Eqs. (1) and (2) can be simplified for the steady-state condition (sliding regime) in which the deformation rate of bristles is zero ($dy/dt=0$).
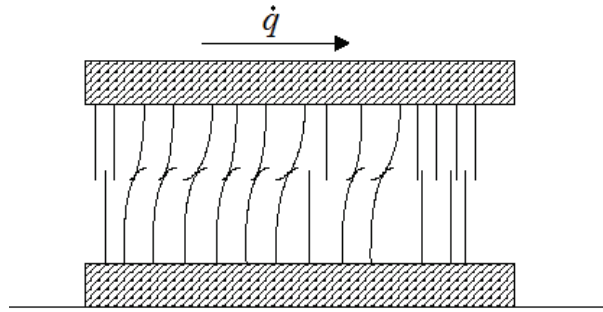
Figure 2. Two surfaces are sliding on each other; the asperities are modeled as bristles attached to the surfaces

Thus, from Eq. (1),

$$\sigma_0 y_{ss} = g(\dot{q}_m) \frac{\dot{q}_m}{|\dot{q}_m|} = \text{sgn}(\dot{q}_m) g(\dot{q}_m) \tag{3}$$

where y_{ss} is the steady-state value of the bristles deformation and the sign function is defined as

$$\text{sgn}(\dot{q}_m) = \begin{cases} 1 & \dot{q}_m > 0 \\ -1 & \dot{q}_m < 0 \end{cases} \tag{4}$$

For steady-state condition, $dy/dt = 0$, the friction torque is obtained by substituting Eq. (3) in Eq. (2)

$$\tau_f^{LG} = \text{sgn}(\dot{q}_m)g(\dot{q}_m) + c_m\dot{q}_m \tag{5}$$

A typical proposed form for the function $g(\dot{q}_m)$ is [18]

$$g(\dot{q}_m) = \tau_{fc}^{LG} + (\tau_{fs}^{LG} - \tau_{fc}^{LG})e^{-(\dot{q}_m/v_s)^2} \tag{6}$$

where τ_{fc}^{LG} and τ_{fs}^{LG} are the Coulomb friction and stiction torque respectively, and v_s is the Stribeck velocity. Replacing Eq. (6) in Eq. (5) leads to

$$\tau_f^{LG}(\dot{q}_m, \psi) = [\tau_{fc}^{LG} + (\tau_{fs}^{LG} - \tau_{fc}^{LG})e^{-(\dot{q}_m/v_s)^2}]\text{sgn}(\dot{q}_m) + c_m\dot{q}_m \tag{7}$$

where ψ is a vector which includes four constant parameters of the LuGre friction model; that is, $\psi = [\tau_{fs}^{LG} \ \tau_{fc}^{LG} \ v_s \ c_m]$. The first and second terms of the friction torque in the above equation describe the Coulomb friction and Stribeck effect respectively and the last term accounts for the viscous damping. To characterize friction torque as a function of velocity in Eq. (7), four unknown parameters, $\psi = [\tau_{fs}^{LG} \ \tau_{fc}^{LG} \ v_s \ c_m]$, must be identified. A schematic of the experimental procedure which was used to identify friction model parameters is shown in Figure 3. The motor position was controlled by a PID controller to follow a triangular wave position reference. The dynamic equation of motor is expressed as

$$J\ddot{q}_m = \tau - \tau_f \tag{8}$$

where J, τ, τ_f and $\ddot{q}_m$ are the mass moment of inertia of the motor, applied torque, joint friction and acceleration of the motor respectively. If the motor follows the reference trajectory, which is a triangular trajectory with constant velocity, the motor acceleration, $\ddot{q}_m$, will become zero and as a result the applied torque will be equal to the actual friction torque in the above equation, i.e. $\tau = \tau_f$. Therefore, the friction torque can be determined by measuring the applied torque.
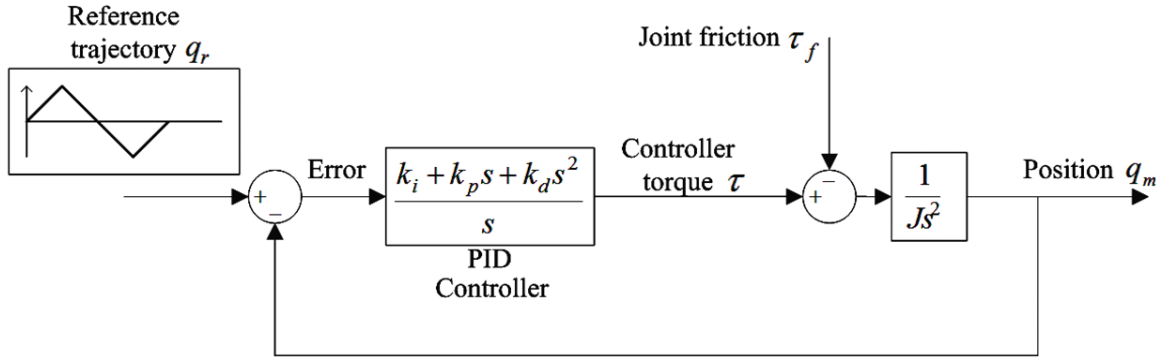
Figure 3. Schematic of the control procedure used to identify the LuGre model parameters

In total, 22 experiments were carried out in different steady-state velocities to estimate the friction torque. The experimental data were then interpolated (curve-fitted) with the LuGre friction torque τ_f^{LG} given in Eq. (7). For this purpose, the nonlinear optimization technique (MATLAB function *lsqcurvefit.m*), was used to minimize the quadratic cost function I which was defined as

$$I = \sum_{i=1}^{N}[\tau_f(\dot{q}_m^{(i)}) - \tau_f^{LG}(\dot{q}_m^{(i)}, \psi)]^2 \tag{9}$$

where $\tau_f(\dot{q}_m^{(i)})$ represents the actual joint friction torque which is measured experimentally during constant motor velocity $\dot{q}_m^{(i)}$. The torque $\tau_f^{LG}(\dot{q}_m^{(i)}, \psi)$ is the joint friction torque which is modeled based on the LuGre model and is given in Eq. (7), and N is the number of the measured data-points. The cost function I represents the error between experimental data points, $\tau_f(\dot{q}_m^{(i)})$, and the estimation function of LuGre model, $\tau_f^{LG}(\dot{q}_m^{(i)}, \psi)$. Therefore, by minimizing cost function, optimum values of $\psi = [\tau_{fs}^{LG} \ \tau_{fc}^{LG} \ v_s \ c_m]$ can be found. These values were obtained as $\psi = [1.57 -0.792 \, 0.190 \, 3.26]$ and $\psi = [-1.99 \, 0.847 \, 0.199 \, 2.93]$ for positive and negative velocities, respectively. By replacing the optimum values of the parameters in the LuGre model in the sliding regime, the friction torques can be expressed as functions of velocity

$$\tau_f^{LG} = [1.57 - 0.792 e^{-(\dot{q}_m/0.190)^2}]\text{sgn}(\dot{q}_m) + 3.26\dot{q}_m \ (N.m) \qquad \dot{q}_m > 0$$
$$\tau_f^{LG} = [-1.99 + 0.847 e^{-(\dot{q}_m/0.199)^2}]\text{sgn}(\dot{q}_m) + 2.93\dot{q}_m \ (N.m) \qquad \dot{q}_m < 0 \tag{10}$$

Figure 4 shows the experimental, τ_f, and estimated results of joint friction, τ_f^{LG}.
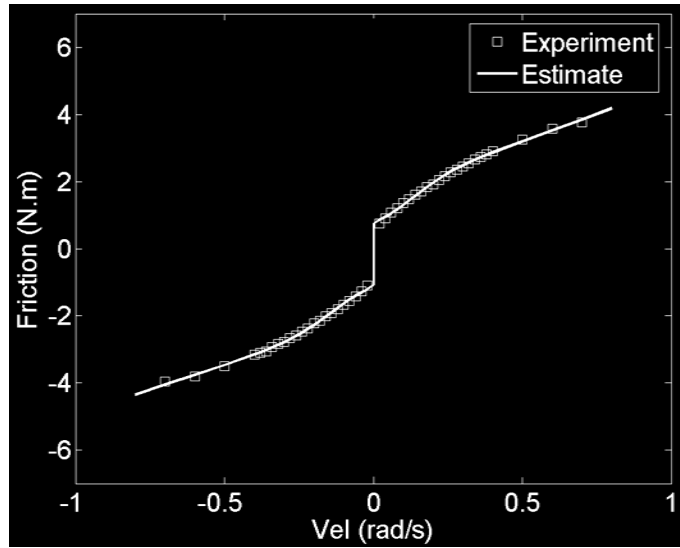
Figure 4. Comparison of experimental results with friction torque obtained in Eq. (10) based on the LuGre model

3.2. Friction model based on work-energy principle

In this section, a friction compensation strategy based on the work-energy principle is proposed. As shown in the previous section, the LuGre method, which is an approximate method for modelling the friction, requires a time-consuming identification procedure including a large number of experiments. Also, the friction torque defined in (10) is obtained based on the assumption of steady-state conditions. Therefore, it cannot model the pre-sliding regime in which the stick-slip motion occurs at very low velocities. Furthermore, the friction can change with oil temperature, load, humidity and actuator wear [21]. However, these effects are not taken into account in the friction model presented for the shoulder joint using the LuGre method. Another disadvantage of the LuGre torque given in Eq. (7) is that it assumes that the stiction at the beginning and end of the motion of the manipulator are the same, while in practice the stiction at the beginning of the manoeuvre is usually greater than that at the end. Here, a new approach is introduced for friction compensation which is identified in only two steps.

According to the work-energy principle, the work done during the motion of the flexible joint robot manipulator includes the work done by the motor torque, W_t, the energies dissipated by viscous damping, W_d, and the Coulomb friction torque, W_{df}. The total work done by the output

64

controller is composed of two parts, the work of the composite controller torque τ_c, which is W_{I_c}

and the work of the compensating torque of dry friction τ_{fd}^{WE}, which is W_{I_f}. These works can be

written as

$$W_I = \int_0^{\theta_f} \tau \, dq_m = \int_0^{t_f} \tau \, \dot{q}_m \, dt = \int_0^{t_f} (\tau_c + \tau_{fd}^{WE}) \dot{q}_m \, dt = \int_0^{t_f} \tau_c \dot{q}_m \, dt + \int_0^{t_f} \tau_{fd}^{WE} \dot{q}_m \, dt = W_{I_c} + W_{I_f} \quad (11)$$

where θ_f and t_f are the final rotation of the joint and the time at which link reaches its final

position, respectively, and $W_{I_c} = \int_0^{t_f} \tau_c \dot{q}_m \, dt$ and $W_{I_f} = \int_0^{t_f} \tau_{fd}^{WE} \dot{q}_m \, dt$. The energy dissipated by the

viscous damping is

$$W_d = \int_0^{\theta_f} c_m \, \dot{q}_m \, dq_m = \int_0^{t_f} c_m \, \dot{q}_m^2 \, dt \quad (12)$$

The energy dissipated by the dry Coulomb friction, τ_{fc}, can be written as

$$W_{df} = \int_0^{\theta_f} \tau_{fc} \, dq_m = \int_0^{t_f} \tau_{fc} \, \dot{q}_m \, dt \quad (13)$$

The principle of work and energy for a general system is

$$K_2 = \sum W_{1 \to 2} + K_1 \quad (14)$$

where $\sum W_{1 \to 2}$ expresses the total work done by the forces (conservative and non-conservative)

on the system from the initial position 1 to the final position 2, and K_1 and K_2 are total kinetic

energy of the system at the initial and final positions, respectively. Since the velocity is zero at

the initial and final positions, K_1 and K_2 are zero and Eq. (14) reduces to

$$\sum W_{1 \to 2} = 0 \quad (15)$$

Thus

$$\sum W_{1 \to 2} = W_{I_c} + W_{I_f} - W_d - W_{df} = 0 \quad (16)$$

and the work done by τ_{fd}^{WE} can be obtained as

$$W_{I_f} = -W_{I_c} + W_d + W_{df} \quad (17)$$

Hence,

$$\int_0^{t_f} \tau_{fd}^{WE} \, \dot{q}_m \, dt = -W_{I_c} + W_d + W_{df} \quad (18)$$

65

The friction compensating torque, τ_{fd}^{WE}, can now be obtained from Eq. (18). There are many candidates for the friction compensating torque function which satisfies Eq. (18). For convenience, the friction compensating torque was assumed to be linear form, that is

$$\tau_{fd}^{WE} = \begin{cases} a+bt & 0<t<-(a/b) \\ 0 & t>-(a/b) \end{cases}$$

(19)

Thus, Eq. (18) becomes

$$\int_0^{t_f}(a+bt)\dot{q}_m\,dt = -W_{I_c}+W_d+W_{df}$$

(20)

Parameter a is the torque required to overcome stiction and initiate motion of the manipulator from the rest position. The parameter b can then be obtained using above equation. The friction torque obtained in Eq. (19) includes the dry friction effect. To obtain the total friction torque, the viscous friction effect, $c_m\dot{q}_m$, must be added to the torque in Eq. (19), and hence

$$\tau_f^{WE} = \begin{cases} a+bt+c_m\dot{q}_m & 0<t<-(a/b) \\ c_m\dot{q}_m & t>-(a/b) \end{cases}$$

(21)

where τ_f^{WE} is the joint friction torque which includes dry and viscous effects. While the friction torque obtained based on the work-energy principle in Eq. (21) has fewer parameters and a simpler form compared to the LuGre model in Eq. (10), it is more accurate in compensating for the friction. For instance, the experimental results in Section 5.2 for a SRLFJ show that by using τ_f^{WE} the trajectory tracking error is significantly reduced in contrast to the results obtained by using the LuGre method.

4. Composite controller

In this section, a composite controller is designed for tip trajectory tracking of flexible-joint manipulators. In the composite controllers developed so far to control of flexible joint manipulators, the dynamic coupling between the actuators and the links is ignored (e.g. [24] and [20]). This leads to the fact that the off-diagonal terms in the mass matrix in the dynamic model become zero and the dynamic model of flexible joint manipulator is simplified. However, ignoring the coupling between the actuators and the links leads to the error in the performance of the controller since in singular perturbation theory the controller is model-based and any error in

the dynamic model causes the deficiency in the control performance. To remove this error, all coupling effects between the actuators and the links are considered in the dynamic model developed in this paper and consequently it provides more accuracy in the control of flexible-joint manipulators.

4.1. Singularly perturbed systems

The standard governing equations of a singularly perturbed system are [26-27]

$$\dot{X} = f(X, Z, \varepsilon, t), \quad X(t_0) = X^0, \quad X \in R^n \tag{22}$$

$$\varepsilon \dot{Z} = g(X, Z, \varepsilon, t), \quad Z(t_0) = Z^0, \quad Z \in R^m \tag{23}$$

where ε represents a small parameter, X and Z are state vectors of dimensions n and m, respectively, $f \in R^n$, $g \in R^m$, and $\dot{X}$, $\dot{Z}$, X^0 and Z^0 are the time derivatives and initial conditions of states X and Z, respectively. State Z is called the *fast state* of the system because ε is a small parameter and the time variation of Z is very large (Eq. (23)). In contrast, state X is called the *slow state* of the system because it has a slower time variation compared with state Z.

For Eqs. (22) and (23), which represent the $(n+m)$ dimensional state-space equations of X and Z, depending on the parameter ε, there is an integral manifold M_ε which represents the m-dimensional set of equations and is defined as

$$M_\varepsilon : Z = \varphi(X, \varepsilon); \quad X \in R^n, Z \in R^m \tag{24}$$

where φ is a function of state X and time. Since Z in Eq. (24) is the solution of Eq. (23), it has to satisfy the following integral manifold condition

$$\varepsilon \dot{Z} = \varepsilon \frac{\partial \varphi}{\partial X} f(X, \varphi(X, \varepsilon)) = g(X, \varphi(X, \varepsilon)) \tag{25}$$

If Eq. (25) is satisfied, fast states Z can be replaced by the integral manifold $\varphi(X, \varepsilon)$ in Eq. (22). This leads to

$$\dot{X} = f(X, \varphi(X, \varepsilon), \varepsilon, t), \quad X(t_0) = X^0, \quad X \in R^n \tag{26}$$

The resultant model in Eq. (26) is called the reduced-order model since it includes only the slow states X and has an order of n compared to the original system Eqs. (22) and (23) which has an order of $(n+m)$. Thus, as long as the fast state Z moves on the integral manifold, that is $Z = \varphi(X, \varepsilon)$, instead of the original system Eqs. (22) and (23), the reduced-order model Eq. (26) can be used to describe the dynamics of the slow states. On the other hand, if Eq. (25) is not satisfied there will be the difference η between Z and φ, i.e. $\eta = Z - \varphi(X, \varepsilon)$. In the control approach based on the integral manifold, two controllers are designed. The first one, called the fast controller, is designed to remove the difference between the fast state and the integral manifold, and as a result $\eta \rightarrow 0$ and $Z = \varphi(X, \varepsilon)$. The second controller, the slow controller, is designed to control the slow states in the reduced-order model (Eq.(26)). Therefore, using the singular perturbation theory along with the integral manifold concept allows for the decomposing system into fast and slow subsystems, and controllers are then designed for each subsystem separately.

Fast and slow subsystems can be obtained from the singularly perturbed equations of the system, Eqs. (22) and (23), in terms of X and η

$$\dot{X} = f(X, \varphi(X, \varepsilon) + \eta), \quad X(t_0) = X^0 \tag{27}$$

$$\varepsilon \dot{\eta} = \varepsilon \dot{Z} - \varepsilon \dot{\varphi}(X, \varepsilon) = \varepsilon \dot{Z} - \varepsilon \frac{\partial \varphi(X, \varepsilon)}{\partial X} \dot{X} =$$

$$g(X, \varphi(X, \varepsilon) + \eta) - \varepsilon \frac{\partial \varphi(X, \varepsilon)}{\partial X} f(x, \varphi(X, \varepsilon) + \eta), \quad \eta(t_0) = \eta^0 \tag{28}$$

where η^0 is the vector of the initial condition of the fast states η. In fact, Eq. (27) describes the slow variations of the state X, and Eq. (28) represents the dynamic of the fast state η. It is clear that if $\eta = 0$, Eq. (28) will be the same as Eq. (25), which means that the manifold condition is satisfied and Z moves on its manifold.

4.2. Singularly perturbed model of flexible joint manipulators

The dynamic equations of a serial manipulator consisting of n-rigid links connected by $(n-1)$ elastic joints are described by the following set of differential equations

$$D(q_L)\ddot{q}_L + C_l(q_L,\dot{q}_L)\dot{q}_L + K(q_L - q_m) = H(\tau - \tau_f) \tag{29}$$

$$J\ddot{q}_m - K(q_L - q_m) = \tau - \tau_f \tag{30}$$

where $D(q_L) \in R^{n \times n}$ is the inertia matrix of the links, $C_l(q_L,\dot{q}_L)\dot{q}_L$ represents the Coriolis and centrifugal effects, $K \in R^{n \times n}$, defined as $K = diag(k_1,\cdots,k_n)$, represents the stiffness of the joints, $J \in R^{n \times n}$ is the inertia matrix of the motors, and τ is the vector of applied torques through the motors, respectively. Also, $q_L \in R^n$ and $q_m \in R^n$ represent, respectively, the rotations of the links and the motors. The components of matrix H are defined as $H_{ij} = -1$ when $i = j-1$, and $H_{ij} = 0$ when $i \neq j-1$. The correctness of dynamic equations (29)-(30) has been verified using finite-element analysis (FEA) for the two-rigid-link flexible-joint manipulator ($n = 2$). The details are given in Appendix I.

As stated earlier, the applied torque τ includes two parts; composite torque τ_c and friction compensating torque τ_f. That is

$$\tau = \tau_c + \tau_f \tag{31}$$

As a result, the joint friction can be eliminated from the dynamic equations of the manipulator and hence,

$$D(q_L)\ddot{q}_L + C_l(q_L,\dot{q}_L)\dot{q}_L + K(q_L - q_m) = H\tau_c \tag{32}$$

$$J\ddot{q}_m - K(q_L - q_m) = \tau_c \tag{33}$$

In the following, the application of the singular perturbation theory and the integral manifold concept is applied to control flexible joint manipulators. Based on the singular perturbation approach, the system is first decomposed into two subsystems, slow and fast, and controllers are then designed for each subsystem. The slow subsystem represents the low-frequency motion of the flexible manipulator where the working frequency range depends on the flexibility of the joints. For instance, if the joint flexibility goes to infinity, the slow subsystem reduces to a rigid

manipulator in which the manipulator manoeuvre will be a rigid body motion (zero frequency). The fast subsystem deals with the motion of the manipulator at higher frequency vibration.

If all the spring constants k_i are assumed to be of the same order of magnitude, they can be written as a multiple of a single large parameter $\bar{k}$,

$$k_i = \bar{k}\,\tilde{k}_i, \quad i=1,\cdots,n \tag{34}$$

and the elastic joint torque is,

$$\xi = \bar{k}\tilde{K}(q_L - q_m) \tag{35}$$

where

$$\tilde{K} = diag\,(\tilde{k}_1,\cdots,\tilde{k}_n)$$

Without loss of generality (by rescaling the ξ variables if necessary), the matrix $\tilde{K}$ is chosen as $\tilde{K}=I$. The singular perturbation parameter can now be defined as $\mu = 1/\bar{k}$, and Eq. (35) becomes

$$\mu\xi = q_L - q_m \tag{36}$$

Then by using Eq. (36), Eqs. (32) and (33) become

$$\ddot{q}_L = -D^{-1}(C_l\dot{q}_L + \xi - H\tau_c) \tag{37}$$

$$\ddot{q}_m = J^{-1}(\xi + \tau_c) \tag{38}$$

Setting $x=q_l$ and subtracting Eq. (38) from (37), one obtains

$$\ddot{x} = -D^{-1}(C_l\dot{x} + \xi - H\tau_c) \tag{39}$$

$$\mu\ddot{\xi} = J^{-1}[-\xi + (JD^{-1}H - I)\tau_c] - D^{-1}(C_l\dot{x} + \xi) \tag{40}$$

Eqs. (39) and (40) represent the singularly perturbed model of the flexible joint manipulators. These equations can be written as

$$\ddot{x} = a_1(x,\dot{x}) + a_2(x)\xi + a_3(x)\tau_c \tag{41}$$

$$\mu\ddot{\xi} = b_1(x,\dot{x})\dot{x} + b_2(x)\xi + b_3(x)\tau_c \tag{42}$$

where

$$a_1(x,\dot{x}) = -D^{-1}C_l\dot{x}, \quad a_2(x) = -D^{-1}, \quad a_3(x) = D^{-1}H$$

$$b_1(x,\dot{x})=-D^{-1}C_l,\ b_2(x)=-(J^{-1}+D^{-1}),\ b_3(x)=D^{-1}H-J^{-1}$$

Moreover, the state-space representation of the singularly perturbed system, Eqs. (41) and (42),

can be obtained by choosing $x_1=x$, $x_2=\dot{x}$, $z_1=\xi$ and $z_2=\varepsilon\dot{\xi}$ where $\varepsilon=\sqrt{\mu}$. Thus

$$\dot{X}=A_1(X)+A_2(X)Z+A_3(X)\tau_c \tag{43}$$

$$\varepsilon\dot{Z}=B_1(X)X+B_2(X)Z+B_3(X)\tau_c \tag{44}$$

where

$$X=[x_1\quad x_2]^T_{1\times 2n},\ Z=[z_1\quad z_2]^T_{1\times 2n}$$

$$A_1=\begin{bmatrix}x_2\\a_1(x_1,x_2)\end{bmatrix}_{2n\times 1},\ A_2=\begin{bmatrix}O_{n\times n}&O_{n\times n}\\a_2(x_1)&O_{n\times n}\end{bmatrix}_{2n\times 2n},\ A_3=\begin{bmatrix}O_{n\times n}\\a_3(x)\end{bmatrix}_{2n\times n}$$

$$B_1=\begin{bmatrix}O_{n\times n}&O_{n\times n}\\O_{n\times n}&b_1(x_1,x_2)\end{bmatrix}_{2n\times 2n},\ B_2=\begin{bmatrix}O_{n\times n}&I_{n\times n}\\b_2(x_1,x_2)&O_{n\times n}\end{bmatrix}_{2n\times 2n},\ B_3=\begin{bmatrix}O_{n\times n}\\b_3(x_1,x_2)\end{bmatrix}_{2n\times n}$$

4.2.1. Recovery of the rigid robot manipulator

In the following it will be shown that by setting $\mu=0$ the equation of motion of the rigid

manipulator will be recovered. In an ideal rigid manipulator, joints stiffness must tend to infinity,

i.e. $K\rightarrow\infty$, and as a result $\mu\rightarrow 0$. Therefore, the flexible joint manipulator in Eqs. (41) and (42),

must behave as a rigid manipulator when $\mu=0$. Setting $\mu=0$ in Eqs. (41) and (42), leads to

$$\ddot{x}=a_1(x,\dot{x})+a_2(x)\xi+a_3(x)\tau_c \tag{45}$$

$$0=b_1(x,\dot{x})\dot{x}+b_2(x)\xi+b_3(x)\tau_c \tag{46}$$

Solving (46) for ξ and substituting the result in (45), leads to

$$\ddot{x}=a_1(x,\dot{x})-a_2(x)b_2^{-1}(x)[b_1(x,\dot{x})\dot{x}+b_3(x)\tau_c]+a_3(x)\tau_c \tag{47}$$

Employing the definitions of a_1, a_2, b_1, b_2 and b_3, Eq. (47) becomes

$$\ddot{x}=-D^{-1}C_l\dot{x}+D^{-1}(J^{-1}+D^{-1})^{-1}[D^{-1}C_l\dot{x}+(J^{-1}-D^{-1}H)\tau_c]+D^{-1}H\tau_c \tag{48}$$

and after some algebraic manipulations, Eq. (48) yields (see Appendix II for details)

$$\ddot{x} = (J + D)^{-1}[-C_I \dot{x} + (H + I)\tau_c] \qquad (49)$$

which are the dynamic equations of the counterpart of the flexible joint manipulator when the

joints are rigid [28].

4.2.2. Integral manifold implementation

According to the definition of the integral manifold in Eq. (24), an integral manifold for a

flexible joint manipulator in the space R^{2n} is

$$M_\varepsilon : Z = \varphi(X, \tau_c, \varepsilon, t); \quad X \in R^{2n} \qquad (50)$$

If Z moves on the integral manifold, Z can be substituted by the integral manifold φ in

Eq. (44), and therefore

$$\varepsilon \dot{\varphi} = B_1(X)X + B_2(X)\varphi + B_3(X)\tau_c \qquad (51)$$

The reduced order model of the system is then

$$\dot{X} = A_1(X) + A_2(X)\varphi + A_3(X)\tau_c \qquad (52)$$

As discussed in Section Two, as long as Z is on the integral manifold φ, the original governing

equations of the system, Eqs. (43) and (44), reduce to its reduced-order model, Eq. (52). Thus,

provided that the fast state Z is restricted to move on the integral manifold, the controller can be

only designed to control the slow state X in Eq. (52). It is a very significant advantage of using

the integral manifold concept, because the controller will be designed for the reduced-order

model of dimension n, while the original system has a dimension of $n + m$. The design

procedure of the controller is discussed in the following section.

4.2.3. Composite controller design procedure

Here, a composite controller torque which consists of slow and fast controllers is proposed. The

slow controller, $\tau_{c,s}$, is designed to control the slow subsystem which presents the low-frequency

motion of the manipulator. If the joint flexibility goes to infinity, the slow subsystem reduces to a

rigid manipulator and the slow controller will be equal to the controller torque for the rigid

manipulator, $\tau_{c,0}$, which can be obtained by using the inverse-dynamic approach [29]. The fast

controller, $\tau_{c,f}$, is selected to suppress the high-frequency vibration of the manipulator. Thus the composite controller τ_c can be written as the summation of slow and fast controller torques as

$$\tau_c = \tau_{c,s}(X,Z,\dot{X},\dot{Z}) + \tau_{c,f}(X,Z,\dot{X},\dot{Z}) \tag{53}$$

The difference between Z and the integral manifold φ, is

$$\eta = Z - \varphi(X,\tau_{c,s},\varepsilon,t) \tag{54}$$

and replacing Eqs. (44) and (51) in Eq. (54) results in

$$
\begin{aligned}
\varepsilon\dot{\eta} &= \varepsilon\dot{Z} - \varepsilon\dot{\varphi}(X,\tau_{c,s},\varepsilon,t) \\
&= B_1(X)X + B_2(X)Z + B_3(X)\tau_c - \\
&\quad \{B_1(X)X + B_2(X)\varphi + B_3(X)\tau_{c,s}\} \\
&= B_2(X)\eta + B_3(X)\tau_{c,f}
\end{aligned}
\tag{55}
$$

It is worth noting that once Z is on the integral manifold, η will be zero and as a result $\tau_{c,f}$ will be zero and the control torque has only the slow controller, i.e. $\tau_c = \tau_{c,s}(X,Z,\dot{X},\dot{Z})$.

From Eqs. (43) and (55) the equations of the slow and fast subsystems in state space are

$$\dot{X} = A_1(X) + A_2(X)\varphi + A_2(X)\eta + A_3(X)\tau_c \tag{56}$$

$$\varepsilon\dot{\eta} = B_2(X)\eta + B_3(X)\tau_{c,f} \tag{57}$$

Eq. (56) describes the low-frequency motion of the robot manipulator and Eq. (57) represents the high-frequency motion of the robot manipulator.

Designing slow controller

In this section, the slow controller $\tau_{c,s}$ is designed using perturbation method. For this purpose, the integral manifold φ and the slow controller $\tau_{c,s}$ are expanded in terms of ε

$$\varphi_{c,s} = \varphi_0 + \varepsilon\varphi_1 + \varepsilon^2\varphi_2 + \cdots \tag{58}$$

$$\tau_{c,s} = \tau_{c,0} + \varepsilon\tau_{c,1} + \varepsilon^2\tau_{c,2} + \cdots \tag{59}$$

For a manipulator with rigid joints (i.e. $\varepsilon \to 0$), the slow controller reduces to $\tau_{c,0}$ which can be designed based on the conventional methods available for the rigid manipulators such as the inverse-dynamic approach [29]. In order to determine the other parts of the slow controller, (i.e. $\tau_{c,1}, \tau_{c,2}, \cdots$), Eqs. (58) and (59) are substituted into integral manifold condition Eq. (51). Therefore,

$$\varepsilon(\dot{\varphi}_0 + \varepsilon \dot{\varphi}_1 + \varepsilon^2 \dot{\varphi}_2 + \cdots) = B_1(X)X + B_2(X)(\varphi_0 + \varepsilon\varphi_1 + \varepsilon^2 \varphi_2 + \cdots) + \\ B_3(X)(\tau_{c,0} + \varepsilon\tau_{c,1} + \varepsilon^2\tau_{c,2} + \cdots) \tag{60}$$

Equating the coefficients with the same power of ε leads to

$$0 = B_1(X)X + B_2(X)\varphi_0 + B_3(X)\tau_{c,0} \tag{61}$$

$$\dot{\varphi}_0 = B_2(X)\varphi_1 + B_3(X)\tau_{c,1} \tag{62}$$

$$\dot{\varphi}_1 = B_2(X)\varphi_2 + B_3(X)\tau_{c,2} \tag{63}$$

$$\dot{\varphi}_i = B_2(X)\varphi_{i+1} + B_3(X)\tau_{c,i+1} \quad i = 2,3,\cdots \tag{64}$$

From Eqs. (61) to (64), φ_0, φ_1 and φ_i $i = 2,3,\cdots$ will be found in terms of $\tau_{c,i}$, iteratively. From Eq. (61)

$$\varphi_0 = -B_2^{-1}(X)[B_1(X)X + B_3(X)\tau_{c,0}] \tag{65}$$

According to the definition of matrices B_1, B_2 and B_3, the last n components of vector $\varphi_0 \in R^{2n}$ are zero; that is, φ_0 can be written as

$$\varphi_0 = [(\varphi_{01})_{n\times1} \quad O_{n\times1}]_{2n\times1} \tag{66}$$

where φ_{01} represents first n components of vector $\varphi_0 \in R^{2n}$. If the second part of integral manifold, φ_1, is written as

$$\varphi_1 = [(\varphi_{11})_{n\times1} \quad (\varphi_{12})_{n\times1}]_{2n\times1} \tag{67}$$

using the definition of the matrices B_1, B_2 and B_3, Eq. (65) leads to

$$\begin{cases} \dot{\varphi}_{01} = \varphi_{12} \\ 0 = b_2(X)\varphi_{11} + b_3(X)\tau_{c,1} \end{cases} \tag{68}$$

By setting $\tau_{c,1} = 0$, φ_{11} becomes zero in Eq. (68). Also, substituting φ_1 in Eq. (63), results in

$$\begin{cases} 0 = \varphi_{22} \\ \dot{\varphi}_{12} = b_2(X)\varphi_{21} + b_3(X)\tau_{c,2} \end{cases} \tag{69}$$

where φ_{21} and φ_{22} represent, respectively, the first and second n components of vector $\varphi_2 \in R^{2n}$. If $\tau_{c,2}$ is now chosen as

$$\tau_{c,2} = b_3^{-1}\dot{\varphi}_{12} \tag{70}$$

then from Eq. (69) $\varphi_{21} = 0$ and consequently $\varphi_2 = 0$. Also, the terms containing φ_i $i = 3,4,\cdots$, will become zero by setting $\tau_{c,i} = 0$ $i = 3,4,\cdots$, in Eq. (64). Therefore

$$\varphi_i = 0 \quad i = 3,4,\cdots \tag{71}$$

Consequently, from Eqs. (58) and (59), the terms of φ and $\tau_{c,s}$ are expressed in the following form

$$\varphi = \varphi_0 + \varepsilon\varphi_1 \tag{72}$$

$$\tau_{c,s} = \tau_{c,0} + \varepsilon^2 b_3^{-1}\dot{\varphi}_{12} \tag{73}$$

Designing fast controller

As discussed in Section 4.1., the fast controller must be selected so that the difference between the integral manifold and parameter Z asymptotically goes to zero; that is $\eta \to 0$. If the fast controller $\tau_{c,f}$ is chosen to have the state-feedback format

$$\tau_{c,f} = B_4\eta \tag{74}$$

where B_5 is a constant matrix, then Eq. (57) becomes

$$\varepsilon\dot{\eta} = [B_2(X) + B_3(X)]B_4\eta \tag{75}$$

If the elements of matrix B_4 are chosen so that the eigenvalues of the square matrix $[B_2(X) + B_3(X)B_4]$ always have negative real parts, the deviation of Z from its manifold will asymptotically go to zero and, finally, Z will be on its invariant manifold.

5. Experimental verification

In order to verify the design of the controller described in the previous section, the experimental single rigid-link flexible-joint manipulator (SRLFJ) available at Robotics Laboratory of the University of Saskatchewan was used. Figure 5 shows the experimental module of the SRLFJ that was used.
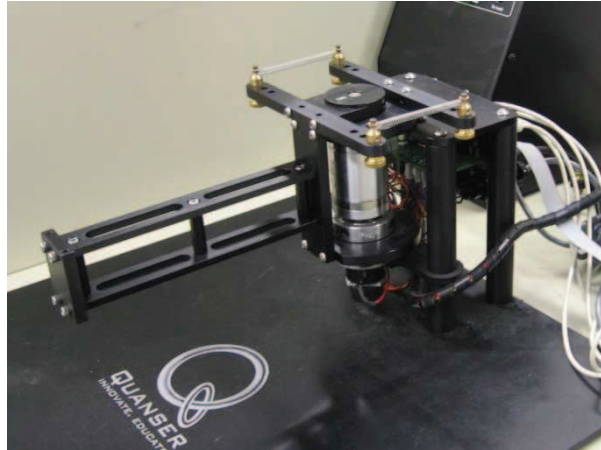
Figure 5. Experimental module single rigid-link flexible-joint manipulator used

5.1. Experimental setup

The experimental module of the SRLFJ included a servo harmonic drive and a rigid link, as well as two parallel linear springs to represent the joint stiffness. Since the parallel springs applied a torque proportional to $(q_L - q_m)$, they were modeled as a torsional spring. The numerical values of the experimental setup parameters were

$$j_L = 0.209 \, kg.m^2, \quad j_m = 0.0110 \, kg.m^2, \quad c_m = 3.26 \, N.m.s/rad, k = 10.3 N.m/rad, \, l = 0.223m$$

where j_L, j_m and l are, respectively, the mass moment of inertias of the link and motor, and the length of the link. The moments of inertia of the link and motor were calculated using the CAD model, and the information provided by the manufacturer of the motor, respectively. The viscous damping of the motor was determined from the torque impulse test.

Four different trajectories were chosen to verify the performance of the controller at different velocities and accelerations. These trajectories were

$$q_d^{(1)} = [70(t/t_f)^9 - 315(t/t_f)^8 + 540(t/t_f)^7 - 420(t/t_f)^6 + 126(t/t_f)^5]\theta_f \qquad (76)$$

$$q_d^{(2)} = [-20(t/t_f)^7 + 70(t/t_f)^6 - 84(t/t_f)^5 + 35(t/t_f)^4]\theta_f \qquad (77)$$

$$q_d^{(3)} = [6(t/t_f)^5 - 15(t/t_f)^4 + 10(t/t_f)^3]\theta_f \qquad (78)$$

$$q_d^{(4)} = [-2(t/t_f)^3 + 3(t/t_f)^2]\theta_f \qquad (79)$$

where the final position was $\theta_f = 0.5\,rad$ and the time required to reach the final position was $t_f = 2\,\sec$. In all of these trajectories the motion of the manipulator started from $q_d^{(i)}(0) = \dot{q}_d^{(i)}(0) = 0, \quad i = 1, 2, 3, 4$ and reached the final position where $q_d^{(i)}(t_f) = \theta_f, \dot{q}_d^{(i)}(t_f) = 0 \quad i = 1, 2, 3, 4$. Furthermore, the first and the second proposed trajectories were designed such that $d^i q_d^{(1)} / dt^i = 0, \quad i = 2, 3, 4$, and $d^i q_d^{(1)} / dt^i = 0, \quad i = 2, 3$ at $t = 0$ and at $t = t_f$, respectively. Also, for the third trajectory the acceleration of the manipulator was set to zero at $t = 0$ and $t = t_f$. The experimental results for each of these desired trajectories are shown in Section 5.2.

5.2. Friction compensating torque

Based on the approach discussed in Section 3, two compensating friction torques were designed based on the work-energy principle and the LuGre method. To design a friction compensating torque based on the work-energy principle, as discussed in Section 3.2, two parameters, a and b, must be identified to determine the friction compensating torque $\tau_{fd}^{WE} = a + bt$ in Eq. (19). Parameter a, the breakaway force, was obtained experimentally by increasing the torque gradually, until the manipulator started to move, as shown in Figure 6. This torque was about as $1.2\,N.m$. To obtain the parameter b from Eq. (20), the work of the composite controller torque, and the dissipated energies by coulomb dry friction and viscous damping during motion of the manipulator were calculated using Eqs. (11), (12) and (13) respectively. The values of work W_{I_c}, W_d and W_{df} were obtained experimentally by calculating the areas under the curves in Figures 7-9 as

$$W_{I_c} = 1.0377 \ J, \quad W_d = 0.6995 \ J, \quad W_{df} = 0.4975 \ J$$

From Eq. (17), the work of the compensating friction torque must be

$$W_{I_f} = 0.1574 J$$

Finally, by solving numerically Eq. (20), coefficient b can be obtained as

$$b = -0.9941 N \cdot m/s$$

Therefore, based on the work-energy principle explained in Section 3.2 and according to equation (21) the friction compensating torque including the viscous friction became

$$\tau_f^{WE(1)} = -t + 1.2 + 3.26 \dot{q}_m \ N \cdot m$$

Also, two other friction compensating torques were selected as

$$\tau_f^{WE(2)} = -1.2t + 1.2 + 3.26 \ \dot{q}_m \ N \cdot m$$

$$\tau_f^{WE(3)} = -0.8t + 1.2 + 3.26 \dot{q}_m \ N \cdot m$$

to ensure that the parameter   was selected properly in Eq. (82). Another compensating torque was

$$\tau_f^{LG} = 1.57 - 0.792 e^{-(\dot{q}_m / 0.190)^2} + 3.26 \ \dot{q}_m \ N.m$$

which was obtained based on the LuGre model explained in Section 3.1. The simulation and experimental results are shown in Figure 10 for friction torques based on the work-energy principle and the LuGre friction torque for the desired trajectory $q_d^{(1)}$. The results for other desired trajectories, $q_d^{(2)}$, $q_d^{(3)}$ and $q_d^{(4)}$, are shown later in this section.
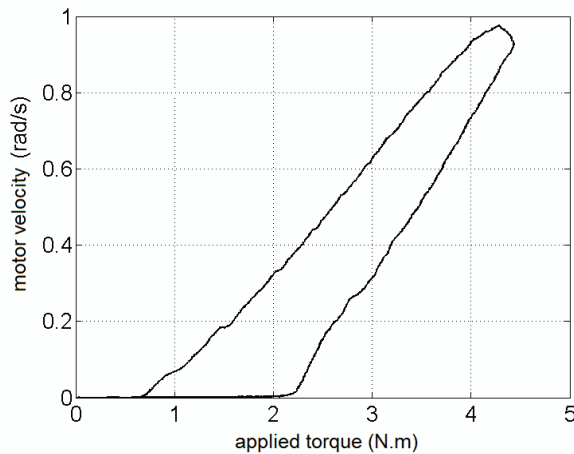
Figure 6. The motor velocity response corresponding to the applied triangle torque to obtain experimentally a in Eq. (19)
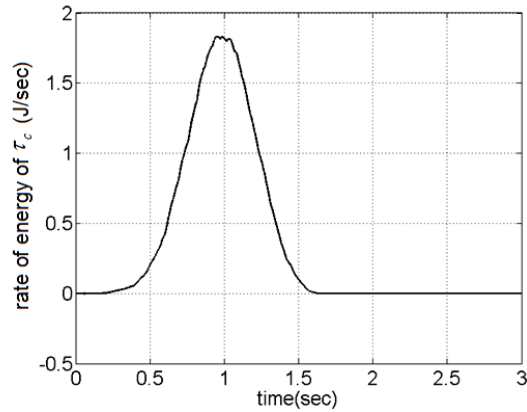
Figure 7. The rate of the energy of the controller torque τ_c applied to the flexible joint manipulator to obtain W_{I_m} from Eq. (11) for manoeuvre $\theta_f = 0.5\,rad$ during two seconds
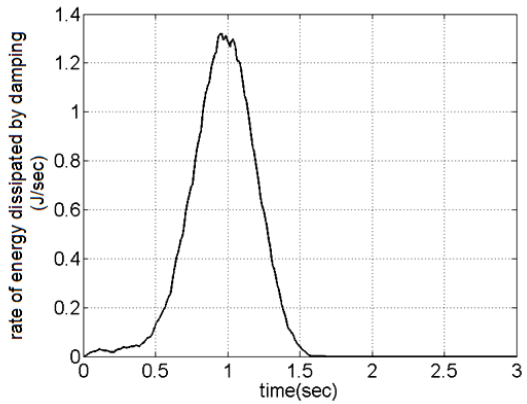
Figure 8. The rate of the dissipated energy by viscous damping to obtain W_d from Eq. (12) for manoeuvre $\theta_f = 0.5\,rad$ during two seconds
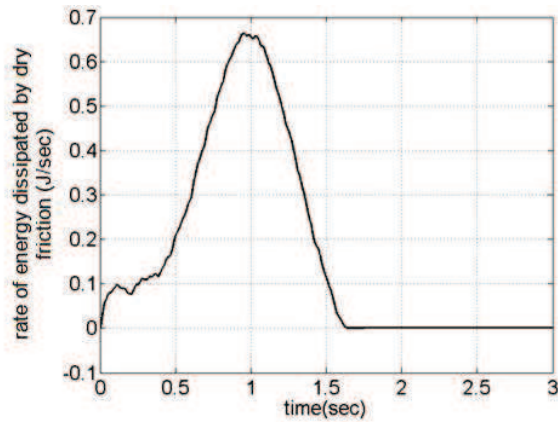
Figure 9. The rate of the dissipated energy by dry friction to obtain W_{df} from Eq. (13) for manoeuvre $\theta_f = 0.5\,rad$ during two seconds

As shown in Figure 10a by using the friction compensating torque τ_f^{LG} whose design was based on the LuGre model, the error was significant, especially there was a considerable steady-state error at the end of trajectory. This error occurred since in reality the frictions at the beginning and at the end of the motion were different due to hysteresis [30] (see Figure 6), while friction compensating torque τ_f^{LG} did not include the hysteresis effect and was the same for the beginning and end of the motion of the manipulator (see the corresponding torque in Figure 11a). There was also a significant error between desired trajectory and link rotation when friction torques $\tau_f^{WE(2)}$ and $\tau_f^{WE(3)}$, Eqs. (84) and (85), were used. In fact, by feeding less energy into the system, using $\tau_f^{WE(2)}$, the manipulator moved behind the desired trajectory and the error remained as a negative value at the end of the motion of the robot manipulator. In contrast, by using $\tau_f^{WE(3)}$, the input energy into system was more than the required energy to overcome the friction and viscous damping of the system combined. Consequently, the link moved beyond the desired trajectory and the error became as a positive value at the end of the motion. The experimental results for torques $\tau_f^{WE(2)}$ and $\tau_f^{WE(3)}$ are not shown here for brevity. The tracking error for $\tau_f^{WE(1)}$ is shown in Figure 10b, where the tracking error at the end of the manipulator manoeuvre was approximately zero; and during the manipulator motion this error remained in an acceptable range. The corresponding applied torque is shown in Figure 11b.

Furthermore, according to the simulation results in Figure 10, the tracking error was almost zero for both cases, the LuGre model and the WE model. That indicates that the friction compensating torque was able to compensate for the joint friction almost completely, and the theoretical model developed for flexible-joint manipulator with joint-friction given in Eqs. (32) and (33) was accurate. In the experimentation, however, there were other factors which were not possible to model them exactly (such as the effect of position and load on the friction), and consequently, there were error in the friction compensation in the experiments.

To have a better assessment of the results, the root mean square error (RMSE) and steady-state error (SSE) are defined, respectively, as

$$RMSE = (\frac{1}{t_f} \int_0^{t_f} e^2 \cdot dt)^{1/2} \tag{87}$$

$$SSE = \left| \frac{e(t_f)}{\theta_f} \right| \times 100 \tag{88}$$

where $e = q_L - q_d^{(1)}$. The RMSE shows the error between the link angle and the desired trajectory during the motion of the robot manipulator and the SSE represents the steady-state error at the end of the manipulator manoeuvre. A summary of the results in terms of the RMSE and values of SSE are illustrated in Table 1 for different friction compensating torques, and the results are then compared in Figure 12. It can be observed that the RMSE and SSE for $\tau_f^{WE(1)}$ have the minimum value of the RMSE and SSE and it can be chosen as the best candidate.
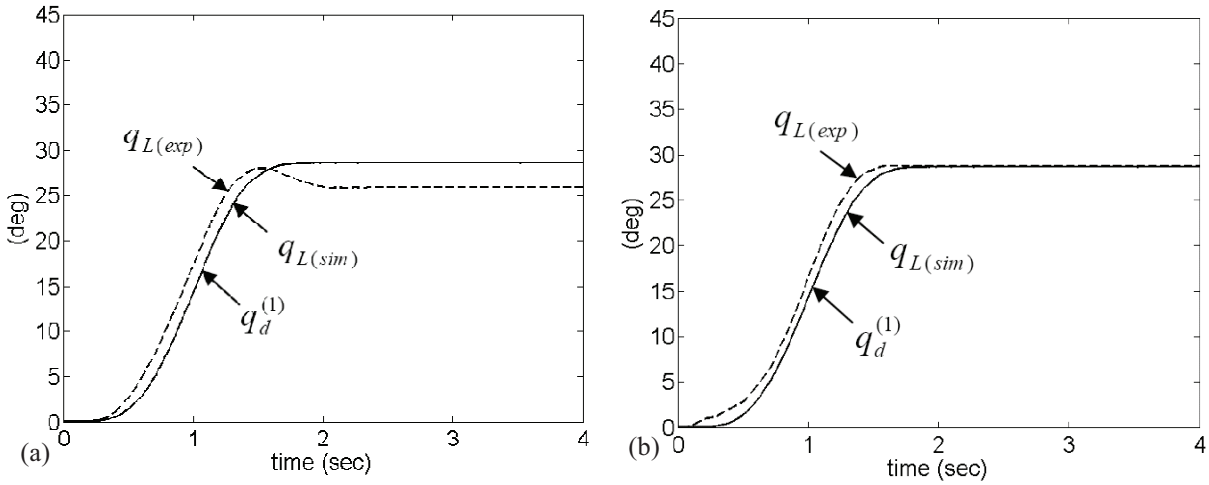
Figure 10. Comparing simulation and experimental results of manipulator manoeuvre using composite controller and different friction compensation torques, (a) τ_f^{LG} **in Eq. (86), (b)** $\tau_f^{WE(1)}$ **in Eq. (83) (link angle** q_L **and the first desired trajectory** $q_d^{(1)}$ **)**
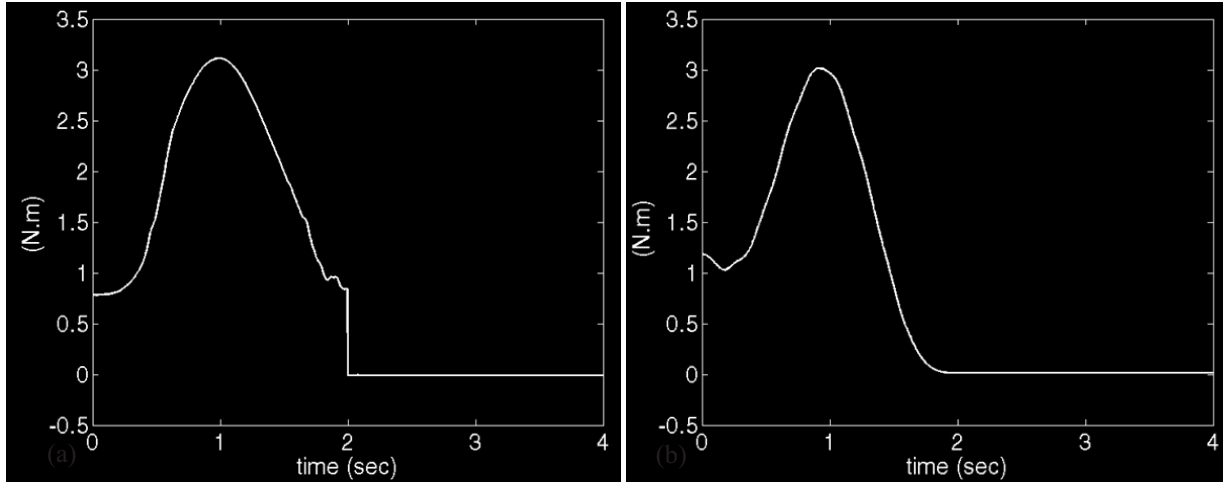
Figure 11. Applied torque to the flexible-joint manipulator of motions in Fig. 10 (a) $\tau_{c,s} + \tau_f^{LG}$**, (b)** $\tau_{c,s} + \tau_f^{WE(1)}$

Table 1.Values of error norm RMSE and SSE for different friction compensating torques for the composite controller for a SRLFJ experimental setup

Friction compensating torque (N.m)	RMSE ($\times 10^{-2}$)	SSE (%)
$\tau_f^{WE(1)}$ (Eq. 83)	2.55	0.428
$\tau_f^{WE(2)}$ (Eq. 84)	4.16	14.6
$\tau_f^{WE(2)}$ (Eq. 85)	4.25	8.43
τ_f^{LG} (Eq. 86)	3.44	9.72
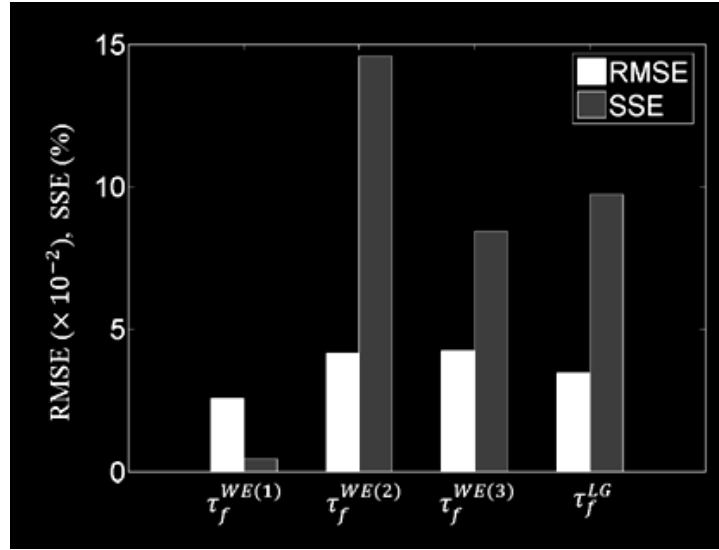
Figure 12. Comparison values of error norms RMSE and SSE for different friction compensating torques for the composite controller for a SRLFJ experimental setup

To verify that the designed friction compensating torque, $\tau_f^{WE(1)}$, acted accurately at different, trajectories, the performance of $\tau_f^{WE(1)}$ was examined for other desired trajectories $q_d^{(2)}$, $q_d^{(3)}$ and $q_d^{(4)}$ given in Eqs. (77) to (79). The results are compared in Figure 13. As shown in this figure, the manipulator follows the desired trajectories accurately. Therefore, it can be concluded that the controller works with different trajectories, from the smooth ninth order to less smooth third order.

5.3. Composite controller

In this section the effectiveness of the composite controller designed for SRLFJ is studied. The results of composite controller were compared with the results of the rigid controller $\tau_{c,0}$. The rigid controller $\tau_{c,0}$ was based on the assumption of a rigid joint and is shown in Figure 14a, and the composite controller $\tau_{c,s}$ is shown in Figure 14b. The corresponding response is compared with the desired trajectory in Figure 15 for the rigid controller. It can be seen that there is a significant tracking error between the desired trajectory and the link angle during the motion of

the link $(t < t_f)$ and a noticeable SSE at the end of the manipulator manoeuvre $(t > t_f)$. However, by using the composite controller torque these errors were significantly reduced (see Figure 16). For instance, the value of SSE in Eq. (88) was computed as $0.026/0.50 = 5.2\%$ when the rigid controller was used, but decreased to 0.42% when the composite controller was used. Furthermore, the value of RMSE, which indicates the tracking error during the motion of the link, decreased from 4.10×10^{-2} *rad* for the rigid controller, to 2.55×10^{-2} *rad* for the composite controller. In fact, the rigid controller was not able to reduce the tracking error during the manoeuvre $(t < 2)$, to reach a small value before the end of the manoeuvre $(t = 2)$; the SSE remained large after $(t > 2)$ because of the stiction. In contrast to the rigid controller, the composite controller had a better performance in tracking; the tracking error relatively was small during the manoeuvre, and the SSE remained small after $(t > 2)$. In both approaches, the torque based on work-energy principle, $\tau_f^{WE(1)}$, was employed to compensate for the friction, as this torque provided a better result compared to the LuGre torque.
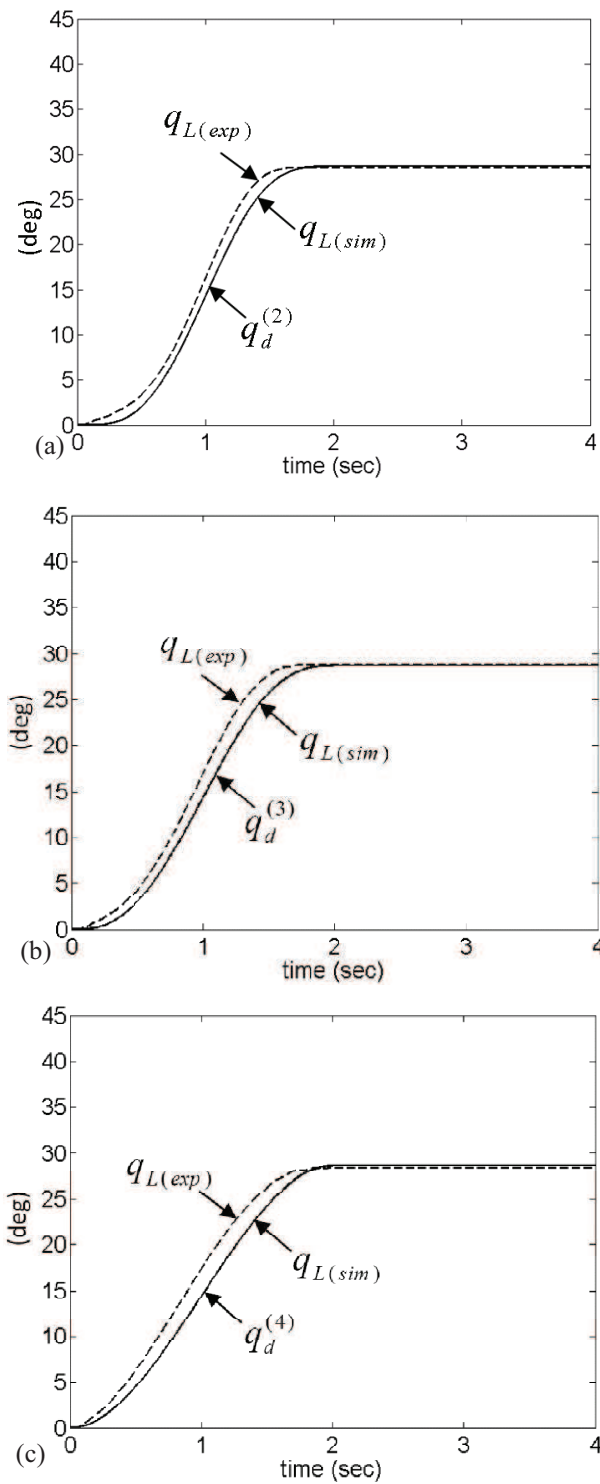
Figure 13. Comparing simulation and experimental results of the flexible joint manipulator manoeuvre using composite controller with link angle q_L for (a) desired trajectory $q_d^{(2)}$, (b) desired trajectory $q_d^{(3)}$, (c) desired trajectory $q_d^{(4)}$
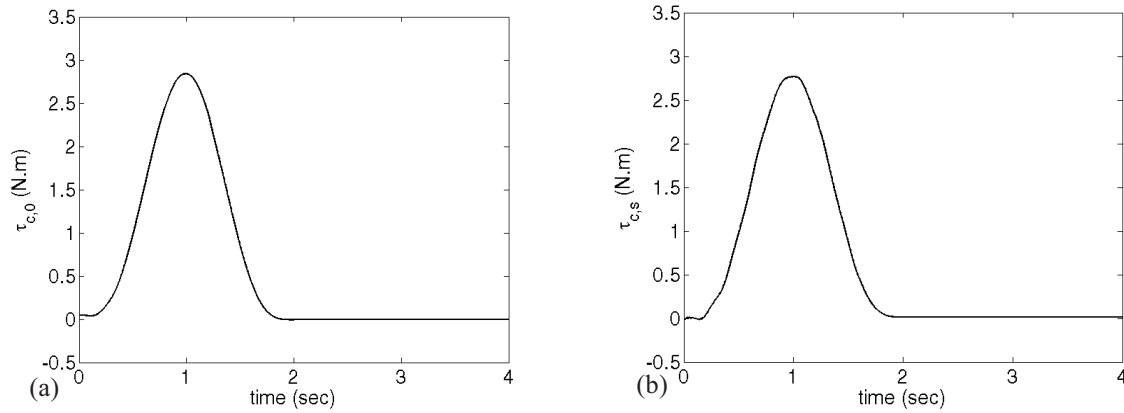
Figure 14. (a) Rigid controller torque, $\tau_{c,0}$, based on the assumption of rigid joint, (b) composite controller torque $\tau_{c,s}$ for a SRLFJ
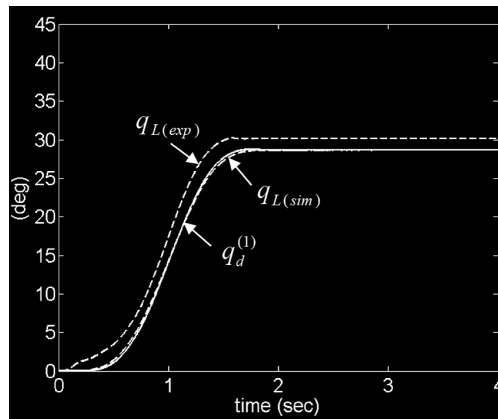
Figure 15. Comparing simulation and experimental results of manipulator manoeuvre with rigid controller torque (link angle q_L and the desired trajectory $q_d^{(1)}$) for a SRLFJ
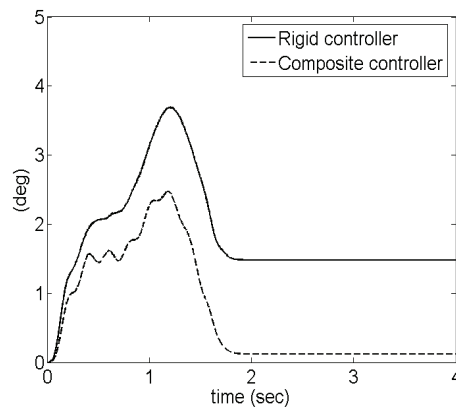
Figure 16. Tracking error, $e = q_L - q_d^{(1)}$, between the actual link, q_L, and the desired trajectory of the link angle $q_d^{(1)}$, for the rigid controller torque and composite controller for a SRLFJ experimental setup

6. Conclusion

In this study, a general control strategy for tip trajectory tracking of flexible-joint manipulators with friction was presented and experimentally validated. The first part of the controller was a linear feed-forward torque whose design was based on the work-energy principle and it was developed to compensate for the friction in the joints. The design of the second part of the controller was based on the singular perturbation theory and the integral manifold, and it was developed to compensate for the joints' flexibility. In contrast to other controllers whose designs were based on the singular perturbation theory, the dynamic coupling between the links and actuators was considered in the dynamic modeling of the manipulators in this study. As a result, the model presented in this paper provided more accurate dynamic modeling and control of flexible-joint manipulators.

The simulation and experimental results verified the effectiveness of the designed controllers. The first part of experiments was performed to determine the efficiency of the friction compensating strategy. Comparing this strategy with other methods such as LuGre method confirmed the effectiveness of the proposed strategy. For instance, the steady-state error, SSE, was significantly reduced from 9.72% by using the LuGre method to 0.428% by using new proposed friction compensating torque. Also, the accuracy of the controller was verified at different trajectories to make sure that the controller acts precisely at different velocities and accelerations.

The second part of the experiments was carried out to determine the effectiveness of the composite controller. In these experiments, it was found that the tracking error was considerably reduced during the motion of the robot arm such that the value of RMSE was decreased from 4.10×10^{-2} *rad* for the rigid controller to 2.55×10^{-2} *rad* for the composite controller. The maximum value of the steady-state error at the end of the manipulator was only 0.428% using the composite controller, while using rigid controller this figure was 5.2%. Thus, using the new proposed controller would be recommended for robot manipulation tasks in which high-accuracy in trajectory tracking is desired.

7. References

1. R. Fotouhi, H. Salmasi, S. Dezfulian and R. Burton "Design and control of a hydraulic simulator for a flexible joint robot," *Advanced Robotics* **23(**6) (2009).

2. M. W. Spong, "Control of flexible joint robots: a survey, University of Illinois," *Coordinate Science Laboratory, College of Engineering, UILU-ENG-90-2203*, February 1990.

3. H. Diken, "Frequency-response characteristics of a single-link flexible joint manipulator and possible trajectory tracking," *Journal of Sound and Vibration* **233**(2), 179-194 (2000).

4. B. O. Al-Bedoor and A. A. Almusallam, "Dynamics of flexible-link and flexible-joint manipulator carrying a payload with rotary inertia," *Mechanism and Machine Theory* **35**(6), 785-820 (2000).

5. S. K. Spurgeon, L. Yao and X. Y. Lu, "Robust tracking via sliding mode control for elastic joint manipulators," *Proceedings of IMechE, Part I (Journal of Systems and Control Engineering)*, **215(**4), 405-17 (2001).

6. A. Benallegue, "Adaptive control for flexible joint robots using a passive systems approach," *Control Engineering Practice* **3**(10), 1393-1400 (1995).

7. K. Khorasani , "Adaptive control of flexible joint robots," *Proceedings of IEEE International Conference on Robotics and Automation*, Sacramento, California (April 1991), vol. (3), pp. 2127-2134.

8. M. Readman, "Flexible Joint Robots," CRC Press, Boca Raton, Florida, 1994.

9. M.C. Han and Y. H. Chen, "Robust control design for uncertain flexible-joint manipulators: A singular perturbation approach," *Proceedings of the IEEE Conference on Decision and Control*, **1**, 611-616 (1993).

10. D. Wang, "A simple iterative learning controller for manipulators with flexible joints," *Automatica*, **31**(9), 1341-1344 (1995).

11. C. J. B. Macnab and G. M. T. D'Eleuterio, "Neuroadaptive control of elastic-joint robots using robust performance enhancement", *Robotica* **19**(6), 619-629 (2001).

12. N. Jalili, "An infinite dimensional distributed base controller for regulation of flexible robot arms," *Journal of Dynamic Systems, Measurement and Control* **123**(4), 712-19 (2001).

13. A. Albu-Schaffer, C. Ott and G. Hirzinger, "A unified passivity-based control framework for position, torque and impedance control of flexible joint robots," *International Journal of Robotics Research* **26**(1), 23-39 (2007).

14. M. Spong, K. Khorasani and P. Kokotovic, "An integral manifold approach to the feedback control of flexible joint robots," *IEEE Journal of Robotics and Automation* **3**(4), 291-300 (1987).

15. L. Sweet and M. Good, "Redefinition of the robot motion-control problem," *IEEE Control Systems Magazine* **5**(3), 18-25 (1985).

16. H. Abdellatif, B. Heimann, "On compensation of passive joint friction in robotic manipulators: modeling, detection and identification," *IEEE International Conference on Control Applications*, Munich, (October 2006) pp. 2510-2515.

17. G. Liu , A.A. Goldenberg and Y. Zhang, "Precise slow motion control of a direct-drive robot arm with velocity estimation and friction compensation," *Mechatronics* **14**(7), 821-834 (2004).

18. C. Canudas de Wit, H. Olsson, K. J. Astrom and P. Lischinsky, "A new model for control of systems with friction," *IEEE Transactions on Automatic Control* **40**(3), 419-425 (1995).

19. M. K. Ciliz, "Adaptive control of robot manipulators with neural network based compensation of frictional uncertainties," *Robotica* **23(**2), 159-67 (2005).

20. P. Tomei, "Robust adaptive friction compensation for tracking control of robot manipulators," *IEEE Transactions on Automatic Control* **45**(11), 2164-9 (2000).

21. J. C. Piedboeuf, J. de Carufel and R. Harteau, "Friction and stick-slip in robots: simulation and experimentation," *Multibody System Dynamics* **4**(4), 341-354 (2000).

22. M. Grotjahn, M. Daemi and B. Heimann, "Friction and rigid body identification of robot dynamics," *International Journal of Solids and Structures* **38**(10), 1889-1902 (2001).

23. B. Subudhi and A. S. Morris, "Singular perturbation based neuro-H∞ control scheme for a manipulator with flexible links and joints," *Robotica* **24**(2), 151-161 (2006).

24. F. Ghorbel and M. W. Spong, "Integral manifolds of singularly perturbed systems with application to rigid-link flexible-joint multibody systems," *International Journal of Non-linear Mechanics* **35**(1), 133-155 (2000).

25. J. H. Ginsberg, "Advanced engineering dynamics," Cambridge University Press, Second Edition (1995).

26. P. V. Kokotovic, H. K. Khalil and J. O'Reiley, "Singular perturbation methods in control: analysis and design," Academic Press, New York, (1986).

27. B. Siciliano and W. J. Book, "A singular perturbation approach to control of lightweight flexible manipulators," *The International Journal of Robotics Research* **7**(4), 79-90 (1988).

28. A. Ferrara and L. Magnani, "Motion control of rigid robot manipulators via first and second order sliding modes," *Journal of Intelligent and Robotic Systems* **48**(1), 23-36 (2007).

29. S. Torres, J. A. Mendez , L. Acosta and V. M. Becerra, "On improving the performance in robust controllers for robot manipulators with parametric disturbances," *Control Engineering Practice* **15**(5), 557-566 (2007).

30. B. Armstrong-Hélouvry, "Control of Machines with Friction," Kluwer Acadamic Publishers, Norwell, USA (1991).

Appendix I. Dyamic equations of two-rigid-link flexible joint manipulator

Equations (29) and (30) were derived using the Euler-Lagrange method. For instance, for a two-rigid-link flexible-joint manipulator, equations (29) and (30) were written as

$$
\begin{bmatrix} D_{11} & D_{12} \\ D_{21} & D_{22} \end{bmatrix} \begin{bmatrix} \ddot{q}_{l_1} \\ \ddot{q}_{l_2} \end{bmatrix} + \begin{bmatrix} 0 & C_{l_1} \\ C_{l_2} & 0 \end{bmatrix} \begin{bmatrix} \dot{q}_{l_1} \\ \dot{q}_{l_2} \end{bmatrix} + \begin{bmatrix} k_1 & 0 \\ 0 & k_2 \end{bmatrix} (\begin{bmatrix} q_{l_1} \\ q_{l_2} \end{bmatrix} - \begin{bmatrix} q_{m_1} \\ q_{m_2} \end{bmatrix}) = \begin{bmatrix} H_{11} & H_{12} \\ H_{21} & H_{22} \end{bmatrix} \begin{bmatrix} \tau_1 \\ \tau_2 \end{bmatrix} \tag{A1}
$$

$$
\begin{bmatrix} J_{11} & 0 \\ 0 & J_{22} \end{bmatrix} \begin{bmatrix} \ddot{q}_{m_1} \\ \ddot{q}_{m_2} \end{bmatrix} - \begin{bmatrix} k_1 & 0 \\ 0 & k_2 \end{bmatrix} (\begin{bmatrix} q_{l_1} \\ q_{l_2} \end{bmatrix} - \begin{bmatrix} q_{m_1} \\ q_{m_2} \end{bmatrix}) = \begin{bmatrix} \tau_1 \\ \tau_2 \end{bmatrix} \tag{A2}
$$

where

$D_{11} = I_{l_1} + m_{l_1} l_{c_1}^2 + m_{l_2} l_1^2 + m_t l_1^2 + I_{h_2} + m_{h_2} l_1^2,$

$D_{12} = m_{l_2} l_1 l_{c_2} \cos(q_{l_2} - q_{l_1}) + m_t l_1 l_2 \cos(q_{l_2} - q_{l_1}),$

$D_{21} = D_{12},$

$D_{22} = I_{l_2} + m_{l_2} l_{c_2}^2 + I_t + m_t l_2^2$

$C_{l_1} = -(m_{l_2} l_1 l_{c_2} + m_t l_1 l_2) \sin(q_{l_2} - q_{l_1}) \dot{q}_{l_2},$

$C_{l_2} = (m_{l_2} l_1 l_{c_2} + m_t l_1 l_2) \sin(q_{l_2} - q_{l_1}) \dot{q}_{l_1},$

$J_{11} = I_{r_1},$

$J_{22} = I_{r_2},$

$H_{11} = 0,$

$H_{12} = -1,$

$H_{21} = 0,$

$H_{22} = 0,$

For $i = 1,2$, parameter τ_i was the applied torque to joint i; m_{l_i} was the mass of link i; m_t was the mass of the manipulator's tip; l_i was the length of link i; l_{c_i} was the distance of the center of mass of link i from joint i axis. Parameters I_{l_i}, I_t, I_{h_i} and I_{r_i} were respectively mass moments of inertia of link i, manipulator's tip, hub of joint i, and rotor of joint i. Also, in equations (A1) and (A2) rotations of links q_{l_i} and rotations of joints q_{m_i} were measured in the absolute coordinate frames. The frame of the first link (shoulder link) was a Cartesian coordinate fixed to the first joint (shoulder joint). The frame of the second link (elbow link) was also a Cartesian coordinate system fixed to the second joint (elbow joint), and parallel to the shoulder frame during the motion.

The numerical values used for verification were $\tau_1 = 0.3\ N \cdot m$, $\tau_2 = 0.1\ N \cdot m$, $l_1 = l_2 = 0.5\ m$, $l_{c_1} = l_{c_2} = 0.25\ m$, $I_{r_1} = I_{r_2} = 1 \times 10^{-3}\ kg \cdot m^2$, $I_{h_1} = I_{h_2} = 3 \times 10^{-4}\ kg \cdot m^2$, $I_t = 1 \times 10^{-3}\ kg \cdot m^2$, $k_1 = k_2 = 30\ N \cdot m/rad$, $m_{l_1} = m_{l_2} = 0.39\ kg$, $I_{l_1} = I_{l_2} = 8.1 \times 10^{-3}\ kg \cdot m^2$, $m_t = 0.2\ kg$, $m_{h_1} = m_{h_2} = 0.2\ kg$. The correctness of dynamic equations of (A1) and (A2) were validated using finite-element analysis (FEA). The results for rotations of shoulder link and shoulder joint are compared in Figure A.1. According to this figure, the results of FEA and theoretical approach confirm each other.
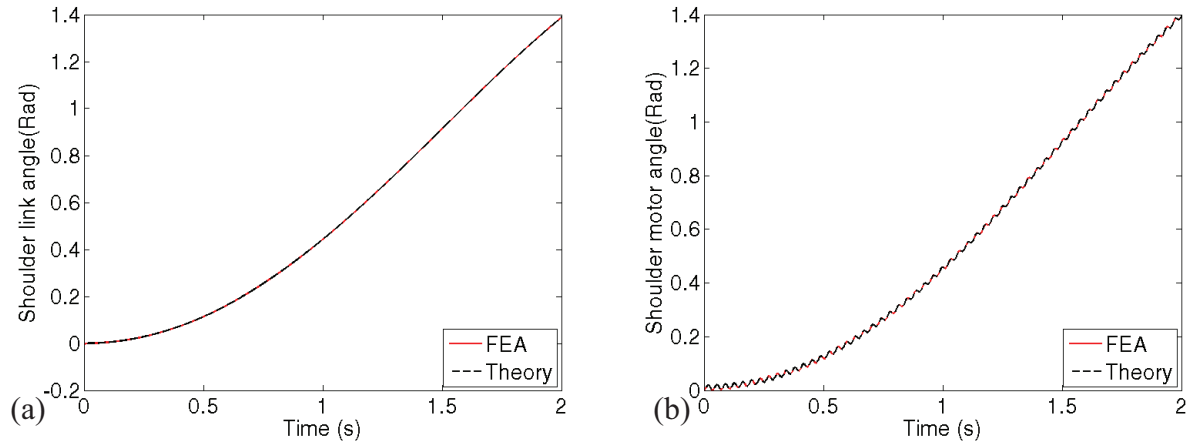
Figure AI.1. Comparison results of finite-element analysis and theoretical method for a two-rigid-link flexible-joint manipulator, (a) shoulder link rotation, and (b) shoulder joint rotation

Appendix II. Deriving the dynamic equations of the flexible joint manipulator for $\mu = 0$

Eq. (48) can be written as

$$
\begin{aligned}
\ddot{x} &= -D^{-1}C_l \dot{x} + D^{-1}[D(J+D)^{-1}J][D^{-1}C_l\dot{x} + (J^{-1} - D^{-1}H)\tau_c] + D^{-1}H\tau_c \\
&= [-D^{-1} + (J+D)^{-1}JD^{-1}]C_l\dot{x} - (J+D)^{-1}\tau_c - D^{-1}[J(J+D)^{-1}D]D^{-1}H\tau_c + D^{-1}H\tau_c \\
&= -(J+D)^{-1}[(J+D)D^{-1} - JD^{-1}]C_l\dot{x} + (J+D)^{-1}\tau_c - D^{-1}J(J+D)^{-1}H\tau_c + D^{-1}H\tau_c \\
&= -(J+D)^{-1}C_l\dot{x} + (J+D)^{-1}\tau_c + [-D^{-1}J + D^{-1}(J+D)](J+D)^{-1}H\tau_c \\
&= -(J+D)^{-1}C_l\dot{x} + (J+D)^{-1}\tau_c + (J+D)^{-1}H\tau_c \\
&= (J+D)^{-1}[-C_l\dot{x} + (H+I)\tau_c]
\end{aligned}
$$

Chapter 4.   A biologically-inspired controller for tip trajectory tracking of flexible-joint manipulators

A BIOLOGICALLY-INSPIRED CONTROLLER FOR TIP TRAJECTORY TRACKING OF FLEXIBLE-JOINT MANIPULATORS

H. Salmasi, R. Fotouhi and P. N. Nikiforuk

Mechanical Engineering Department, University of Saskatchewan, Saskatoon, Canada

Email: {hamid.salmasi, reza.fotouhi, peter.nikiforuk}@usask.ca

Abstract: This paper presents a new biologically-inspired control strategy for tip trajectory tracking of flexible-joint manipulators. The social behavioural pattern of swarms such as bird flocks and fish schools is the inspiration to develop a new controller for flexible joint manipulators in this study. This controller, referred to as swarm control, is a self-organized robust technique which is able to control the rotations of the joints and the position of the robot end-effector simultaneously. Therefore, in contrast to other studies in which the joints are individually controlled, and the performance of the controller is independent of the position of the end-effector, the swarm control takes into account the errors in the positions of the end-effector and the joints at the same time. In this control scheme, the parameters of the controller are updated every time-step based on their values at the previous time step and also the feedbacks of the positions of the links and the end-effector. Along with the swarm control, a friction compensating torque which is based on the LuGre method is employed to counterbalance the effect of the friction in the joints. Verification of the proposed controller is performed using the experimental setup of a two rigid-link flexible-joint. The experimental results show that the controller is successful in tip trajectory tracking at several different desired trajectories and at several different speeds, such that the tracking error and the steady-state errors are almost zero

during the manoeuvre of the manipulator and after reaching to the final desired position. Furthermore, experimental comparison with the computed torque scheme demonstrates the superiority of the swarm control strategy as the maximum end-effector error is reduced by a factor of three by using the swarm control scheme.

Keywords: Flexible joint manipulators, biologically-inspired swarm control, tip trajectory tracking.

1. Introduction

In most robot applications, such as spacecraft and automotive industries, the control of the end-effector of the manipulator (e.g. welding tool) is the main concern. In these applications, a desired trajectory is usually specified in the task-space and the robot end-effector (the tip) is required to follow this prescribed trajectory. To achieve this task, a mapping is determined between the robot end-effector and the rotations of the joints, and based on the desired trajectory of the end-effector, the desired rotations of the joints are computed. A control strategy is then designed such that the error between rotations of the joints and their desired trajectories are minimized. Therefore, the position of the end-effector is indirectly controlled. This method has been widely employed in different control strategies. They include feedback linearization [1], singular perturbation techniques [2,3], integral manifold approach [4], adaptive control [5-8], iterative approaches [9], robust [10] and neuroadaptive methods [11]. However, the main drawback of these control methods is that the joints are controlled separately, and the error in the end-effector position is not taken into account in the control procedure. Therefore, it is possible that while the error in the joints rotations are kept small, the error at the end-effector position becomes very significant. This can happen because, for serial robot manipulators, the end-

effector position is a trigonometric function of the joints position, and not a linear function of the rotations of the joints.

The main concept of the swarm control strategy which is introduced in this paper is inspired by the real biological systems. Populations such as swarms of birds or schools of fishes often move in coordinated but localized efforts toward a particular target [12]. In fact, by simply adjusting the trajectory of each individual toward its own best location the swarm finds its best position at each time step [13]. For instance, when a swarm of birds (or a school of fish) is moving towards a specific destination, each bird (or fish) has to follow a desired path so that the entire group moves towards the target. In this paper, we employ the swarm movement concept to propose a new biologically-inspired control strategy for the tip trajectory tracking of flexible-joint manipulators. In this method, the positions of the joints and the robot end-effector are controlled simultaneously. Several approaches have been developed so far based on the swarm intelligence. Kennedy and Eberhart [14] introduced the particle swarm optimization (PSO) technique which is a computationally efficient method of finding the optimal solution for continuous nonlinear functions. This method is used in [15] for reactive and power control considering voltage stability. In other work, PSO is employed to optimize efficiently multiple machining parameters simultaneously for milling operation [16]. Other applications of the swarm control can be found in [17]. In this study, we develop a novel swarm control strategy applicable to the flexible-joint manipulators. The flexibility of the joints may arise from several phenomena such as elasticity in the transmission system, belts and bearings [5], and it may produce lightly damped oscillatory motions during the manoeuvre of the manipulator. Especially, the effect of joint flexibility becomes more significant in robot manipulators driven by harmonic drives. While harmonic drives have zero backlash, high torque transmissibility and compact size [18-

19], there is high torsional elasticity in harmonic drives which limit their capability [20]. Therefore, a more accurate control strategy in which the joint flexibility is taken into account is essential, especially in applications such as robots used in the manufacture of precision components (e.g. circuit boards). Another important effect which is taken into account in the design of the controller is joint friction. It has been proven that joint friction can lead to tracking errors and undesired stick-slip motion [21-29]. Despite this, joint friction is usually neglected in modeling and control strategies developed for flexible joint manipulators, e.g. [30] and [31]. In this study, to counterbalance the effect of the friction in the joints, a compensating torque is used along swarm control. The design of friction compensating torque is based on the non-linear dynamic LuGre model and its parameters are identified through closed-loop steady-state experiments.

To verify the performance of the proposed controller an experimental setup of a two rigid-link flexible-joint manipulator (TRLFJ) available at the Robotics Laboratory at the University of Saskatchewan is employed. Experiment results are presented for several trajectories and the performance of the swarm control is compared to the computed torque scheme which is usually utilized for control of the manipulator with stiff joints.

The structure of the paper is as follows. Section 2 of the paper details the characteristics of the experimental setup of the TRLFJ, and gives an overall picture of the proposed control scheme. The dynamics of the flexible-joint manipulators are given in Section 3, and Section 4 describes the application of the swarm control in the tip trajectory tracking of flexible-joint manipulators. Section 5 explains the design procedure of friction compensating torque, and Section 6 presents the experimental results obtained using the experimental setup of TRLFJ.

2. Experimental setup

The block diagram of the control strategy which was used in this study to control a two-rigid-link flexible-joint manipulator (TRLFJ) is shown in Fig. 1. The desired trajectory q_d and its derivatives, $\dot{q}_d$ and $\ddot{q}_d$, were the inputs to the controller. The positions of the motor, q_m, and link, q_L, were measured using encoders implemented in the experimental setup and the velocities were then obtained by taking the derivatives of the position signals using a low-pass filter. Employing the low-pass filter removed the high frequency noises which might deteriorate the controller performance. Also, since applying high-frequency signals to DC motors would eventually damage the motor brushes a band limit of 50 Hz was considered for the frequency of the signals applied to the motors. In our experimentation, the cutting frequency of the filter was set to 100 rad/s (16 Hz) which was much smaller than the band limit.

The applied torque τ had three parts; the inverse-dynamic torque τ_I, the friction compensating torque τ_f and the swarm torque τ_s; that is, $\tau = \tau_I + \tau_f + \tau_s$. The procedures to obtain these torques are described in Sections 4 and 5. To calculate the current required by the motor, the resultant torque τ was multiplied by the inverse of the torque constant of the motor, K_t, and the current was then fed into a D/A card. The motor torque constants for the experimental setup were $K_{t_s} = 8.92\ N.m/A$ and $K_{t_e} = 1.31\ N.m/A$[12] where the subscripts s and e stand for the shoulder and elbow, respectively.

The experimental setup which was used is shown in Fig. 2. The manipulator included two rigid links, which were driven using two DC motors. In order to increase the torques applied to the links, two harmonic drives were used, in the shoulder and elbow joints, with gear speed

---

[12] It is noteworthy that DC permanent magnet motors usually have a linear relationship to motor torque.

reduction ratios of 1:80 for the shoulder joint and 1:100 for the elbow joint, respectively. As shown in Fig. 2, the shoulder link was coupled to the shoulder joint by means of a flexible joint. At the end of the shoulder link a second harmonic drive was connected to the elbow link via the flexible elbow joint. Both motors and both flexible joints were instrumented with quadrature optical encoders whose resolutions were 0.0015 rad/count [32]. Other physical parameters of the manipulator are given in Table 1
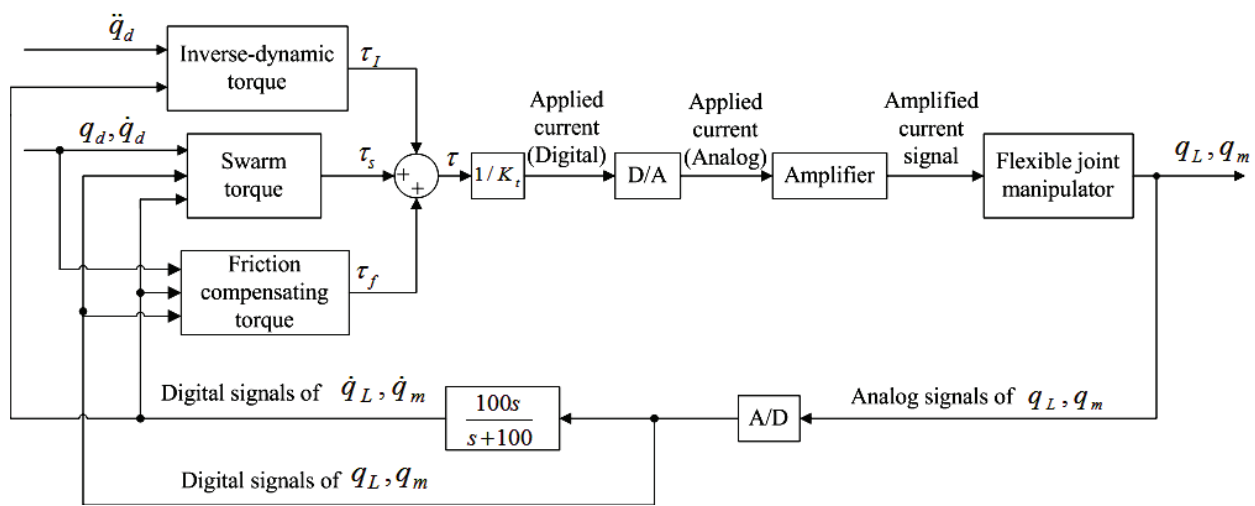
Fig. 1. Swarm control strategy for tip trajectory tracking of a two-rigid-link flexible-joint manipulator
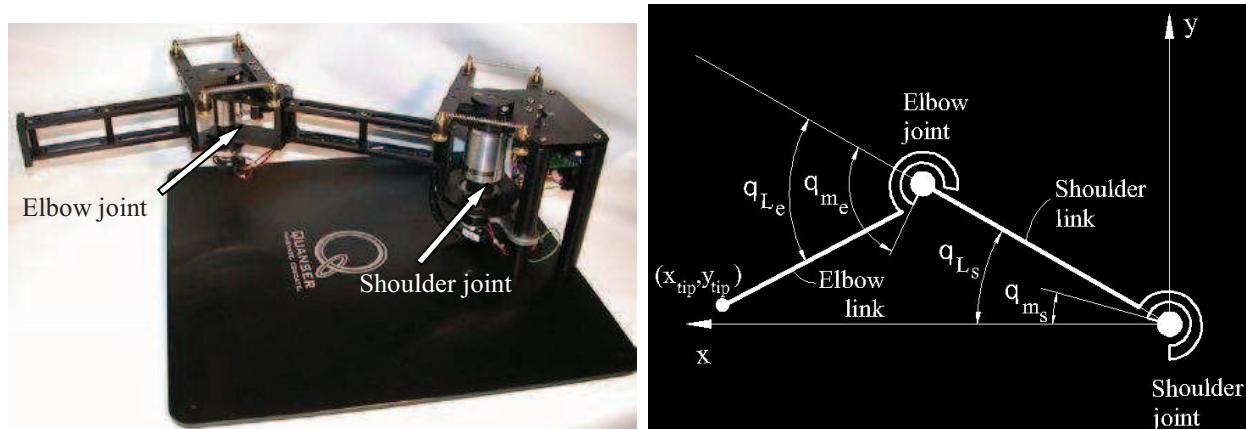
Fig. 2. (a) Experimental module of a two-rigid-link flexible-joint manipulator available in the Robotics Laboratory of the University of Saskatchewan, (b) schematic of the top-view of the experimental setup showing the angles of the joints and the links (subscripts *e* and *s* stand for elbow and shoulder, respectively)

Table 1. Physical parameters of the experimental setup of TRLFJ [32]

Parameter	Symbol	Shoulder	Elbow
Inertia of the downstream mechanism of the link[13]	D	$0.2300\ kg.m^2$	$0.0107\ kg.m^2$
Mass moment of inertia of the motor	J	$0.0110\ kg.m^2$	$0.0094\ kg.m^2$
Joint stiffness	K	$10.30\ N.m/rad$	$3.930\ N.m/rad$
Length of the link	l	$0.2230\ m$	$0.2230\ m$

3. Dynamics of flexible-joint manipulators

The dynamic equations of a serial manipulator consisting of n-rigid links connected by n-elastic joints (e.g. n=2 for the two-link manipulator shown in Fig. 2) are

$$M\ddot{q}_L + C_L\dot{q}_L + K(q_L - q_m) = H(\tau - \bar{\tau}_f), \qquad (1)$$

$$J\ddot{q}_m - K(q_L - q_m) = \tau - \bar{\tau}_f, \qquad (2)$$

where $M \in R^{n \times n}$ is the inertia matrix of the links and $C_L\dot{q}_L$ represents the vectors of Coriolis and centrifugal torques. The diagonal matrix $K = diag\ (k_1, k_2, \cdots, k_n)$ represents the stiffness of the joints. The matrix $J \in R^{n \times n}$ is the inertia matrix of the motors, τ is the vector of the applied torques to the motors, and $\bar{\tau}_f$ is the vector of the actual friction joint torques. Also, $q_L \in R^n$ and $q_m \in R^n$ represent, respectively, the rotations vectors of the links and the motors. The components of the matrix H are defined as $H_{ij} = -1$ when $i = j - 1$, and $H_{ij} = 0$ when $i \neq j - 1$ $i,j = 1,2, \cdots, n$.

---

[13] The inertia for the shoulder includes the mass moment of inertias of the shoulder and elbow links, and the elbow motor with respect to the shoulder joint. Also, the equivalent inertia for the elbow includes the mass moment of inertia of the elbow link with respect to the elbow joint.

In case all joints become rigid, the stiffness of the joints will approach infinity; that is $K \to \infty$, and the rotations of the links and the joints will be the same; that is $q_m = q_L$. Therefore, dynamic equations (1) and (2) are simplified as

$$(M + J)\ddot{q}_L + C_L\dot{q}_L = (H + I)(\tau - \bar{\tau}_f), \tag{3}$$

where I is the identity matrix. A proposed method for the tip trajectory tracking of the rigid manipulator is applying the following torque to the joints

$$\tau = \tau_I + \tau_{PID} + \tau_f, \tag{4}$$

in which the applied torque τ incorporates three parts. The first part is the inverse-dynamic torque τ_I which compensates for the effects of the inertial and centrifugal forces; that is

$$\tau_I = (M + J)\ddot{q}_d + C_L\dot{q}_L, \tag{5}$$

The second part is a PID controller which is

$$\tau_{PID} = (M + J)[D(\dot{q}_d - \dot{q}_L) + P(q_d - q_L) + I\int(q_d - q_L)dt], \tag{6}$$

where D, P and I are, respectively, the derivative, proportional and integrative gains of the PID controller, and the third part is a friction compensating torque τ_f which is designed to counterbalance the effect of the friction in the joints. Assuming that the friction compensating torque τ_f counterbalances the real friction of the joints $\bar{\tau}_f$; that is $\tau_f = \bar{\tau}_f$, the joints friction is eliminated from the dynamic equations of the manipulator, and combining (4)-(6) into (3) leads to the error equation

$$(M + J)(\ddot{e}_{lk} + D\dot{e}_{lk} + Pe_{lk} + +I\int e_{lk}dt) = 0, \tag{7}$$

where $e_{lk} = q_d - q_L$. Differentiation of (7) results in a 3$^{\text{rd}}$ order ordinary differential equation and since the inertia matrix cannot be zero

$$\dddot{e}_{lk} + D\ddot{e}_{lk} + P\dot{e}_{lk} + +Ie_{lk} = 0, \tag{8}$$

It can be shown provided that the gains of the PID controller are selected properly, the system in (8) will be asymptotically stable and the links error e_{lk} will exponentially approach zero.

The aforementioned method has been successfully used in [33] for tip trajectory tracking of manipulators in which the flexibility of the joints can be ignored. However, for tip trajectory tracking of manipulators in which the flexibility of the joints is crucial, the flexibility of the joints must be taken into account, and a more complicated controller is required. Similar to the rigid controller torque given in (4), our proposed controller torque for flexible-joint manipulators has three parts (see Fig. 1)

$$\tau = \tau_I + \tau_s + \tau_f, \tag{9}$$

where the first part of the applied torque τ is the inverse dynamic torque and it can be obtained from (5). The second part is a new biologically-inspired controller which is designed based on the swarm concept and is explained in the following section, and the third part is the friction compensating torque τ_f which is based on non-linear dynamic LuGre, and is explained in Section 5.

4. Swarm control

The main concept of the swarm control is based on the social behavioural pattern of organisms such as bird flocks and fish schools. When a flock of birds (or a school of fish) is moving towards a destination, each bird (or fish) has to follow a desired path so that the entire group moves towards the target. This is shown in Fig. 3. Each bird (or fish) is symbolically modelled by a particle, and the center of the swarm is shown at the center of the group. The swarm's center can be easily found as the average of the positions of the particles in the space; that is $X = \sum_{i=1}^{n} x_i/n$ and $Y = \sum_{i=1}^{n} y_i/n$ where (X, Y) denotes the Cartesian coordinate of the swarm's

center, (x_i, y_i) denotes each particle's location and n is the number of particles (e.g. $n = 8$ for the model of Fig. 3). The local error is defined as the error between the actual path of each particle and its desired path, and the global error shows the deviation of the group from its desired path. Each particle has a memory and intelligence and, hence, is able to correct its position such that the local and global errors are minimized during the motion of the swarm. Therefore, the swarm movement can be resembled by an optimization problem in which the objective function constitutes the local and the global errors. The optimum movement is achieved when the objective function is minimized.
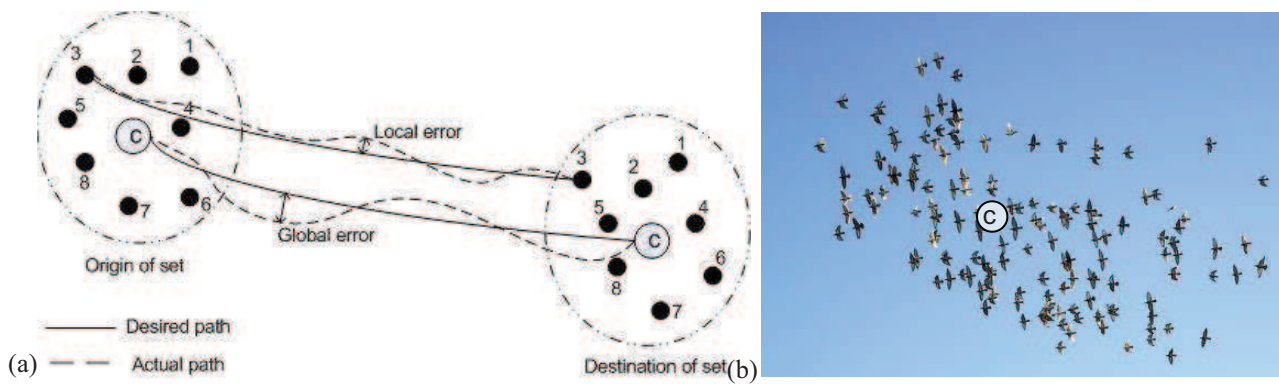
Fig. 3. (a) Schematic of a swarm movement; each particle is shown by a solid circle (b) An actual swarm of birds; the center of the swarm is denoted by c

To apply swarm control to the flexible-joint manipulators, each link is represented by a particle and the robot end-effector is represented by the swarm's center. For tip trajectory tracking, each link (particle) should move along its desired path so that the end-effector (swarm's center) can follow the desired trajectory of the swarm. Therefore, for flexible-joint manipulators, the local error is defined as the difference between the rotation of each link and its desired rotation

$$e_{lk} = q_d - q_L,$$ (10)

and the global error is the difference between the position of the end-effector and its desired position; that is

$$e_{tip} = \sqrt{(x_{tip} - x_{des})^2 + (y_{tip} - y_{des})^2}, \tag{11}$$

where x_{tip} and y_{tip} (shown in Fig. 2b) are the coordinates of the tip of the manipulator in the coordinate system shown in Fig. 2(b), and, x_{des} and y_{des} are the coordinates of the desired position of the manipulator's tip. The block-diagram of the swarm control scheme is shown in Fig. 3 which constitutes four principal parts:

1. *Variable-gain PID controller*: in this component, the applied torques to motors are evaluated using the following equation

$$\tau_s = Pe_{lk} + D\dot{e}_{lk} + I \int e_{lk} dt, \tag{12}$$

   where D, P and I are, respectively, the derivative, proportional and integrative gains of the PID controller. These gains are updated every time-step in the gain generator. The main reason to choose the PID controller to compute torque lies in its simplicity and clear physical meaning. Specially, in industrial applications, simple controllers are preferred to complex controllers, if the performance enhancement by employing complicated control methods are not significant enough [34].

2. *Gain generator*: this component produces proportional, derivative and integrative gains every time-step. These gains are then used in the PID controller, equation (12). Updating of the gains are based on the local and global errors and also their values at the previous time-step; that is

$$P(t + \Delta t) = P(t) + \alpha_P e_{lk} + \beta_P e_{tip}, \tag{13}$$

$$D(t + \Delta t) = D(t) + \alpha_D e_{lk} + \beta_D e_{tip}, \tag{14}$$

$$I(t + \Delta t) = I(t) + \alpha_I e_{lk} + \beta_I e_{tip}, \tag{15}$$

104

where α_P and β_P are updating coefficients for the proportional part of the controller in (13). Coefficients α_D and β_D are for the derivative part, equation (14), and coefficients α_I and β_I are used to update the integrative part in (15). Variable Δt is the time step that is used to update the gains. Updating gains make the swarm controller similar to an adaptive gain scheduling control scheme in which the parameters of the controller are modified depending on local and global errors, and the controller adjusts its parameters based on behaviour of the system.

To start computing the gains in (13)-(15), they must be initialized; that is, the initial values of P, D, and I must be specified at $t = 0$. The initial starting values can be determined from the 3rd order differential equation (8) such that all roots of the characteristic equation of (8) are negative, and, hence, the stability of the controller is guaranteed. Although equation (8) has been obtained with the assumption that the joints are rigid, however, it can be used as a good starting point to estimate the gains. The values of the gains are then adjusted based on the local and global errors using (13)-(15) during the manoeuvre of the manipulator.

3. *Memory:* After computing gains in the gain generator, they are stored in a memory. These values are then employed in the gain generator in the next time-step to evaluate proportional, derivative and integrative gains.

4. *Error evaluator*: in this component, local errors (links' errors) and global error (end-effector-error) are calculated based on the feedback signals of links rotations using equations (10) and (11).

Therefore, generally speaking the swarm control strategy is a self-organized robust technique in which the applied torques are regulated every time-step based on the local and

global errors observed in the links' rotations and the end-effector's position. The value of the swarm torque obtained in (12) is then added to the inverse dynamic torque   and the friction compensating torque   , and the resultant torque is applied to the motors (see Fig. 1).
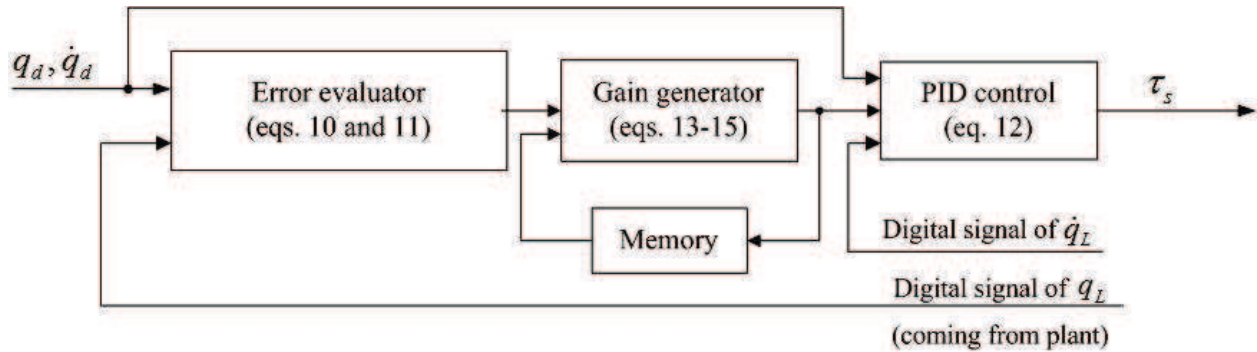
Fig. 4. Block diagram of the swarm torque controller for the tip-trajectory tracking of flexible-joint manipulators

5. Friction compensation

The design procedure of the friction compensating torque (FCT) is explained in this section. The main principles of the LuGre model and identification procedure of the friction properties of harmonic drives are explained in Sections 5.1. Details of the design of the friction compensating torque are given in Section 5.2.

5.1. Experimental estimation of the friction parameters

A friction model which describes different aspects of the friction torques in harmonic drives is the LuGre model [35]. In this model, the proposed friction torque for steady-state conditions has the mathematical form

$$, \qquad (16)$$

where   is the joint friction torque. Terms   and   are the Coulomb and stiction friction torques, respectively, and   and   are the Stribeck velocity and viscous damping coefficient,

respectively. The first two terms of the friction torque in (16) represent the Coulomb friction and Stribeck effect, respectively, and the last term accounts for the viscous damping. To determine the friction torque as a function of the velocity four parameters must be identified. These parameters are τ_{fc}, τ_{fs}, v_s and c_m which for each motor must be determined experimentally.

An experimental procedure which was designed and used to identify these parameters is discussed in detail in [4]. In total, 54 experiments were performed for the shoulder and elbow motors to estimate the friction torque as a function of velocity. The experimental data of the shoulder and elbow joint motors were then interpolated (curve-fitted) using the function of $\bar{\tau}_f$ given in (16). Using the experimentally identified parameters, the friction torques were expressed as functions of the velocity for the shoulder joint motor as

$$\bar{\tau}_{LuG} = \left[1.573 - 0.7919e^{-(\dot{q}_m/0.1900)^2}\right]\text{sgn}(\dot{q}_m) + 3.259\dot{q}_m, \quad \dot{q}_m > 0, \tag{17}$$

$$\bar{\tau}_{LuG} = \left[-1.988 + 0.8465e^{-(\dot{q}_m/0.1991)^2}\right]\text{sgn}(\dot{q}_m) + 2.933\dot{q}_m, \quad \dot{q}_m < 0, \tag{18}$$

and for the elbow joint motor as

$$\bar{\tau}_{LuG} = \left[0.6761 - 0.2992e^{-(\dot{q}_m/0.6050)^2}\right]\text{sgn}(\dot{q}_m) + 0.2532\dot{q}_m, \quad \dot{q}_m > 0, \tag{19}$$

$$\bar{\tau}_{LuG} = \left[-0.6826 + 0.2802e^{-(\dot{q}_m/0.4824)^2}\right]\text{sgn}(\dot{q}_m) + 0.3007\dot{q}_m, \quad \dot{q}_m < 0, \tag{20}$$

The experimental data and the estimated functions given in (17)-(20) for the shoulder and the elbow joint motors are shown in Fig. 5. As can be seen in this figure, for the shoulder joint, the overall friction torque varied from -4 to 4 N.m., when the range of the velocity was -0.7 to 0.7 (rad/s). For the elbow joint, the change was much smaller from -0.7 N.m. to 0.7 N.m. for the same range of velocity. Also, according to the functions of the friction torques, the Stribeck velocity in the elbow joint motor was greater than in the shoulder joint motor. However, the shoulder joint had larger viscous damping and stiction than the elbow joint.
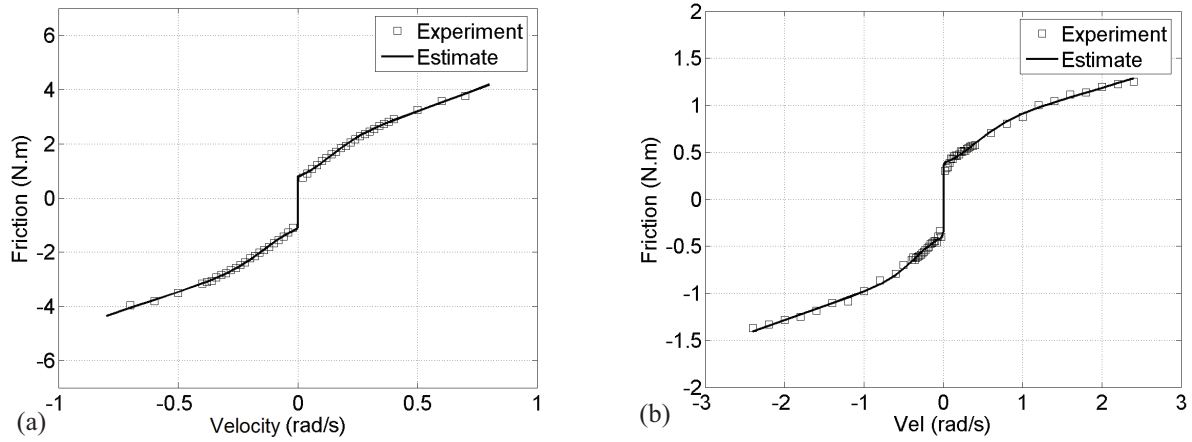
Fig. 5. Experimental results obtained for steady state conditions and estimation function obtained based on the LuGre model for a TRLFJ (a) shoulder joint motor, (b) elbow joint motor

5.2. Friction compensation strategy

Ideally, the counterbalancing estimated joint friction torque found in (17)-(20), is equal to the real friction of the joints, and, hence, the friction of the joints will be compensated completely. However, practically there is always an error between the estimated joint friction torque and the actual friction torque. Some of these error sources were as follows:

1. The friction torques were obtained based on the assumption of steady-state conditions, and the pre-sliding regime in which stick-slip motion occurs at very low velocities was not considered.

2. Although the friction can change with oil temperature, load, humidity and actuator wear [36], the effects of these parameters were not taken into account in the friction model presented for the shoulder and elbow joints.

To remove the aforementioned errors a PD controller along with friction torque based on (17)-(20) was used. Therefore, the friction compensating torque was

$$\tau_f = \bar{\tau}_{LuG} + P_f(q_d - q_m) + D_f(\dot{q}_d - \dot{q}_m), \tag{21}$$

in which the first term was identified based on (17)-(20), and constants P_f and D_f were proportional and derivative gains of the friction compensating torque. The stability analysis using the Lyapunov theory of this friction compensating strategy has been discussed in [37]. According to this analysis, the controller was stable provided that the appropriate parameters P_f and D_f were selected. Also, it has been shown in [37] while employing the proposed method in (21) could avoid hunting[14], it led to a steady-state error in friction compensation. The range of this error was a function of friction parameters, values of parameters P_f and D_f, and inertias of motors.

6. Experimental results

To verify the performance of the new controller described in the previous sections, the two-rigid-link flexible-joint (TRLFJ) manipulator, shown in Fig. 2, was used. The physical parameters of the experimental setup are given in Table 1 in Section 2. The desired trajectory for rotations of links was considered to be the ninth-order polynomial

$$q_d = [90\left(\frac{t}{t_f}\right)^9 - 315\left(\frac{t}{t_f}\right)^8 + 540\left(\frac{t}{t_f}\right)^7 - 420\left(\frac{t}{t_f}\right)^6 + 126\left(\frac{t}{t_f}\right)^5]q_f, \qquad (22)$$

where q_d, q_f and t_f were, respectively, the desired trajectory of the rotation of both shoulder and elbow links, the final rotation of the link and the time of total manoeuvre. This trajectory was designed such that it satisfied the initial conditions of $q_d(0) = 0$, $q_d(t_f) = q_f$ and $d^i q_d/dt^i|_{t=0,t_f}$ $i = 1,2,3,4$. Thus, since the trajectory had to satisfy ten initial conditions, it was

---

[14] Stick-slip oscillations around target position caused by the difference between Coulomb friction and Stiction is referred to as hunting [38].

chosen as a polynomial of ninth order. Experiments were also carried out for other lower-order

desired trajectories, however, for briefness they are not included in this paper.

6.1. Trajectory tracking

Several desired trajectories were tested to ensure that the controller was able to perform

effectively at different trajectories and velocities. According to the technical manual of the

experimental setup, the maximum rotations both links could reach was $3\ rad$. Therefore, the

experiments were performed for final rotations less than $3\ rad$ with steps of $0.5\ rad$; that is,

final rotations q_f were chosen as $0.5, 1, 1.5, 2$ and $2.5\ rad$ in different experiments. The shape

of the trajectory was the ninth-order polynomial given in (22), and the manoeuvre time was

$t_f = 4\ sec$. The initial values of the gains chosen were $[P_s, D_s, I_s] = [300, 40, 1]$ for the shoulder

and $[P_e, D_e, I_e] = [60, 5, 1]$ for the elbow. As discussed in Section 4, the initial values of the

gains were selected such that the stability of system given in (8) for rigid manipulator was

guaranteed. While these initial values were found based on the assumption of the rigid-joints,

yet, they were good starting points for our controller. This was proven through a sensitivity

analysis that was performed to investigate the effect of initial values of the gains on the

performance of the controller. Details of this analysis are given in Section 6.4.

The updating coefficients α and β used in the gain generator, equations (13)-(15), to

update the gains of the swarm control were $\left[\alpha_{P_s}, \alpha_{D_s}, \alpha_{I_s}\right] = [30, 8, 1]$ and $\left[\beta_{P_s}, \beta_{D_s}, \beta_{I_s}\right] =$

$[12, 5, 0.5]$ for the shoulder. For the elbow link these parameters were selected as

$\left[\alpha_{P_e}, \alpha_{D_e}, \alpha_{I_e}\right] = [60, 5, 1]$ and $\left[\beta_{P_e}, \beta_{D_e}, \beta_{I_e}\right] = [5, 0.5, 0.1]$. Experiments were performed for

several trajectories with different final rotations, however, for briefness, only the trajectory

tracking results for the final rotations $0.5\ rad$, $1.5\ rad$ and $2.5\ rad$ are shown in Figs. (6)-(8).

As shown in these figures, the links followed the desired trajectory precisely such that the

tracking error between the actual and desired trajectories was almost zero for different final rotations of the manipulator. This indicated that the swarm controller was able to perform successfully at different trajectories.
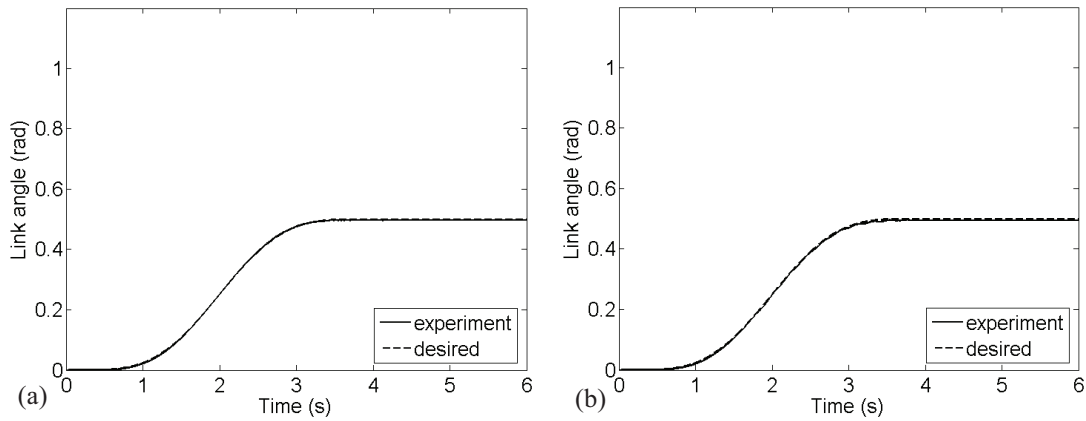
Fig. 6. Experimental results of swarm control for two-rigid-link flexible-joint manipulator: Links rotations for ninth-order trajectory with final rotation $q_f = 0.5\ rad$; (a) shoulder link angle, (b) elbow link angle
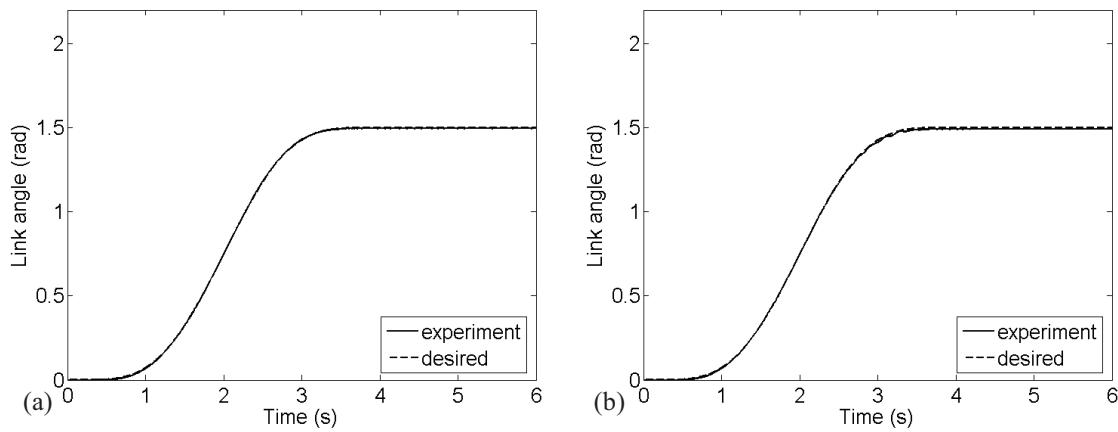
Fig. 7. Experimental results of swarm control for two-rigid-link flexible-joint manipulator: Links rotations for ninth-order trajectory with final rotation $q_f = 1.5\ rad$; (a) shoulder link angle, (b) elbow link angle
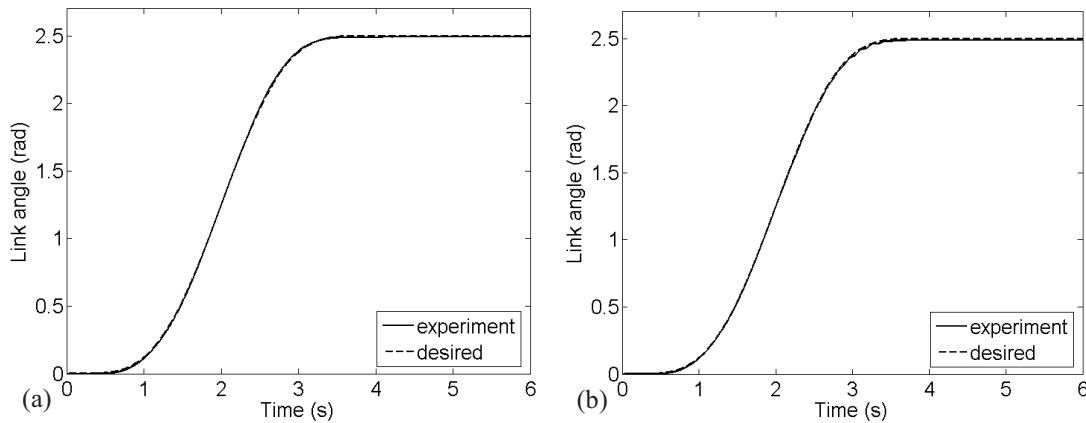
Fig. 8. Experimental results of swarm control for two-rigid-link flexible-joint manipulator: Links rotations for ninth-order trajectory with final rotation $q_f = 2.5\ rad$; (a) shoulder link angle, (b) elbow link angle

To have a better understanding of the experimental data, several error measures were considered: normalized tracking error percentage, steady-state error, maximum normalized error and the tip error. The percentage of normalized tracking error was defined as

$$error = \left(\frac{q_L - q_d}{q_f}\right) \times 100, \tag{23}$$

where q_d, q_f and q_L were, respectively, the desired trajectory of the rotation, the final rotation of the link and the position of the link. The normalized tracking error showed the difference between the experimental and desired values of the links rotation during the manoeuvre of the manipulator. The maximum normalized error was

$$error_{max} = \max\left(\left|\frac{q_L - q_d}{q_f}\right|\right) \times 100, \tag{24}$$

and the tip-trajectory-tracking error was obtained based on the distance difference between the actual and the desired positions of the manipulator's tip. The tip position was measured during the maneuver of the manipulator using the rotations of the links as follows

$$x_{tip} = L_s \cos\left(q_{L_s}\right) + L_e \cos\left(q_{L_s} + q_{L_e}\right),$$

$$y_{tip} = L_s \sin\left(q_{L_s}\right) + L_e \sin\left(q_{L_s} + q_{L_e}\right), \tag{25}$$

where x_{tip} and y_{tip} were respectively the coordinates of the tip of the manipulator in the coordinate system shown in Fig. 2(b). Parameter L was the length of each link, and q_L was the rotation of the links. Also, as mentioned before subscripts s and e denoted the shoulder and elbow respectively. Once the actual position of the tip was found from (25), the tip-trajectory-tracking error was computed using (11). Steady-state error was measured as the difference between the actual and desired trajectories when the response of the system became stable, and the normalized steady state error was equal to the steady state error divided by the final rotation q_f. A summary of the error values are tabulated in Table 2 for different desired trajectories.

113

According to these values, for all cases the normalized maximum tracking error was less than 1.4% while the steady-state error was less than 1.0%. The end-effector error was at most $3.6\ mm$ when the final rotations of the links were $q_f = 2.5\ rad\ (143^{\circ})$. This error was $2.0\ mm$ for $q_f = 1.5\ rad\ (86^{\circ})$, and $0.34\ mm$ when $q_f = 0.5\ rad\ (29^{\circ})$. Therefore, based on these values, one may conclude that the controller acted very successfully in trajectory tracking task.

The time variation of the controller gains for the shoulder link is shown in Fig. 9, when the final rotation of the manipulator was $q_f = 1.5\ rad$. It can be observed that the gains were kept constant after a manoeuvre time of $t_f = 4\ sec$. The reason for doing this was that because of the steady-state (constant) error at the end of the manoeuvre, the gains of the controller were linearly increased in equations (13)-(15). Therefore, according to (12) the applied swarm torque was increasing constantly and after a while the system became unstable. To avoid this, a switch was utilized in the controller so that the gains were kept constant as the manipulator reached its final position, and hence, the controller tuned into a typical PID controller with constant gains at the end of the manoeuvre $(t > t_f)$.

Table 2. Experimental results of the swarm control for two-rigid-link flexible-joint manipulator: comparison of error values for different final rotations q_f

	$q_f = 0.5\ rad$		$q_f = 1.5\ rad$		$q_f = 2.5\ rad$	
	Shoulder	Elbow	Shoulder	Elbow	Shoulder	Elbow
Max. error (rad)	0.0034	0.0070	0.0058	0.015	0.015	0.019
Steady-state error (rad)	0.0031	0.0046	0.0044	0.0077	0.0092	0.0097
Normalized max. error (%)	0.68	1.4	0.39	1.02	0.60	0.77
Normalized Steady-state error (%)	0.63	0.91	0.29	0.51	0.37	0.39
Max. end-effector error (m)	0.00034		0.0020		0.0036	
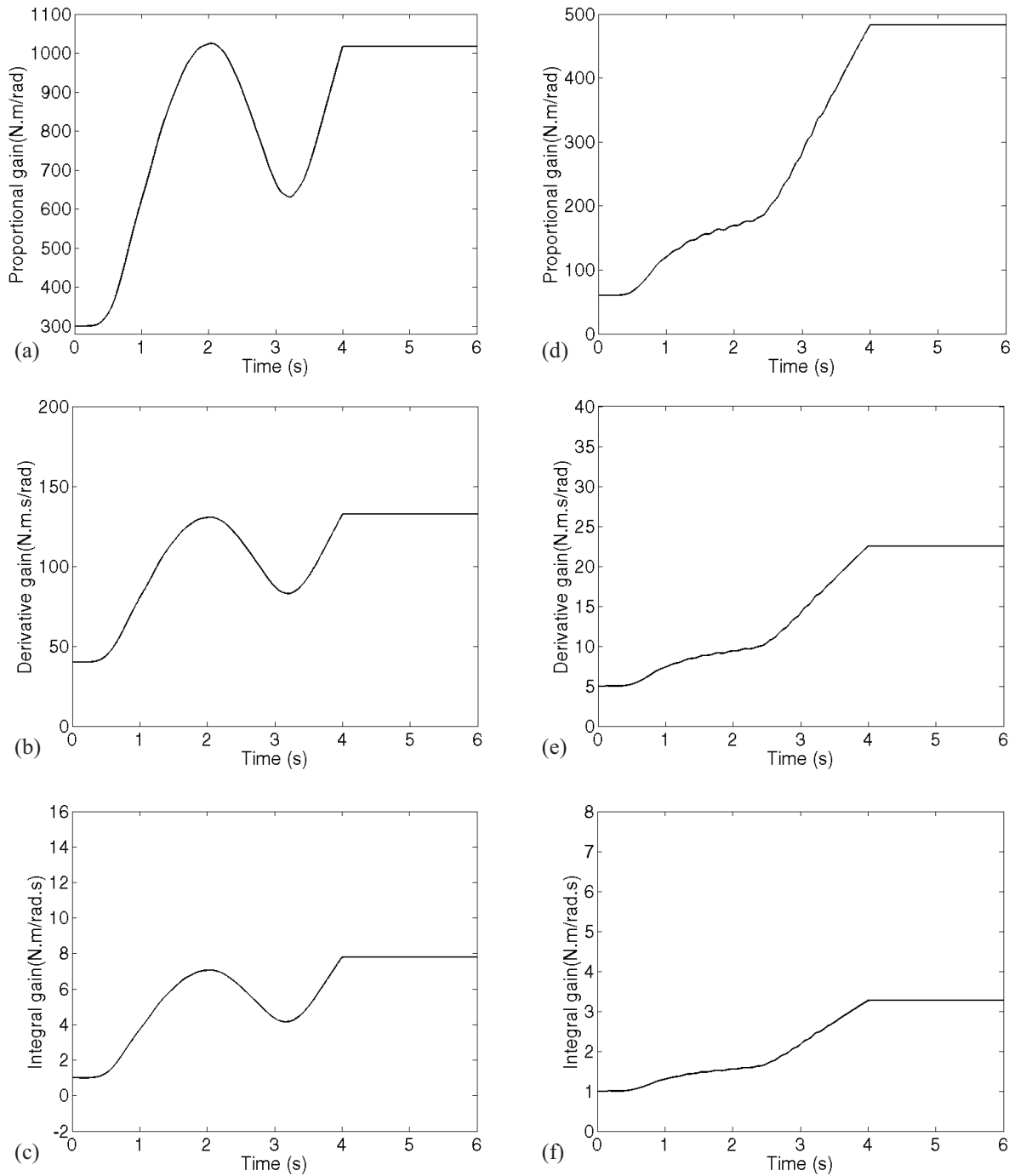
Fig. 9. Experimental results of swarm control for two-rigid-link flexible-joint manipulator: variation of the gains for the shoulder link; (a) proportional gains, (b) derivative gain, (c) integral gain, variation of the gains for the elbow link; (d) proportional gains, (e) derivative gain, (f) integral gain.

6.2. Rigid controller versus swarm controller

In this section, the performance of the swarm controller is experimentally compared to the rigid controller. The rigid controller torque, given in (4), was obtained using the inverse-dynamic approach which was a typical control method for robots with the rigid joints (i.e. $K \rightarrow \infty$). In these experiments the desired trajectory of the links was the ninth-order trajectory given in (22). Final rotations of both links were $q_f = 1.0\ rad$, and the manoeuvre time was $t_f = 4\ sec$. The normalized tracking error percentage, given in equation (23), is compared for the rigid and swarm controls in Fig. 10. It can be observed that the tracking error was significantly reduced, for both shoulder and elbow links, by using the swarm controller compared to the results obtained using the rigid controller. For instance, according to the values of the maximum tracking errors in Table 3, the performance of the swarm controller was five times ($3.5/0.65 \approx$ 5) better than the rigid controller for the shoulder, and about three times ($2.0/0.63 \approx 3$) better for the elbow link. The steady-state errors were also decreased by applying the swarm control; especially for the elbow, this error was reduced from 1.1 % for the rigid controller to 0.48 % for the swarm controller. Furtheremore, as shown in Fig. 11 the end-effector error was considerably decreased by employing the swarm control as the maximum error was reduced from 17 mm for the rigid controller to 3.6 mm for the swarm controller.
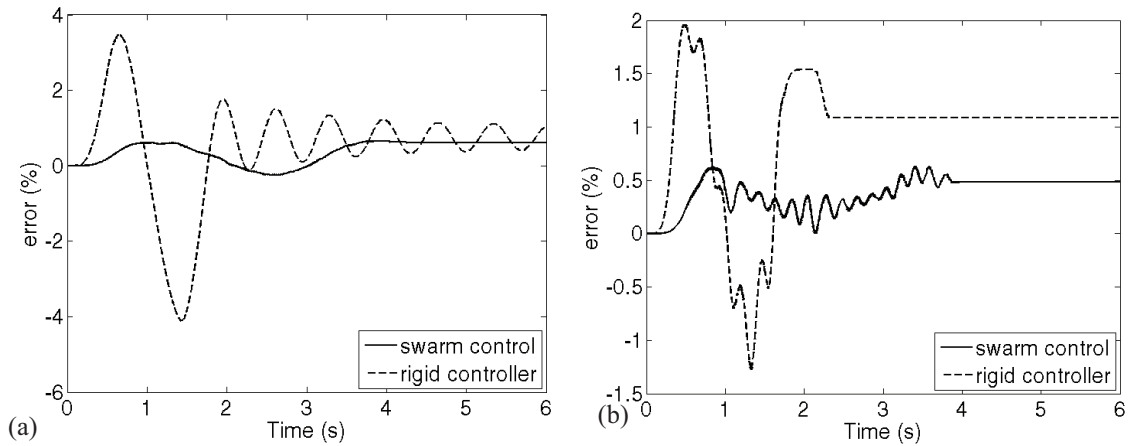
Fig. 10. Experimental results: normalized tracking error for swarm and rigid controllers (a) shoulder link, (b) elbow link
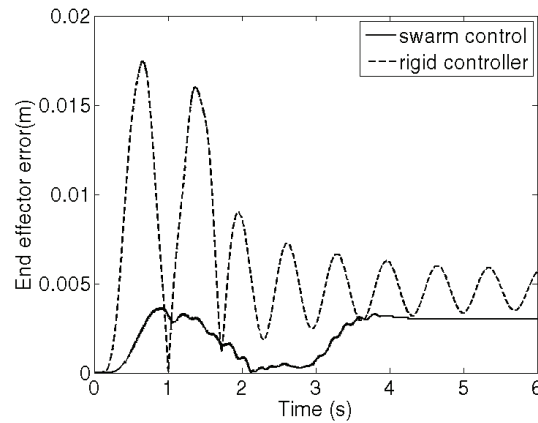
Fig. 11. Experimental results: comparison of the end-effector error for swarm and rigid controllers

Table 3. Summary of experimental results for swarm and rigid controllers

	Rigid controller		Swarm control	
	Shoulder	Elbow	Shoulder	Elbow
Max. error (rad)	0.035	0.020	0.0065	0.0063
Steady-state error (rad)	0.0067	0.011	0.0060	0.0048
Normalized max. error (%)	3.5	2.0	0.65	0.63
Normalized Steady-state error (%)	0.67	1.1	0.60	0.48
Max. end-effector error (m)	0.017		0.0036	

6.3. Effect of the speed of the manipulator

In this section the performance of the controller is experimentally analyzed for different manipulation speeds. The desired trajectory of the links was the ninth-order polynomial given in (22) with the final rotation of $q_f = 1.5\ rad$. In the experiments presented in Section 6.1 for $q_f = 1.5\ rad$ (see Fig. 7), the maneuver time was $t_f = 4\ sec.$, the maximum speed of the links reached $0.92\ rad/s$, and the maximum speed of the end-effector was $0.28\ m/s$. To test the controller at a higher speed, the maneuver time of the manipulator was decreased to $3\ sec.$ while the final rotation of the manipulator was kept constant as before; that is $q_f = 1.5\ rad$. In this experiment, the maximum speed of the links was recorded $1.23\ rad/s$, and the maximum speed of the end-effector was $0.45\ m/s$. The corresponding experimental results are shown in Fig. 12 for the shoulder and elbow links. As shown in this figure and as indicated in Table 4, the tracking error was very small for both links and the maximum error at the end-effector was approximately $1.5\ mm$. The experiments were then repeated for more rapid motion of the manipulator as the maneuver time was decreased to $2.5\ sec.$ for the final rotation of $q_f = 1.5\ rad$. For this case, the maximum speed of each link reached $1.46\ rad/s$ $(84\ deg/s)$, and the maximum speed of the end-effector was about $0.55\ m/s$ which was relatively high[15]. The experimental results are shown in Fig. 13 where the tracking error between the rotations of the links and the desired trajectories was remained very small. As indicated in Table 4, for this case the maximum error at the end-effector position reached $1.5\ mm$. Therefore, according to the results presented in this section, the controller was able to work successfully in tracking task at different speeds while

---

[15] Note that for typical similar size robot manipulators the maximum end-effector speed is $0.25\ m/s$ [27]

both tracking error for the links and the end effector remained very small during the maneuver of the manipulator.
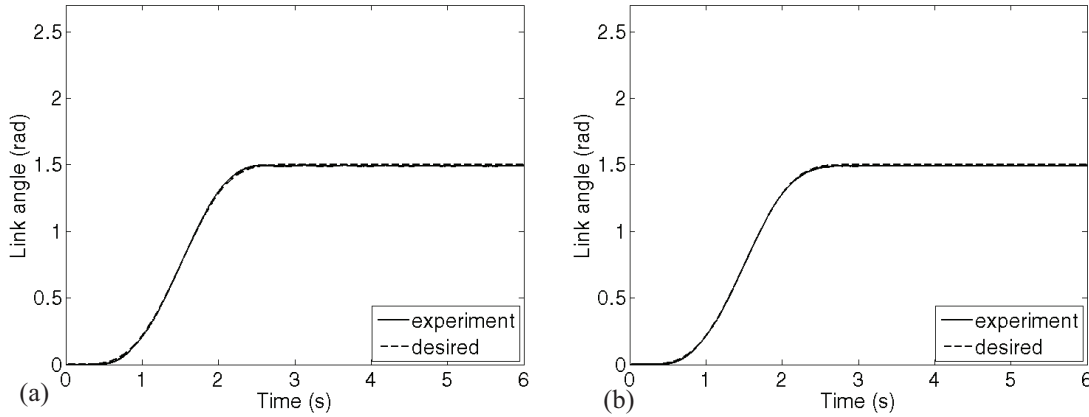
Fig. 12. Experimental results of swarm control for the two-rigid-link flexible-joint manipulator: (a) shoulder link angle, (b) elbow link angle. ($q_f = 1.5\ rad, t_f = 3\ sec, \dot{q}_L^{max} = 1.23\ rad/s$)
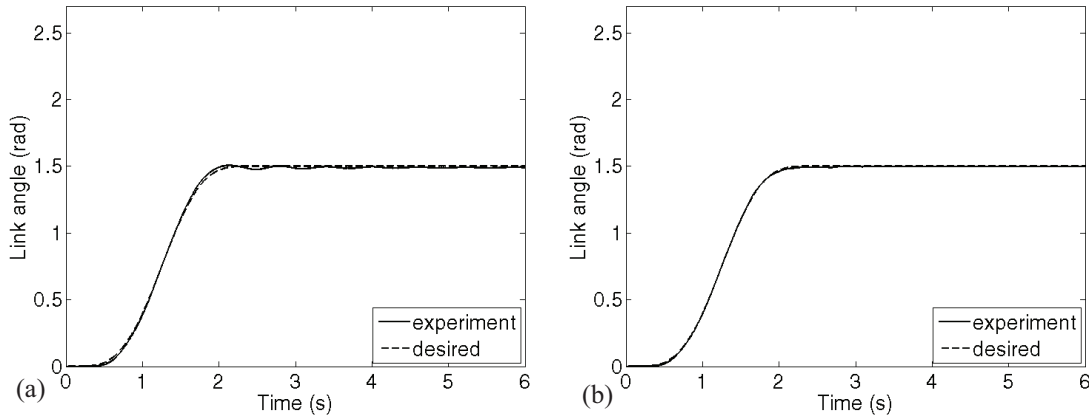
Fig. 13. Experimental results of swarm control for the two-rigid-link flexible-joint manipulator: (a) shoulder link angle, (b) elbow link angle. ($q_f = 1.5\ rad, t_f = 2.5\ sec, \dot{q}_L^{max} = 1.48\ rad/s$)

Table 4. Experimental results of swarm control for the two-rigid-link flexible-joint manipulator: comparison of error values for different manipulation speeds for $q_f = 1.5\ rad$

	Max speed 0.92 ($t_f = 4\ sec.$, Fig. 7)		Max speed 1.23 rad/s ($t_f = 3\ sec.$, Fig. 12)		Max speed 1.46 rad/s ($t_f = 2.5\ sec.$, Fig. 13)	
	Shoulder	Elbow	Shoulder	Elbow	Shoulder	Elbow
Max. error (rad)	0.0058	0.015	0.015	0.011	0.024	0.011
Steady-state error (rad)	0.0044	0.0077	0.0072	0.0077	0.011	0.0060
Normalized max. error (%)	0.39	1.02	0.99	0.77	1.6	0.75
Normalized Steady-state error (%)	0.29	0.51	0.48	0.51	0.77	0.40
Max. end-effector error (m)	0.0020		0.0015		0.0015	

6.4. Sensitivity analysis

In this section, the influence of the initial values of the gains on the behaviour of the time-variable-gain controller is investigated. Ideally, the controller should be completely robust and insensitive to the initial values. This means that for an ideal controller the response of the system did not change by assigning different initial gains. However, in practice, it is acceptable if the controller can work successfully for a limited range of the initial gains. In the experimental results presented in the previous sections the initial values of the gains were selected as $[P_s, D_s, I_s] = [300, 40, 1]$ for the shoulder and $[P_e, D_e, I_e] = [60, 5, 1]$ for the elbow. These initial values were selected such that the system given in (8) for a rigid manipulator was stable. For sensitivity analysis, the initial values of the gains were increased by 20%. Therefore, new initial values were $[P_s, D_s, I_s] = [360, 48, 1.2]$ for the shoulder and $[P_e, D_e, I_e] = [72, 6, 1.2]$ for the elbow. The variable gains are shown in Fig. 15. Similar to Fig. 7, the tracking errors were still small and the links followed the desired trajectories accurately in this experiment.

The initial values of gains were decreased by 20% with respect to the original values; that is, the new initial values were $[P_s, D_s, I_s] = [240, 32, 0.8]$ for the shoulder and $[P_e, D_e, I_e] = [48, 4, 0.8]$ for the elbow. The corresponding experimental results for the variable gains are shown in Fig. 16. According to Table 5, the tracking errors still remained very small, and it can be observed even if the initial values of the gains were changed by $\pm 20\%$, the errors did not change considerably. In particular, the end-effector error was very small for all cases. This error was between 1.8 mm to 2.3 mm as shown in Table 5. Therefore, according to the experimental results one can conclude that the controller was robust to the initial conditions and the performance of the controller was almost insensitive to the changes in initial conditions of the controller parameters. It is noteworthy to mention that while the experimental results presented

here indicated the robustness of the controller for $\pm 20\%$ of the initial gains, however, the controller was stable for a wider range of initial gains. For example, it was experimentally proven that the controller was stable for initial gains from $[P_s, D_s, I_s] = [50, 10, 0.1]$ to $[P_s, D_s, I_s] = [929, 122, 8.22]$ for the shoulder, and $[P_e, D_e, I_e] = [10, 2, 0.1]$ to and $[P_e, D_e, I_e] = [294, 14.2, 2.11]$ for the elbow.
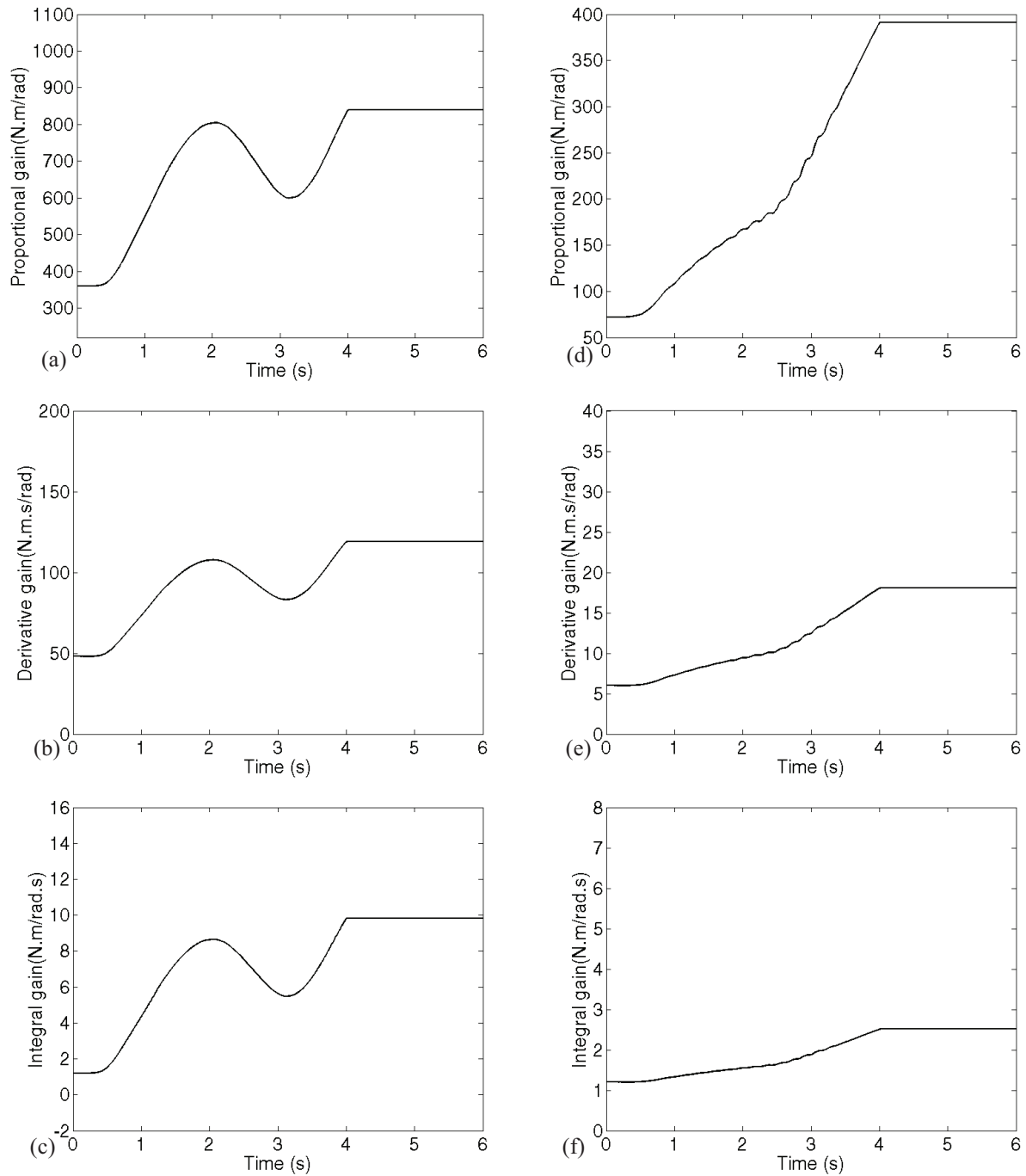
Fig. 14. Experimental results of swarm control for the two-rigid-link flexible-joint manipulator: variation of the gains for the shoulder link; (a) proportional gains, (b) derivative gain, (c) integral gain; variation of the gains for the elbow link; (d) proportional gains, (e) derivative gain, (f) integral gain. ($q_f = 1.5\ rad, t_f = 4\ sec.$, initial gains for the shoulder $[P_s, D_s, I_s] = [360, 48, 1.2]$ and the elbow $[P_e, D_e, I_e] = [72, 6, 1.2]$)
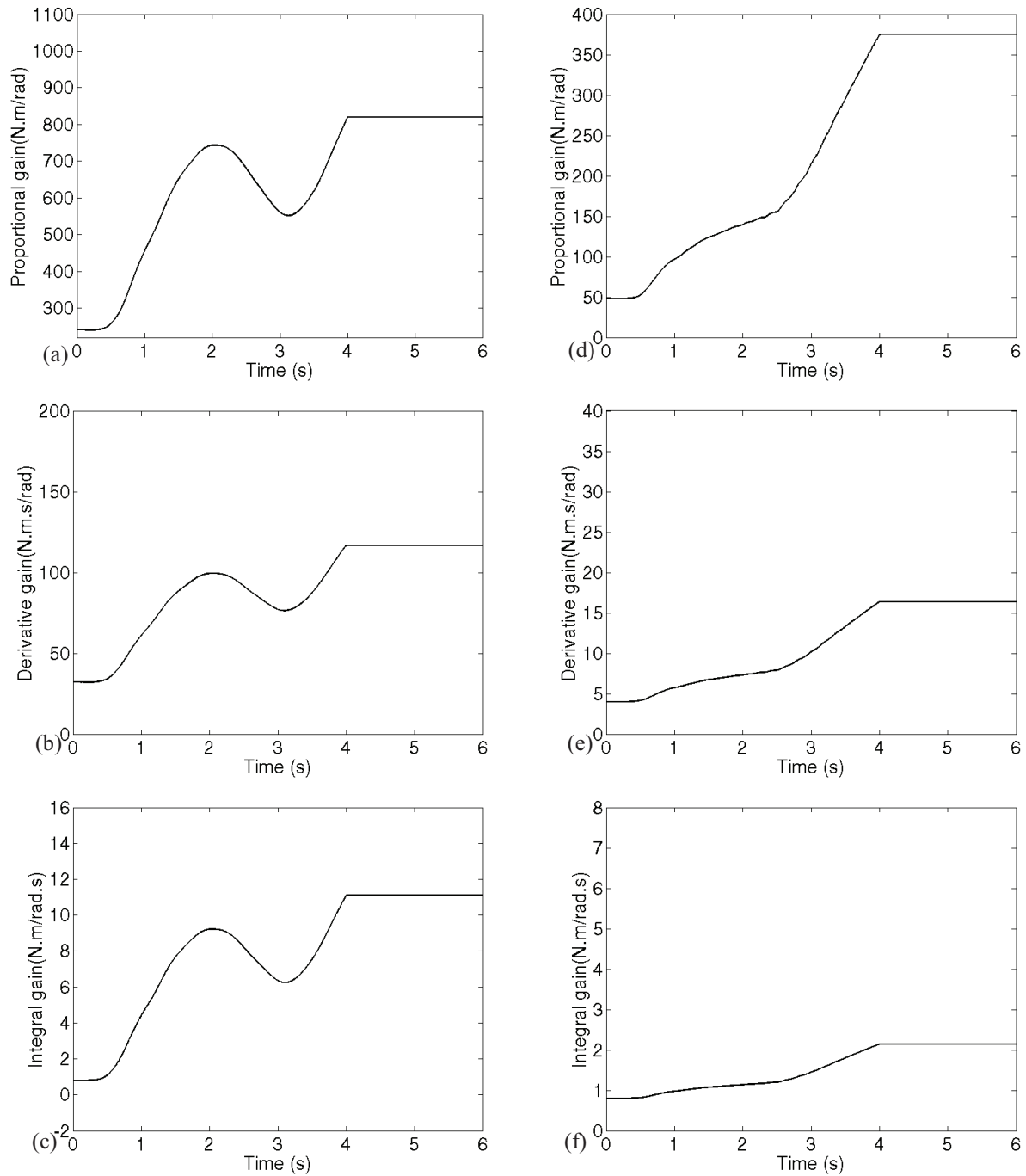
Fig. 15. Experimental results of swarm control for the two-rigid-link flexible-joint manipulator: variation of the gains for the shoulder link; (a) proportional gains, (b) derivative gain, (c) integral gain; variation of the gains for the elbow link; (d) proportional gains, (e) derivative gain, (f) integral gain. ($q_f = 1.5\,rad, t_f = 4\,sec.$, initial gains for the shoulder $[P_s\,D_s\,I_s] = [240, 32, 0.8]$, and the elbow $[P_e\,D_e\,I_e] = [48, 4, 0.8]$)

Table 5. Experimental results of swarm controller for the two-rigid-link flexible-joint manipulator: comparison of error values for different initial values of the gains ($q_f = 1.5\ rad, t_f = 2.5\ sec.$, original initial gains $[P_s, D_s, I_s] = [300, 40, 1], [P_e, D_e,\ I_e] = [60, 5, 1]$)

	Original initial gains		20% increase of initial gains		20% decrease of initial gains	
	Shoulder	Elbow	Shoulder	Elbow	Shoulder	Elbow
Max. error (rad)	0.0058	0.015	0.0068	0.017	0.0084	0.013
Steady-state error (rad)	0.0044	0.0077	0.0055	0.0082	0.0060	0.0096
Normalized max. error (%)	0.39	1.02	0.45	1.2	0.56	0.90
Normalized Steady-state error (%)	0.29	0.51	0.37	0.55	0.40	0.64
Max. end-efftor error (m)	0.0020		0.0023		0.0018	

7. Conclusions

In this paper, a novel biologically-inspired swarm controller was proposed for the tip trajectory tracking of flexible-joint manipulators. The main concept of the controller was inspired by the social behaviour pattern of swarms in which every particle corrected its position toward its best location so that the entire swarm found its best position. This idea was adopted for the control of a set of flexible-joint manipulators. The local error was defined as the difference between the rotations of links and their desired positions, and the global error was defined as the difference between the end-effector position and its desired one. The main objective of the swarm control was to minimize the local and global errors simultaneously. For this purpose, the parameters of the controller were updated every time step based on their previous values, restored from the memory embedded in the controller, and the local and global errors. To verify the proposed approach, the experimental setup of two-rigid-link flexible-joint manipulator was employed. The experimental results indicated that the controller was successful in the tip trajectory task for different final rotations and different manipulation speeds. An experimental comparison between swarm control and a typical controller used for rigid robots, inverse dynamic torque control,

demonstrated the superiority of the proposed swarm control strategy. Furthermore, to analyze the effects of initial gains of the time-variable-gain controller, a sensitivity analysis was experimentally performed and it was shown that the tracking and the steady-state errors did not change significantly for different initial gains of the controller.

8. References

1. M. W. Spong, Modeling and control of elastic joint robots, *Journal of Dynamic Systems, Measurement and Control*, *109*(4), 1987, 310-319.
2. A. Konno, & L. Deman, A singularly perturbed method for pole assignment control of a flexible manipulator, *Robotica*, *20*(6), 2002, 637-651.
3. Y. R. Hu, & G. Vukovich, Position and force control of flexible joint robots during constrained motion tasks, *Mechanism and Machine Theory*, *36*(7), 2001, 853-871.
4. H. Salmasi, R. Fotouhi, & P. N. Nikiforuk, Tip trajectory tracking of flexible-joint manipulators driven by harmonic drives, *International Journal of Robotics and Automation*, *24*(2), 2009.
5. A. Benallegue, Adaptive control for flexible joint robots using a passive systems approach, *Control Engineering Practice*, *3*(10), 1995, 1393-1400.
6. F. Ghorbel, J. Y. Hung, & M. W. Spong, Adaptive control of flexible-joint manipulators, *IEEE Control Systems Magazine*, *9*(7), 1989, 9-13.
7. S. S. Ge, Adaptive controller design for flexible joint manipulators, *Automatica*, *32*(2), 1996, 273-278.
8. J. H. Oh, & J. S. Lee, Control of flexible joint robot system by backstepping design approach, *Proceedings of IEEE International Conference on Robotics and Automation*, Albuquerque, NM, 1997, 3435-3440.
9. D. Wang, A simple iterative learning controller for manipulators with flexible joints, *Automatica*, *31*(9), 1995, 1341-1344.
10. S. Jain, & F. Khorrami, Robust adaptive control of flexible joint manipulators, *Automatica*, *34*(5), 1998, 609-615.

11. C. J. B. Macnab, & G. M. T. D'Eleuterio, Neuroadaptive control of elastic-joint robots using robust performance enhancement, *Robotica*, *19*(6), 2001, 619-629.

12. D. S. Morgan, & I. B. Schwartz, Dynamic coordinated control laws in multiple agent models, *Physics Letters A*, *340*, 2005, 121-131.

13. A. Ratnaweera, S. K. Halgamuge, & H. C. Watson, Self-organizing hierarchical particle swarm optimizer with time-varying acceleration coefficients, *IEEE Transactions on Evolutionary Computation*, *8*(3), 2004, 240-255.

14. J. Kennedy, & R. Eberhart, Particle swarm optimization, *Conference Proceedings of IEEE International Conference on Neural Networks,* Perth, Western Australia, *4*, 1995, 1942-1948.

15. H. Yoshida, Y. Fukuyama, S. Takayama, & Y. Nakanishi, A particle swarm optimization for reactive power and voltage control in electric power systems considering voltage security assessment, *Conference Proceedings of IEEE International Conference on Systems, Man, and Cybernetics*, Rio de Janeiro, Brazil, *6*, 1995, 497-502.

16. V. Tandon, H. El-Mounayri, & H. Kishawy, NC end milling optimization using evolutionary computation, *International Journal of Machine Tools and Manufacture*, *42*(5), 2002, 595-605.

17. R. C. Eberhart, & Y. Shi, Particle swarm optimization: developments, applications and resources, *Proceedings of the IEEE Congress on Evolutionary Computation (CEC 2001)*, Seoul, Korea, *1*, 2001, 81-86.

18. A. Albu-Schaffer, C. Ott, & G. Hirzinger, A unified passivity-based control framework for position, torque and impedance control of flexible joint robots, *International Journal of Robotics Research*, *26*(1), 2007, 23-39.

19. M. Spong, K. Khorasani , & P. Kokotovic, An integral manifold approach to the feedback control of flexible joint robots, *IEEE Journal of Robotics and Automation, 3*(4), 1987, 291-300.

20. L. Sweet, & M. Good, Redefinition of the robot motion-control problem, *IEEE Control Systems Magazine*, *5*(3), 1985, 18-25.

21. H. Abdellatif, & B. Heimann, On compensation of passive joint friction in robotic manipulators: modeling, detection and identification, *IEEE International Conference on Control Applications*, Munich, 2006, 2510-2515.

22. A. Lotfazar , & M. Eghtesad, Application and comparison of passivity-based and integrator backstepping control methods for trajectory tracking of rigid-link robot manipulators incorporating motor dynamics, *International Journal of Robotics and Automation*, *22*(3), 2007, 196-205.

23. G. Liu, A. A. Goldenberg, & Y. Zhang, Precise slow motion control of a direct-drive robot arm with velocity estimation and friction compensation, *Mechatronics*, *14*(7), 2004, 821-834.

24. C. Canudas de Wit, H. Olsson, K. J. Astrom, & P. Lischinsky, A new model for control of systems with friction, *IEEE Transactions on Automatic Control*, *40*(3), 1995, 419-425.

25. R. A. Al-Ashoor, Robust adaptive Cartesian control of robot manipulators using bounded uncertainties approach, *International Journal of Robotics and Automation*, *10*(1), 1995, 1-10.

26. M. K. Ciliz, Adaptive control of robot manipulators with neural network based compensation of frictional uncertainties, *Robotica*, *23*(2), 2005, 159-167.

27. P. Tomei, Robust adaptive friction compensation for tracking control of robot manipulators, *IEEE Transactions on Automatic Control*, *45*(11), 2000, 2164-9.

28. J. C. Piedboeuf, J. de Carufel , & R. Harteau, Friction and stick-slip in robots: simulation and experimentation, *Multibody System Dynamics*, *4*(4), 2000, 341-354.

29. M. Grotjahn, M. Daemi, & B. Heimann, Friction and rigid body identification of robot dynamics, *International Journal of Solids and Structures*, *38*(10), 2001, 1889-1902.

30. B. Subudhi , & A. S. Morris, Singular perturbation based neuro-H_∞ control scheme for a manipulator with flexible links and joints, *Robotica*, *24*(2), 2006, 151-161.

31. F. Ghorbel, & M. W. Spong , Integral manifolds of singularity perturbed systems with application to rigid-link flexible-joint multibody systems, *International Journal of Non-Linear Mechanics*, *35*(1), 2000, 133-155.

32. Reference manual of serial flexible joint manipulator, Quanser company, Document No:619, Toronto (2005).

33. M. W. Spong, & R. Ortega, On adaptive inverse dynamics control of rigid robots automatic control, *IEEE Transactions on Automatic Control, 35*(1), 1990, 92-95.

34. B. Siciliano, & O. Khatib, *Springer Handbook of Robotics*, Springer (2008)

35. C. Canudas de Wit, H. Olsson H., K. J. Astrom, & P. Lischinsky, A new model for control of systems with friction, *IEEE Transactions on Automatic Control*, *40*(3), 1995, 419-425.

36. P. Lischinsky, C. Canudas-de-Wit , & G. Morel, Friction compensation of a Schilling hydraulic robot, *Proceedings of IEEE International Conference on Control Applications*, Hartford, CT, USA, 1997, 294-299.

37. H. Salmasi, R. Fotouhi , & P. N. Nikiforuk, On the stability of a friction compensation strategy for flexible-joint manipulators, *Submitted to Advanced Robotics*, March 2009.

38. R. H. A. Hensen, M. J. G. van de Molengraft , & M. Steinbuch, Friction induced hunting limit cycles: A comparison between the LuGre and switch friction model, *Automatica*, *39*(12), 2003, 2131-2137.

Biographies

Hamid Salmasi received the B.Sc. and M.Sc. in Mechanical Engineering from the Sharif University of Technology, Tehran, Iran, in 2003 and 2005, respectively. He is currently working toward the Ph.D. degree in the Mechanical Engineering at the University of Saskatchewan, Saskatoon, Canada. His research interests include Robotics and Vibration Control.

Reza Fotouhi obtained his PhD in Mechanical Engineering from the University of Saskatchewan in Canada. He is currently a professor of Mechanical Engineering at University of Saskatchewan in Canada. His research interests include Robotics (dynamics and control), Structural Dynamics and Vibrations, Computational Mechanics, and Biomechanics.

Peter N. Nikiforuk is Dean Emeritus, College of Engineering, at the University of Saskatchewan, Canada. Previously, he was Dean of Engineering for 23 years, Head of Mechanical Engineering for 7 years and Chair of the Division of Control Engineering for 5 years. He holds the B.Sc. degree in engineering physics from Queen's University in Canada and Ph.D. degree in electrical engineering from Manchester University in England. He received the D.Sc. degree, also from Manchester University, in 1970 for research in control systems. He served as chair or member of five Councils in Canada, was recipient of seven Fellowships in Canada and England and seven other honors, and member of several Boards. His fields of research are Adaptive and Control Systems.

Chapter 5.   Vibration Control of a Flexible Link

Manipulator Using Smart Structure

Vibration Control of a Flexible Link Manipulator Using Smart Structures

H. Salmasi*. R. Fotouhi**, P. N. Nikiforuk ***

* , ** , *** Mechanical Engineering Department, University of Saskatchewan, Saskatoon, Canada;

email:hamid.salmasi@usask.ca, reza.fotouhi@usask.ca, peter.nikiforuk@usask.ca

Abstract: The active vibration suppression of a flexible link manipulator using a smart structure (piezoelectric actuator) is investigated. For this purpose, a Finite Element (FE) model is developed for the modal and transient analysis of a cantilever beam and a flexible link manipulator. The novelty of this work is in the development of an accurate finite element model of a piezoelectric and beam/manipulator. Also, the effect of the placement of the piezoelectric actuator along the beam, based on the controllability of the system states and using FE analysis, is investigated. To avoid system instability, a collocated sensor-actuator pair is used and a proportional control strategy is employed to adjust the voltage applied to the piezoelectric actuator so as to control vibrations. For the flexible link manipulator, it is shown that the vibration is well suppressed during and at the end of a maneuver by locating the piezoelectric actuator at the optimum location. The effect of the controller gain on the vibration behavior of the system is investigated and the optimum controller gain is found using two main evaluation criteria; these are the contribution of the dominant frequencies in the response and the error norms of the vibration amplitudes.

1. INTRODUCTION

Designing and utilizing robot manipulators having higher load capacities is always desired. However, vibration is an important factor that restricts the performance of such devices especially in applications where accurate positioning is very important. In the past decade

131

different approaches have been used for vibration suppression. Active vibration control is one of the best approaches to suppress vibration. One of the methods of active control is using piezeoelectrics as actuators (Lewis and Inman, 2001).

Piezoelectric actuators have been successfully used for vibration suppression in some works. Khajehpour and Golnaraghi (1997) developed a nonlinear controller for vibration control of a cantilever beam using piezoelectric actuators. The optimum placement of the actuators for a cantilevered plate was proposed in (Peng et al., 2005). Effect of the placement of the piezoelectric actuator on the modal and spatial controllability of a structure was analysed in (Moheimani and Ryall, 1999) based on a performance index H_2. This index represents the norm of the input-output characteristics of a dynamical system and can be used to find the optimal placement of the actuator/sensor for plates.

However, in most of the models developed for the control of flexible structures, the controller is designed for a particular range of frequency, and it is common practice to remove the higher modes of vibration which are lying out of the desired range of frequency (Clark, 1997). This approach leads to truncation errors and the closed-loop performance will be considerably different from the predicted theoretical model. In fact, by ignoring the higher modes in the assumed mode shapes method, the zeros of the system are located far from where they should be and as a result the developed model will be different from the original one. One of the methods used to reduce the truncation error is finite element analysis (FEA) (Theodore and Ghosal, 1995). Since a large number of the mode shapes of the system are considered in FEA, the truncation of the error, due to ignoring the higher modes, is minimized in finite element models provided that a reasonably enough number of elements are used.

The main contribution of this paper is in the development of an accurate model of a piezoelectric and beam/manipulator using the finite element (FE) method and finding the optimal placement of the piezoelectric actuator along the flexible structure. Verifying the FE model by analytical calculations and error analysis can be considered as other less important contributions of this paper. It is believed that in the FE model, if the time integration and iterative solver provide accurate solutions, the computer simulations of the manoeuvre of the manipulators, even very flexible ones, will be quite reliable and closer to the experimental measurements. To check the accuracy of the FE model, the natural frequencies of the FE model are calculated and verified

132

using the theoretical approach. The optimal placement of the piezoelectric is then found for the cantilevered beam, based on the controllability of the system, and is then compared with the results of the FEA. In the following, the piezoelectric is utilized for the vibration suppression of the flexible manipulator during the manoeuvre and after reaching the desired position. The effect of the gain on the controller performance is also investigated.

2. MATHEMATICAL FORMULATION

2.1 Piezoelectric Actuator

A cantilever beam with a piezoelectric actuator, shown in Fig. 1, was used in the study described in this paper. For perfectly bonded piezoelectric actuators and assuming an Euler-Bernoulli beam, the moment induced by the applied voltage on the piezoelectric actuator is given as

$$M_p = E_p e_{31}[(V_1(t) - V_2(t))(t_b/2 + t_p/2)] \tag{1}$$

where E_p is the module of elasticity of the piezoelectric element, e_{31} the piezoelectric actuator constant, t_b the thickness of the beam and t_p the thickness of the piezoelectric actuator. $V_1(t)$ and $V_2(t)$ are respectively the applied voltage to the top and bottom surfaces of the piezoelectric actuator, and M_p is the effective bending moment applied to the beam with an equivalent area moment of inertia I_{eq}. By letting $K_s = (1/2)E_p e_{31}(t_b + t_p)$, equation (1) becomes

$$M_p = K_s(V_1(t) - V_2(t)) \tag{2}$$

If the applied voltage to the bottom surface of the piezoelectric actuator is zero ($V_2(t) = 0$), then from equation (2) M_p will be proportional to the applied voltage on the top surface, $M_p = K_s V_1(t)$. If the beam is modeled as a Euler-Bernoulli beam with deflection $y(x,t)$, where x is measured from the fixed end of the beam and t is time, the partial differential equation of the system becomes

$$E_b I_{eq} \frac{\partial^4 y(x,t)}{\partial x^4} + \rho_b A_b \frac{\partial^2 y(x,t)}{\partial x^2} = M_p \frac{\partial}{\partial x}[\delta(x - L_s - L_p) - \delta(x - L_s)] \tag{3}$$

where E_b and ρ_b are the module of elasticity and density of the beam respectively. L_b, L_p and L_s, as shown in Fig. 1, are the length of the beam, length of the piezoelectric actuator, and distance of the piezoelectric actuator from the fixed end respectively, and $\delta(x)$ is the Dirac function. The

133

deflection of the beam can be expressed using assumed mode shapes

$$y(x,t) = \sum_{i=1}^{N} \varphi_i(x) q_i(t), \quad i = 1,2,\cdots,N \tag{4}$$

where φ_i is the i'th normalized mode shape, q_i is the amplitude of the i'th normalized mode shape, and N is the number of the assumed mode shapes. Substituting equation (4) into equation (3), multiplying by φ_i and integrating, equation (3) becomes

$$E_b I_{eq} q_i(t) \int_0^{L_b} \frac{\partial^4 \varphi_i(x)}{\partial x^4} \varphi_j(x) dx + \rho_b A_b \ddot{q}_i(t) \int_0^{L_b} \varphi_i(x)\, \varphi_j(x) dx = K_s V_1 \left[\varphi_i'(x - L_s - L_p) - \varphi_i'(x - L_s) \right], \quad i,j = 1,2,\cdots,N \tag{5}$$

where the dot indicates the time derivative and $()'$ represents the derivation with respect to x. Using the orthogonality property of mode shapes and inclusion the modal damping ratio ξ_i for the i'th normal mode, equation (5) is written as

$$\ddot{q}_i(t) + 2\xi_i \dot{q}_i(t) + \omega_i^2 q_i(t) = F_i V_1(t), \quad i = 1,2,\cdots,N \tag{6}$$

where

$$\omega_i^2 = \frac{E_b I_{eq}}{\rho_b A_b} \int_0^{L_b} \frac{\partial^4 \varphi_i(x)}{\partial x^4} \cdot \varphi_i(x) dx, \quad i = 1,2,\cdots,N \tag{7}$$

$$F_i = \frac{K_s}{\rho_b A_b} \left[\varphi_i'(x - L_s - L_p) - \varphi_i'(x - L_s) \right], \quad i = 1,2,\cdots,N \tag{8}$$

Equation (6) can be written in the state-space form

$$\dot{X}(t) = AX(t) + FV_1(t) \tag{9}$$

where

$$X(t) = \begin{bmatrix} q_1(t) \\ \vdots \\ q_N(t) \\ \dot{q}_1(t) \\ \vdots \\ \dot{q}_N(t) \end{bmatrix}, \quad A = \begin{bmatrix} O_{N\times N} & I_N \\ -\Omega^2 & -2\xi\Omega \end{bmatrix}, \quad F = \begin{bmatrix} O_{N\times 1} \\ F_1 \\ \vdots \\ F_N \end{bmatrix} \tag{10}$$

and $\Omega = \text{diag}(\omega_1, \omega_2, \cdots, \omega_N)$, $\xi = \text{diag}(\xi_1, \xi_2, \cdots, \xi_N)$, $O_{N\times N}$ is a zero matrix of size N, and I_N is an identity matrix of size $N \times N$. Note that as shown in equation (8) the matrix F depends on the location of the piezoelectric, L_s.

The optimum placement of the piezoelectric can be obtained by minimizing the energy of

the control force. In fact, it is desired in minimizing the energy required to steer the initial state $X(t_0)$ to the final state $X(t_1)$. It means that at the final state all modes are well suppressed; that is $q_i(t) = 0$ and $\dot{q}_i(t) = 0$ for $i = 1,2,\cdots,N$. Therefore the final state , $X(t_1)$, must be zero. The value of the minimum energy functional J of the control voltage $V_1(t)$, which steers the initial state $X(t_0)$ to zero, can be written as (Klamka, 1991)

$$J(t_0, t_1; X(t_0)) = X(t_0)^T W^{-1} X(t_0) \tag{11}$$

where W is a controllability Grammian matrix which is the solution of the following Lyapunov equation

$$WA^T + AW + FF^T = 0 \tag{12}$$

The controllability measure μ can be introduced as the reciprocal of the maximum value of the control energy $J(t_0, t_1; X(t_0))$ for all initial states taken from the unit sphere, that is, $\{X(t_0)\epsilon R^n: \|X(t_0)\| = 1\}$; thus

$$1/\mu = \max_{\|X(t_0)\|=1} J(t_0, t_1; X(t_0)) = \lambda_{max}(W^{-1}(t_0, t_1)) = 1/\lambda_{min}(W(t_0, t_1)) \tag{13}$$

where $\lambda_{max}(W^{-1}(t_0, t_1))$ denotes the maximum eigenvalue of W^{-1} which is the inverse of the minimum eigenvalue of W, $\lambda_{min}(W(t_0, t_1))$. To find the optimal placement of the piezoelectric actuator, the control energy in equation (13), must be minimized for different locations of the piezoelectric actuator. In other words, most controllability can be obtained when μ has its maximum value. Based on this approach, the optimal placement of a piezoelectric actuator will be found in Section 4.1 for a cantilevered beam.

2.2 Dynamics of Manipulator

The manipulator shown in Fig. 2 has a hub at the base with a mass moment of inertia J_o, a beam of length L_b, a payload with mass m_p and a mass moment of inertia J_p. The coordinate system (X, Y) is the global coordinate system and (x, y) rotates with angular velocity $\dot{\theta}$ where the angle θ is the rotation of the base. A torque u is applied by the hub (motor) and the arm rotates around its base during the interval time of $(0 < t \leq t_d)$. After reaching the desired angle θ_d, the torque is reduced to zero and the arm behaves as a cantilever beam $(t > t_d)$. Thus, the simulation procedure must be performed in two steps for a rotating flexible manipulator $(0 < t \leq t_d)$ and a

cantilever beam $(t > t_d)$. A piezoelectric actuator is used for vibration suppression of the manipulator during the rotation of the arm and after reaching its desired position.

2.3 Controller Design

A proportional controller was used in which the applied voltage to the piezoelectric actuator was proportional to the axial strain. A block diagram of the controller is shown in the Fig. 3 where K_c, ε, V and V_ε are the gain, strain at the midpoint of the piezoelectric actuator, potentiometer output voltage and applied voltage to the piezoelectric actuator, respectively. To avoid instability due to the non-collocation of sensor and actuators, the actuator and sensor were located at the same location; that is the strain ε was measured at the location of the piezoelectric actuator. The set point (for error) was selected as zero. An important issue in vibration control of flexible structures is the collocation of sensor and actuator. In this study, a collocated sensor-actuator pair is used. The collocation of sensor and actuator guarantees that the system is positive real at least for lower frequency modes. However, this guarantee does not apply to higher frequency modes, because the collocation principle does not apply to modes of wavelength comparable to the size of piezoelectric actuator. In addition, computational delays at high frequencies can drive some higher frequency modes unstable (Falangas, 1994). Therefore, the collocation of the sensor and actuator does not necessarily lead to the stability of the controller. Another factor affecting the stability criteria is the proper location of the piezoelectric which is discussed later in this paper.

3. FINITE ELEMENT MODEL

Three types of elements from the ANSYS Software elements library were used to model the beam/manipulator. The beam was constructed using ten "PLANE 82" elements spaced equally along the beam. This element had eight nodes with two degrees-of-freedom (DOF), and translations in the x and y directions at each node. Since "PLANE 82" did not have a rotational degree of freedom, two "BEAM 3" elements having three degrees of freedom, translations in the nodal x and y directions as well as rotation in the z-direction, were used for the base rotation. The element "PLANE 223", which models the piezoelectric actuator, was used as an actuator to suppress the vibration. The physical properties of the beam and piezoelectric actuator shown in Figs. 1 and 2, are given as follows

$L_s = 0.030\ m, L_b = 0.200\ m, t_b = 0.001\ m,$

$I_b = 8.33 \times 10^{-11}\ m^4, t_p = 0.001\ m,$

$v = 0.300, \rho_b = 7.80 \times 10^3\ kg.m^{-3},$

$J_o = 0\ kg.m^2, J_p = 0\ kg.m^2, m_p = 0\ kg,$

$E_b = 201 \times 10^9\ N.m^{-2}, L_p = 0.010\ m$

where L_b, L_p and L_s are, respectively, the length of the beam, length of the piezoelectric actuator, and distance of the piezoelectric actuator from the fixed end, and t_b and t_p are respectively the thicknesses of the beam and piezoelectric actuator. E_b, I_b, v and ρ_b are the modulus of elasticity, area moment of inertia, Poisson ratio and density of the beam respectively, and m_p, J_o and J_p are the payload mass, mass moment of inertia of the hub and mass moment of inertia of the payload.

4. SIMULATION RESULTS

In the simulation study, both modal and transient analyses were carried out for the cantilever beam and for the robot flexible link manipulator. The simulation was performed in three steps. In the first step, the free vibration and modal analysis of the cantilever beam was studied. The natural frequencies of the manipulator which were determined theoretically and using finite element analysis (FEA) are illustrated in table 1. The results obtained from the theoretical approach and FEA are in good agreement. In the next step, the effect of placement of the piezoelectric actuator on the vibration was studied and the optimal location of the piezoelectric actuator along the beam was determined. Finally, the active vibration suppression of the robot flexible link manipulator during and at the end the manoeuvre was successfully accomplished, and the effect of the gain on the vibration behaviour of the system was determined. In this study, it was assumed that the base was fixed and the beam behaved as a cantilever.

4.1 Optimum location of the Piezoelectric Actuator

Based on the approach described in Section 2.1, the optimum placement of the piezoelectric was found for the cantilevered beam. For this purpose, the first two mode shapes were considered and the eigenvalues of the controllability Grammian matrix, W, were found for different locations of the piezoelectric actuator using the Lyapunov equation (12). Values of μ versus L_s/L_b, are plotted in Fig. 4. It can be seen that the location $L_s/L_b = 0.3$ had the

maximum value and provided the most controllability.

To verify the optimal placement of the piezoelectric actuator, $L_s/L_b = 0.3$ the simulation was performed using the finite element model for different values of L_s/L_b. To find the best location of the actuator, the following evaluation criteria were used

$$E_{0-3} = \sqrt{\frac{1}{N_3-1}\sum_{i=0}^{i=N_3}\left(\frac{y_{i,e}}{y_{max,e}}\right)^2} \qquad (14)$$

$$E_{2-3} = \sqrt{\frac{1}{N_3-N_2}\sum_{i=N_2}^{i=N_3}\left(\frac{y_{i,e}}{y_{max,e}}\right)^2} \qquad (15)$$

where the norms E_{0-3} and E_{2-3} represent the values of the normalized tip deflections for the time intervals of $(0 \le t \le 3)$ and $(2 \le t \le 3)$, respectively. The $y_{i,e}$ is the tip deflection of the beam at the time step i, N_3 is the number of time steps at $t = 3$ and N_2 is the number of time steps at $t = 2$. Table 2 illustrates the values of these norms for the different cases investigated. The values of E_{0-3} and E_{2-3} are plotted versus L_s/L_b in Fig. 5. According to this figure, $L_s/L_b = 0.3$ corresponds to the best location of the piezoelectric actuator. This finding is also consistent with the findings of (Peng, 2005) for a similar beam.

4.2 Flexible link robot manipulator

To verify the effectiveness of the piezoelectric actuator in suppressing the vibration of a robot manipulator, a single flexible manipulator was analyzed. In this case, the manipulator could rotate about its base. The physical properties and the dimensions were the same as those of the cantilever beam, except the values of the mass moment of inertia of the hub and the tip-mass which were selected as $J_o = 1.2 \times 10^{-3}$ kg. m^2 and $m_p = 0.2$ kg respectively. The torque applied to the hub was of a bang-bang nature causing, as shown in Fig. 6.a, the manipulator initially to accelerate, then decelerate and finally to lock at its desired final position, where it continued to vibrate as a cantilever beam. As shown in Fig. 6.b, the hub rotated approximately 0.8 *rad* in one second and it was locked then at 0.8 *rad*. The natural frequencies of the manipulator and cantilever beam were obtained theoretically and compared in table 1 against the FEA results. Fig. 7.a illustrates the tip deflection with respect to the shadow beam (see Fig. 2) without the controller being active ($K_c = 0$). To find the dominant frequencies of the system, the

FFT of the tip deflections in time was evaluated. This is illustrated in Fig. 7.b which indicates three dominant frequencies. The first was the main excitation frequency which was $1.0\,Hz$. The second frequency was approximately $17\,Hz$ which corresponded to the first natural frequency of the cantilever beam and the third frequency, which was approximately $60\,Hz$, corresponded to the first non-zero natural frequency of the flexible link manipulator. To suppress the vibration a piezoelectric actuator was placed at the optimum location, $L_s/L_b = 0.3$, as reported in Section 4.1. The simulation was carried out for three different values of the controller gain, $K_c = 2.00\mathrm{e}5, 4.00\mathrm{e}5$ and $6.00\mathrm{e}5$, and these are referred to as Cases 2, 3 and 4 respectively. The vibration was well suppressed during and at the end of the manoeuvre as shown in Fig. 8.a for Case 3 ($K_c = 4.00\mathrm{e}5$). The FFT of the tip deflection in time is shown in Fig. 8.b for this case. According to this figure, the peak values of the dominant frequencies, especially the main excitation frequency and the first natural frequency of the cantilever beam, were significantly reduced for Case 3 in comparison with Case 1 (Fig. 7).

Three evaluation criteria, E_{0-1} for $0 \le t \le 1$ (during the manoeuvre), E_{1-4} for $1 \le t < 4$ (at the end of the manoeuvre) and E_{0-4} for $0 \le t < 4$ (the total response), were defined so as to compare the results. The values of these norms were the normalized tip deflections of the manipulator arm and were calculated using equations similar to those reported for the cantilever beam (equations (14) and (15)). These norms are compared in Fig. 9.a for different gain values. As shown in Fig. 9.a, the gain value of Case 3 ($K_c = 4.00\mathrm{e}5$) had the smallest values of norms E_{1-4} and E_{0-4} in comparison with other gain values. Thus the amplitude of vibration was smaller for Case 3 than other cases, after the manipulator reached its desired rotation during $1 \le t < 4$, as well as during the total response ($0 \le t < 4$).

Another index which was used to compare the results was the values of the PSD peaks at the dominant frequencies. This index is shown in Fig. 9.b for four different cases. Also, for the three dominant frequencies, overall Case 3 shows the best result in suppressing the vibration.

5. CONCLUSIONS

Finite element analysis (FEA) was used in this paper for modeling a cantilever beam and a flexible robot manipulator. The optimum values for the controller gain were found and the optimum location of the piezoelectric actuator was determined for the cantilever beam based on

minimizing the energy of the control force and was verified by FEA. The controller was stable because of using a collocated sensor-actuator pair in the optimum position and because of using full non-linear transient dynamic analysis using FEA. Also, it was concluded that Case 3 with a controller gain of Kc= 4.00e5 and the location of the piezoelectric actuator 30% of the beam length from the base, produced the best results as far as suppressing the vibration was concerned. These findings were verified by analytical calculations and will be verified experimentally in near future.

6. REFERENCES

ANSYS Software ANSYS Inc., Canonsburg, PA, USA (www.ansys.com)

Chen C. Q. and Shen Y. (1997). "Optimal control of active structures with piezoelectric modal sensors and actuators," *Smart Materials and Structures* **6(4)** 403-9.

Clark R. L. (1997). "Accounting for out-of-bandwidth modes in the assumed modes approach: implications on collocated output feedback control," *Journal of Dynamic Systems, Measurement, and Control* **119(3)** 390-395.

De Luca A. and Siciliano B. (1991). "Closed-form dynamic model of planar multilink lightweight robots," *IEEE Transactions on Systems, Man and Cybernetics* **21(4)** 826-39.

Devasia S., Meressi T., Paden B. and Bayo E. (1993). "Piezoelectric actuator design for vibration suppression: placement and sizing," *Journal of Guidance, Control, and Dynamics* **16(5)** 859-64.

Falangas E. T., Dworak J. A. and Koshigoe S. (1994). "Controlling plate vibrations using piezoelectric actuators," *IEEE Control Systems Magazine* **14(4)** 34-41.

Khajepour A. and Golnaraghi M.F., (1997). "Experimental control of flexible structures using nonlinear modal coupling: forced and free vibration," *Journal of Intelligent Material Systems and Structures* **8(8)** 697-710.

Khorrami F., Zeinoun I. and Tome E. (1993). "Experimental results on active control of flexible-link manipulators with embedded piezoceramics," *Proc. of IEEE International Conference on Robotics and Automation* (Atlanta, GA, USA) **3** 222-227.

Klamka J. (1991). "*Controllability of dynamical systems*," Boston, Kluwer Academic Publishers.

Lewis J. A. and Inman D. J. (2001). "Finite element modeling and active control of an inflated torus using piezoelectric devices," *Journal of Intelligent Material Systems and Structures* **12(12)** 819-33.

Manning W. J., Plummer A. R. and Levesley M. C. (2000). "Vibration control of a flexible beam with integrated actuators and sensors," *Smart Materials and Structures* **9(6)** 932-39.

Moheimani S. O. R. and Ryall T. (1999). "Considerations on placement of piezoceramic actuators that are used in structural vibration control," *Proc. of the 38th IEEE Conference on Decision and Control* (Phoenix, AZ, USA) **2** 1118-23.

Peng F., Ng A. and Hu Y. (2005). "Actuator placement optimization and adaptive vibration control of plate smart structures," *Journal of Intelligent Material Systems and Structures* **16(3)** 263-71.

Theodore R. J. and Ghosal A. (1995). "Comparison of the assumed modes and finite element models for flexible multilink manipulators," *International Journal of Robotics Research* **14(2)** 91-111.

Table 1. The natural frequencies of the flexible manipulator and cantilever beam

Set	Flexible link manipulator		Cantilever beam	
	Theoretical (Hz)	FEA (Hz)	Theoretical (Hz)	FEA (Hz)
1	0	0	16.97	16.91
2	61.94	61.41	112.6	110.5
3	145.6	144.5	325.7	322.9

Table 2. Evaluation criteria for different locations of actuator

.05	.1	.2	**.3**	.4	.5
.3917	.2999	.2848	**.2845**	.2938	.3106
.2084	.0799	.063	**.063**	.0731	.0925
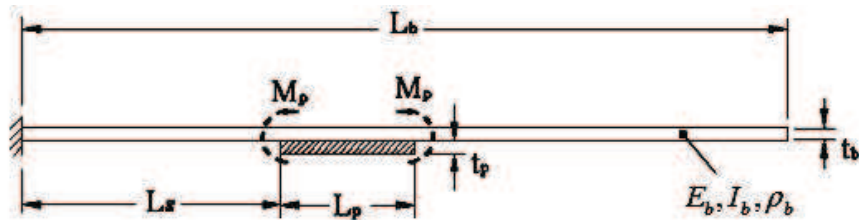
Fig. 1. Model of a cantilever beam with piezoelectric actuator
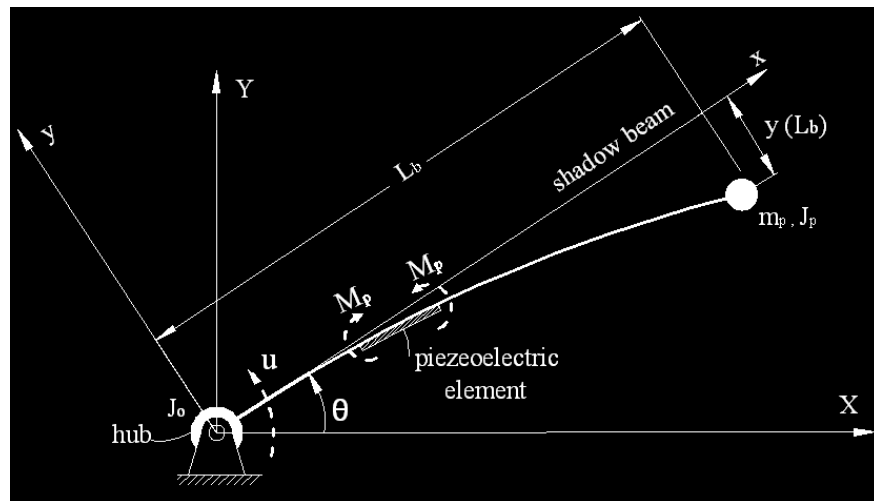
Fig. 2. A single flexible link robot manipulator including its tip mass and hub inertia
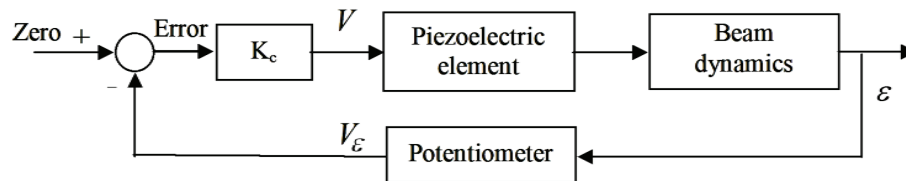
Fig. 3. Block diagram of the controlling vibration of the manipulator
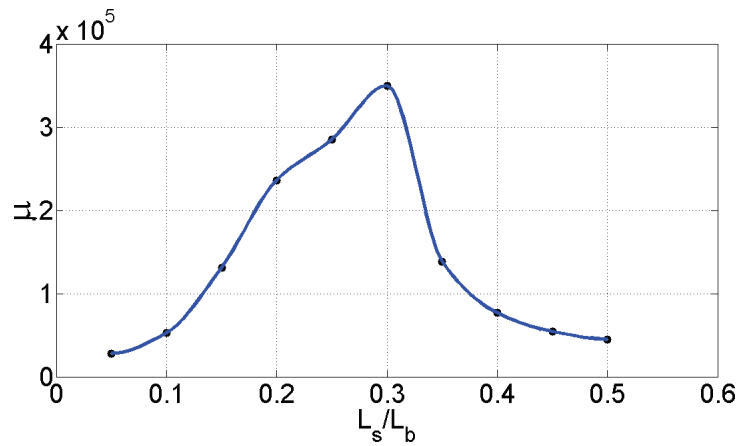
Fig. 4. Controllability measure for different locations of the piezoelectric actuator

143
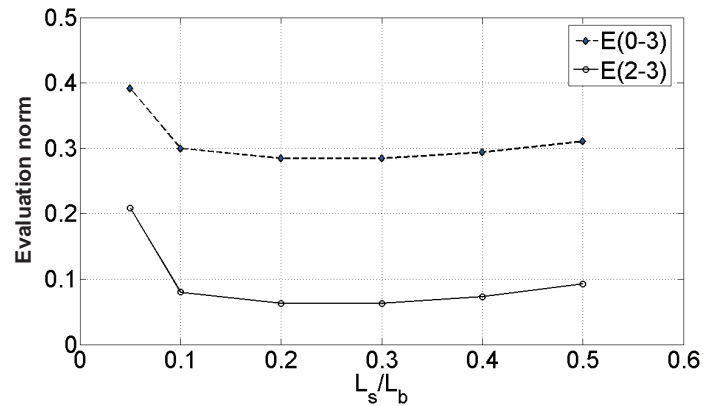
Fig. 5. Norms of normalized tip deflection of cantilever beam for optimum location of piezoelectric actuator
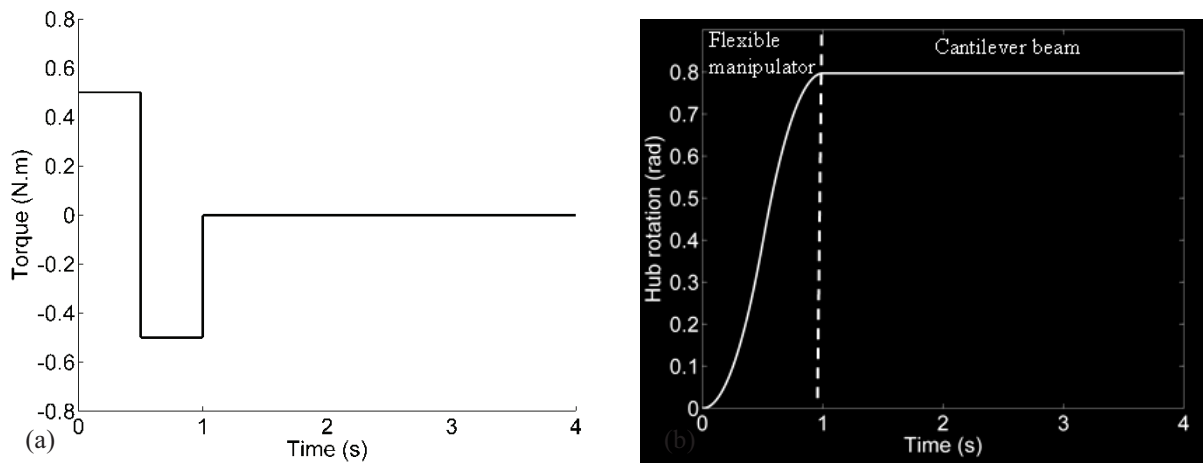
Fig. 6.(a) Applied bang-bang controller torque, and (b) hub rotation.
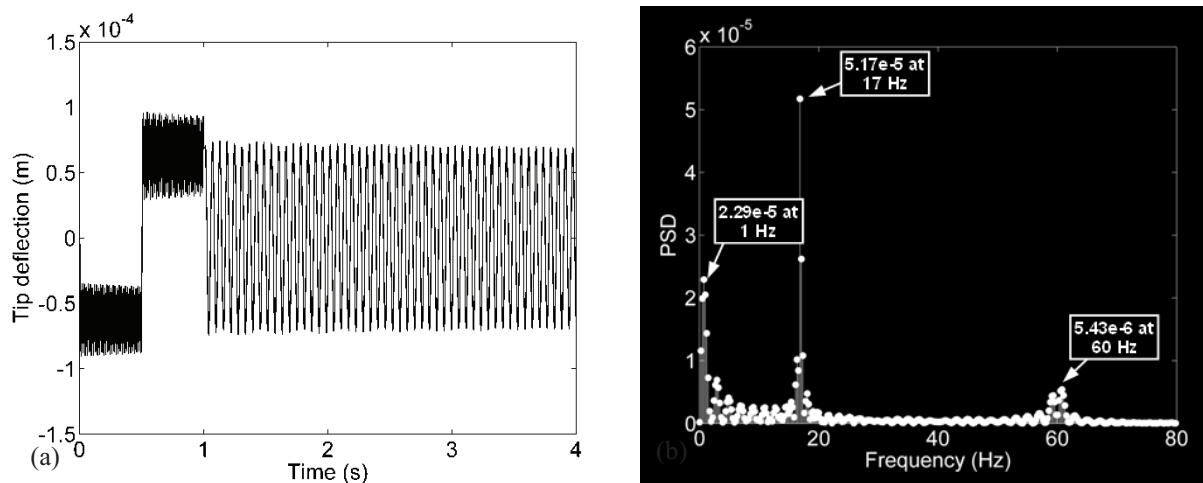
Fig. 7. Case 1 (K_c= 0): Single-link flexible manipulator, (a) tip deflection w.r.t. shadow beam, and (b) FFT spectrum of tip deflection

144
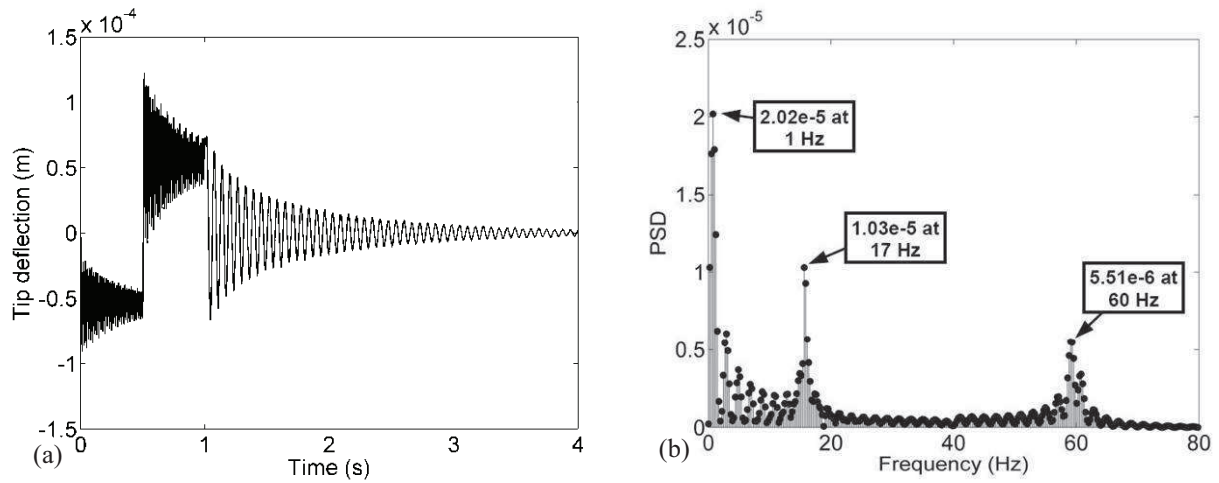
Fig. 8. Case 3 (Kc=4×10^5): Single-link flexible manipulator, (a) tip deflection w.r.t. shadow beam, and (b) FFT spectrum of tip deflection.
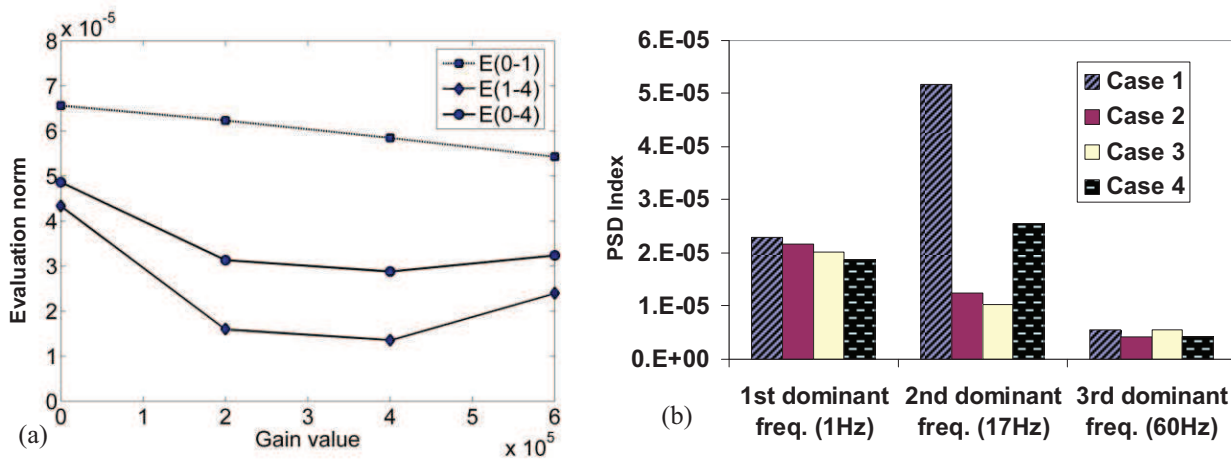
Fig. 9. Single-link flexible manipulator, evaluation criteria for different gain values, (a) norms of vibration amplitudes, and (b) peak values of FFT spectrums at dominant frequencies.

145

Chapter 6. Dynamic modeling of a manipulator with flexible links and flexible joints

Dynamic modeling of a manipulator with flexible links and flexible joints

Hamid Salmasi, Reza Fotouhi, Peter Nikiforuk

Mechanical Engineering Department, University of Saskatchewan, Saskatoon, Canada, S7N 5A9

hamid.salmasi@usask.ca, reza.fotouhi@usask.ca, peter.nikiforuk@usask.ca

1. Introduction

A wide variety of robots is now employed in different areas such as spacecraft and vehicle manufacturing. However, designing and utilizing lighter robots with flexible arms has always been desired. Flexible manipulators have a number of advantages: they require less material, weigh less, consume less energy, are more transportable and maneuverable, cost less and have a higher payload to robot weight ratio [1]. In this paper, the combination of the Lagrange method and assumed mode shapes method (LAMM), has been used for the dynamic modeling of flexible manipulators considering flexibility in the joints and links. The model is then verified by full non-linear finite element analysis (FEA).

2. Mathematical Model

2.1 Kinematics of flexible manipulator

A manipulator consisting of n flexible links interconnected with flexible joints was considered. The model of the ith flexible-link flexible-joint manipulator is shown in Figure 1. The frame

$(\hat{X}_i, \hat{Y}_i)$ is attached to the rigid-like links and $(\hat{x}_i, \hat{y}_i)$ represents the rotating frame. Angles α_i and θ_i are the motor and link angles respectively measured with respect to the rigid frame. The velocity of an arbitrary point along the beam, V_p, can be written as

$$\bar{V}_p^i = \bar{V}_o^i + \bar{\omega}_i \times \bar{r} + \bar{V}_{rel}^i \tag{1}$$

where $\bar{V}_o^i$ is the absolute velocity of the coordinate system (x_i, y_i), $\bar{V}_{rel}^i$ is the relative velocity of point $p(x_i, y_i)$ with respect to the coordinate system (x_i, y_i), $\bar{\omega}_i$ is the absolute angular velocity of the coordinate system $(\hat{X}_i, \hat{Y}_i)$, $\bar{r}$ is the position vector of the point $p(x_i, y_i)$, and y_i is the link deflection, where $(0 \leq x_i < l_i)$ and l_i is the length of the ith link.

The assumed mode shapes method can be used to approximate the link deflection as follows

$$y_i(x_i) = \sum_{j=1}^{m} \varphi_{ij}(x_i)\, \delta_{ij}(t) \tag{2}$$

where m is the number of mode shapes used for each link, and δ_{ij} is the weight of the assumed mode shape φ_{ij}.
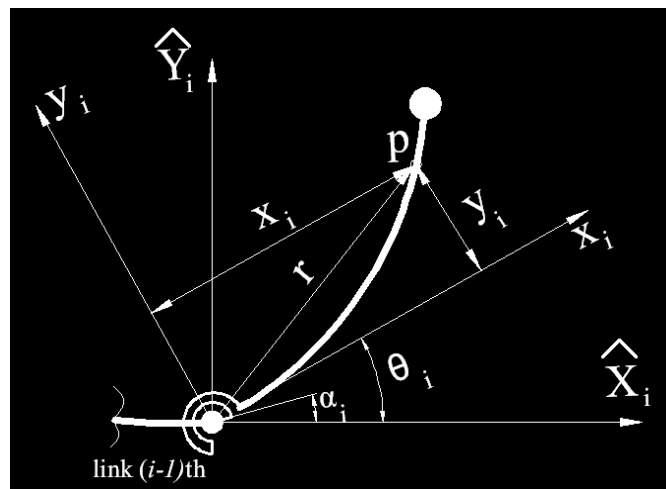
Figure 1. Model of the ith flexible-link flexible-joint manipulator

2.2 Dynamics of flexible manipulator

The equations of motion of a system can often be expressed in terms of generalized coordinates, q_i, using Lagrange's equations. In general, Lagrange's equation for a system with n degrees of freedom can be expressed as

$$\frac{d}{dt}\frac{\partial}{\partial \dot{q}_i}T - \frac{\partial}{\partial q_i}T + \frac{\partial}{\partial q_i}U = \tau_i, \quad i = 1,2,\cdots,n \tag{3}$$

where T, U and τ_i are the kinetic and potential energies of the system, and the torque applied to the ith motor respectively.

The kinetic energy of a flexible-link flexible-joint manipulator is composed of the kinetic energies of the rotors, T_r, links, T_l, hubs, T_h, and the payload mass, T_p,

$$T = T_r + T_l + T_h + T_p \tag{4}$$

where

$$T_r = \frac{1}{2}\sum_{i=1}^{n} I_r^i \dot{\alpha}_i^2 \tag{5}$$

$$T_h = \frac{1}{2}\sum_{i=1}^{n} I_h^i \dot{\theta}_i^2 + \frac{1}{2}\sum_{i=1}^{n} m_h^i \left(\bar{V}_0^i\right)^2 \tag{6}$$

$$T_p = \frac{1}{2}I_p \dot{\theta}_n^2 + \frac{1}{2}m_p (\bar{V}_0^n)^2 \tag{7}$$

$$T_l = \frac{1}{2}\sum_{i=1}^{n} \int_0^{l_i} \rho_i \left(V_p^i \cdot V_p^i\right)dx \tag{8}$$

where I_r, I_h and I_p are respectively the mass moment of inertias of the rotor, hub, and tip, and m_p, m_h and ρ are respectively the payload mass, hub mass and mass per unit length of each link. The potential energy is the sum of the elastic energies stored in the links and the potential energy due to joints flexibility.

$$U = \frac{1}{2}\sum_{i=1}^{n} \int_0^{l_i}(EI)_i \left[\frac{d^2 y_i(x_i)}{dx_i^2}\right]^2 dx + \frac{1}{2}\sum_{i=1}^{n} k_i(\theta_i - \alpha_i)^2 \tag{9}$$

where $(EI)_i$ and k_i are respectively the rigidity of the ith link and stiffness of the ith joint. By substituting the values of the kinetic and potential energies into equation 3, the dynamic equation of system can be described in matrix form as

$$M(q)\ddot{q} + C(q,\dot{q}) + Kq = \tau \tag{10}$$

where M, C, K and τ are the mass matrix, vector of Coriolis and centrifugal forces, stiffness matrix, and vector of applied torques to motors respectively.

3. Simulation

In order to test above procedure, a two flexible-link flexible-joint manipulator (TFLFJ), shown in Figure 2, was considered with the following physical properties

were $l_1 = l_2 = 0.5\ m$, $(EI)_1 = (EI)_1 = 4.8 \times 10^{11}\ N \cdot m^2$, $I_{r_1} = I_{r_2} = 1 \times 10^{-2}\ kg \cdot m^2$, $\rho_1 = \rho_2 = 0.39\ kg/m$, $I_p = 5 \times 10^{-4}\ kg \cdot m^2$, $k_1 = k_2 = 5.0\ N \cdot m/rad$, $m_{h_1} = m_{h_2} = 0.50\ kg$, $m_p = 0.10\ kg$.
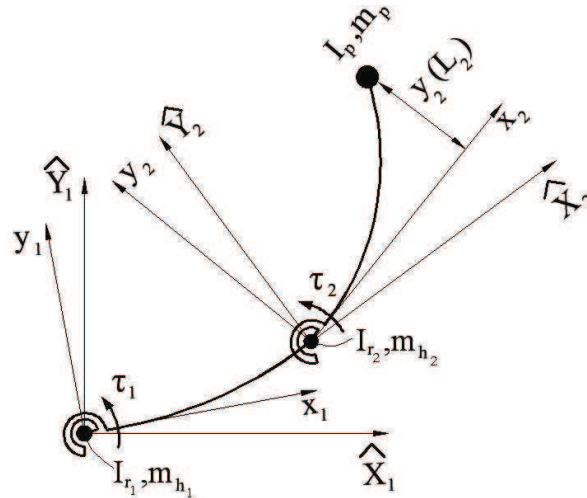
Figure 2. Two flexible-link flexible-joint manipulator (TFLFJ)

150

By assuming two mode shapes for each link, two rotations for the motors and two rotations for the links, it is seen that eight degrees of freedom contribute to the dynamics of the TFLFJ.

The simulation was carried out using two approaches including full nonlinear finite element analysis (FEA-ANSYS) and LAMM. The time step in both simulations was 1e-4s. For finite element analysis, ten BEAM3 elements were used to model each link. This element had three degrees of freedom, translations in nodal *x* and *y* directions and rotation in the *z*-direction at each of its two nodes.

Figure 3 shows the applied torques to the shoulder and elbow motors. Tip deflections of the manipulator are shown in Figure 4 for FEA and LAMM. As shown in this figure, the simulation results of the FEA confirm the results of the LAMM.
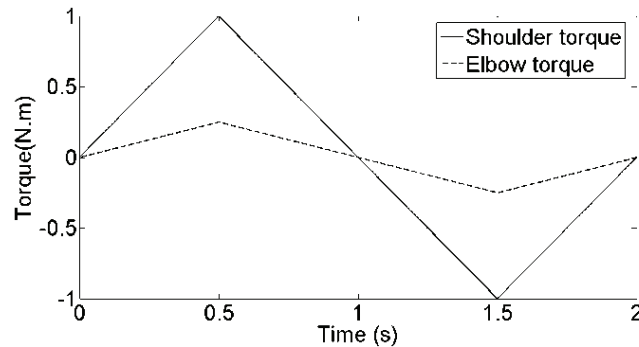
Figure 3. Applied torques to shoulder and elbow motors
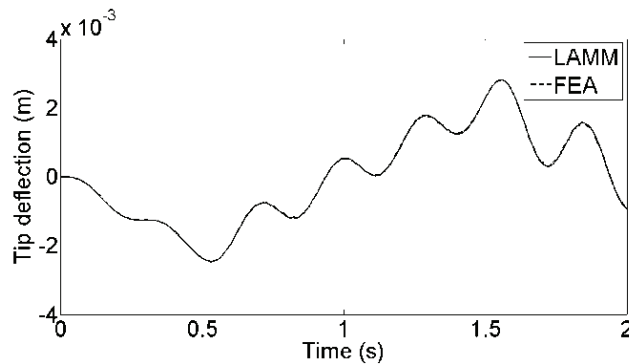
Figure 4. Tip deflection of the manipulator $(y_2(L_2))$

4. Conclusions

The dynamic modeling of a flexible-link flexible-joint manipulator was studied in this paper. A combination of the Lagrange method and the assumed mode shape method (LAMM) was employed for the dynamic modeling. The simulation was carried out for a TFLFJ using LAMM and ANSYS full non-linear finite element analysis. It was shown that the results of the dynamic model are in an excellent agreement with the FEA results.

5. References

[1] Vakil M., Fotouhi R., Nikiforuk P. N., 2006, "Systematic dynamic modeling of flexible link manipulator", CSME Forum, Calgary, Canada.

Chapter 7.   Conclusions, Contributions, and Future Works

In this dissertation, the dynamics and control of flexible-joint robot manipulators were studied, and new controllers for the trajectory tracking were developed. In addition, the dynamics of flexible-link flexible-joint robot manipulators were modelled, and a piezoelectric actuator was utilized to suppress the vibrations during the manoeuvre of the manipulator. Out of this research, eleven research papers were submitted/published in technical journals and international conferences. Five of these papers were selected and presented in Chapters 2-6. A summary of these papers is given in the following Section 7.1. Also, the novelties and contributions of this study are discussed in Section 7.2. The potential future work which can be done in the continuation of this work is presented in Section 7.3.

7.1 Summary and conclusions

New control strategies have been proposed for the tip-trajectory tracking of flexible (elastic) joint robot manipulators in this research work. The control method presented in Chapter 2 was a combination of a composite controller and a LuGre-PD compensator. The composite controller, which was developed using the singular perturbation theory and integral manifold concept, had two parts: slow and fast controllers. To compensate for the friction effect in the joints, a combination of the LuGre model, which was a dynamic non-linear friction model, and a PD compensator was used. The proposed approach was verified experimentally using experimental setups of a single-rigid-link flexible-joint (SRLFJ) and a two-rigid-link flexible-joint (TRLFJ) manipulators. According to the experimental results obtained by these SRLFJ and TRLFJ manipulators, the proposed control strategy was successful in trajectory tracking such that the error between the actual and desired rotations of the links remained very small during and at the end of the manoeuvre of the manipulator.

154

A novel friction compensation strategy was introduced in Chapter 3 to compensate for the friction in the joints. This strategy was developed using the Work-Energy (WE) principle, and it was a linear forward compensating torque which could be identified in only two steps. The friction method was then employed along with the composite controller for the tip trajectory tracking of flexible joint manipulators. The effectiveness of the Work-Energy method was experimentally verified using an experimental setup of the SRLFJ manipulator. For this purpose, the performance of the friction compensation strategy was tested for different trajectory shapes. To analyze the experimental data, two evaluation criteria were defined based on the tracking errors during and at the end of the manoeuvre of the manipulator. According to these criteria, the WE method was superior to the traditional LuGre method used to compensate for the friction.

Chapter 4 presents a novel biologically-inspired controller, which is referred to as the swarm controller, for the tip trajectory tracking of flexible-joint manipulators. This method was inspired by real biological systems such as swarm of birds or school of fishes, and it was a self-organized robust technique in which the applied torques were regulated based on the local and global errors observed in the links' rotations and the end-effector's position. Combination of the swarm controller and the LuGre-PD method was experimentally examined using a TRLFJ manipulator. The experimental results which were obtained for different trajectories and different speeds indicated that the method was effective such that the tracking error was almost zero during the performance of the manipulator.

In Chapter 5, the application of a piezoelectric actuator for the vibration suppression of a single flexible-link manipulator was studied. The optimum placement of the piezoelectric actuator was found based on the controllability of the system states and using finite element analysis. To avoid system instability, a collocated sensor-actuator pair was implemented and a

proportional control strategy was employed to adjust the voltage applied to the piezoelectric actuator. Investigation of the effect of the time delay between the input and output of the controller and the stability analysis of the approach were other parts of this study presented in a technical journal paper and is currently under review.

Chapter 6 describes the dynamic modeling of flexible-link flexible-joint manipulators. The Lagrange method, in combination with the assumed modes shapes method, was used to derive the dynamic equations. The kinetic and potential energies for a two flexible-link flexible-joint manipulator were obtained and substituted in the Lagrange's equations to derive dynamic equations. The method was then verified using the finite-element analysis.

7.2 Contributions of the study

The contributions of this research are as follows:

7.2.1 Developing a new composite controller for flexible-joint manipulators

In singular perturbation models developed for flexible-joint manipulators, the inertias of the rotors are usually ignored. This assumption may deteriorate the performance of the controller and leads to error in trajectory tracking which is crucial in high-precision manipulation tasks such as producing circuit boards. In this study, a more accurate dynamic model which took into account the inertias of rotors was developed. The correctness of the dynamic model was validated using finite-element analysis (FEA). For this purpose, an accurate finite element model of a two-rigid-link flexible-joint manipulator was developed. Simulations were then performed for the finite element and singular perturbation models. The comparison between these models indicated that the simulation results were in very good agreement. Results are given in Chapters 2, 3 and 4.

7.2.2 Constructing a new biologically-inspired controller (swarm controller) for the tip trajectory tracking of manipulators

Based on the movement of real biological systems, a new control strategy was proposed and developed for the flexible-joint manipulators. This approach was successfully implemented to control a two rigid-link flexible-joint manipulator. Experimental results showed the success of this controller in tip trajectory tracking for the TRLFJ. The simplicity and accuracy of the swarm controller were among its advantages. Results are given in Chapter 4.

7.2.3 Designing the LuGre-PD friction compensation strategy

This novel strategy was developed to compensate for the friction effect in harmonic drives. The second method of Lyapunov was utilized to find sufficient conditions for the global asymptotic stability of the LuGre-PD friction compensating torque. The effectiveness of the proposed method was also experimentally proven for different trajectories and manipulation speeds. Results are in Chapter 2.

7.2.4 Developing a friction compensating torque based on the Work-Energy principle

This new approach was a linear forward torque and had only two parameters to be identified. Therefore, compared to other friction compensation approaches, it was easier to implement and simpler to identify. The performance of this friction compensation strategy was verified using experimental setup of the SRLFJ. Results are in Chapter 3.

7.2.5 Application of a piezoelectric actuator for vibration suppression

An accurate finite element model of a piezoelectric and beam/manipulator was derived. Finding the optimal placement of the piezoelectric actuator and the stability analysis of the approach were other novelties of this work. Results are in Chapter 5.

7.2.6 Deriving a comprehensive dynamic model for flexible-link flexible-joint manipulators

Dynamic equations of flexible-link flexible-joint manipulators were derived using Lagrange's equations and assumed mode shapes method. The developed model was validated with FEA. Compared to other dynamic models this method was more accurate since it took into account both flexibilities in the joint and links. Results are in Chapter 6 and Appendix II.

7.3 Future work

The results of this study provide a strong foundation for further research in the dynamic modelling and control of robot manipulators. Some of the potential future work in this area are as follows:

1- Improving the swarm control strategy: In this study, the swarm control strategy was developed for the tip trajectory tracking of flexible-joint manipulators and its performance was experimentally validated. A stability analysis of this approach can ensure that the controller will be stable in different working conditions. For this purpose, the stability analysis approaches developed for the non-linear systems such as Lyapunov's theorem may be applied.

2- Employing the swarm control strategy for flexible-link flexible-joint manipulators: Swarm control strategy was used for the tip trajectory tracking of flexible-joint manipulators in this study. As a possible extension, this controller can be altered for manipulators with flexibility in both joints and links.

3- Finding the optimal placement of a piezoelectric actuator experimentally: The optimal location of a piezoelectric actuator was found using the controllability of the states and FEA in this thesis. While the results obtained using finite-element models are reliable, experiments can verify the correctness of the optimal position of the piezoelectric actuator found using FEA.

Therefore, finding the optimimim location of a piezoelectric actuator through the experiments is recommended as an extension for this study.

4- Investigating the effect of joints' damping on the performance of the controllers: The performance of the developed controllers in this thesis can be examined for different joints' damping. This can be experimentally carried out using experimental modules of SRLFJ and TRLFJ. Also, analyzing the effect of the damping on the stability of the developed controllers can be another future work.

Appendix I: List of experiments carried out to verify the proposed control strategies

The experiments performed to verify the developed control strategies in Chapters 2-4 are listed in this Section. Table AI.1 lists the experiments carried out using different friction compensation strategies for different trajectory shapes, joint stiffness and final rotations. In these experiments, the experimental module of the single rigid-link flexible-joint manipulator, shown in Fig. 2 (Chapter 1), was employed.

The lists of the experiments performed using two-rigid-link flexible-joint manipulator, shown in Fig. 3 (Chapter 1), are given in Tables AI.2 and AI.3. Table AI.2 lists the experiments carried out to compare the performance of composite and rigid controllers for different working conditions, and Table AI.3 lists the experiments carried out using the swarm controller. In these experiments, the friction compensation strategy was the LuGre-PD method. The results of these experiments have been explained and discussed in Chapters 2-4.

Table AI.1. List of the experiments carried out using the single rigid-link flexible-joint manipulator

Friction compensation method	Trajectory shape				Joint stiffness		Controller type		Final rotation (rad)			No
	3rd-order	5th-order	7th-order	9th-order	Low	High	Composite	Rigid	0.5	1	1.5	
LuGre				x		x	x		x			4
				x		x	x			x		2
				x		x	x				x	2
				x	x		x		x			2
				x	x		x			x		2
				x	x		x				x	2
Work-Energy	x					x	x		x			6
		x				x	x		x			9
			x			x	x		x			3
				x		x	x		x			4
				x		x		x	x			2
LuGre+PD				x	x		x		x			3
				x	x		x			x		3
				x	x		x				x	3
				x		x	x		x			4
				x		x	x			x		3
				x		x	x				x	3

Table AI.2. List of the experiments carried out using the TRLFJ manipulator

Trajectory shape Shoulder		Trajectory shape Elbow		Joint stiffness		Controller type		Final rotation Shoulder (rad)		Final rotation Elbow (rad)		No.
3rd-Order	9th-order	3rd-order	9th-Order	Low	High	Composite	Rigid	1	1.5	1	1.5	
x		x			x	x		x		x		4
x			x		x	x		x		x		3
	x	x			x	x		x		x		3
	x		x		x	x		x			x	2
	x	x			x		x	x			x	2
	x		x		x	x				x		3
	x	x			x		x			x		2
	x		x		x	x		x		x		4
	x	x			x		x			x		2
	x		x		x	x		x		x		3
	x	x			x	x		x			x	3
	x	x			x	x		x		x		3
	x	x			x	x		x			x	3
	x	x			x	x		x		x		3
	x		x		x	x		x			x	3

Table AI.3. List of the experiments carried out using the swarm controller and LuGre-PD friction compensation method for the TRLFJ manipulator

Speed			Controller type		Final rotations of both Shoulder and Elbow (rad)					No.
Slow	Moderate	Fast	Swarm	Rigid	0.5	1.0	1.5	2.0	2.5	
■			■		■					2
■			■			■				2
■			■				■			2
■			■					■		2
■			■						■	2
	■		■				■			3
		■	■				■			2
■				■			■			3

162

Appendix II: Dynamic modelling of TRLFJ and TFLFJ

The dynamic modelling of a two rigid-link flexible link manipulator (TRLFL) and a two flexible-link flexible-joint manipulator (TFLFL) are presented in this Section. The approach used to develop dynamic models for flexible manipulators was Lagrange's method. Based on this method, the kinetic and potential energies of the system were first obtained, and using Lagrange's equations the dynamic equations were then derived. The correctness of the dynamic models was verified using finite-element analysis (FEA) for both TRLFJ and TFLFJ.

AII.1. Dynamic modelling of TRLFJ:

As shown in Fig. 3 (Chapter 1) TRLFJ had two flexible joints and two rigid links. Thus, it had four degrees of freedom (DOF). Two DOF's (θ_1, θ_2) were related to the rotations of the links, and the other two DOF's (θ_3, θ_4) represented the rotations of motors. The Lagrange's equations were used to extract the dynamic equations in terms of generalized coordinates. In general, Lagrange's equation for a system with n degrees of freedom was

$$\frac{d}{dt}\frac{\partial}{\partial \dot{\theta}_i}T - \frac{\partial}{\partial \theta_i}T + \frac{\partial}{\partial \theta_i}U = \tau_i \quad , \quad i = 1, 2, \cdots, n \qquad \text{(AII.1)}$$

where T and U were the total kinetic and potential energy, respectively, and θ_i was the i'th generalized coordinate. Also, τ_i was the generalized applied torque corresponding to the i'th generalized coordinate θ_i, and n is the number of the generalized coordinates. Since the flexibilities of the joints were modeled as linear springs, the potential energy of the system due to the joint flexibilities became

$$U = \frac{1}{2}k_1(\theta_1 - \theta_3)^2 + \frac{1}{2}k_2(\theta_2 - \theta_4)^2 \qquad \text{(AII.2)}$$

where k_1 and k_2 represented the joint flexibilities. The kinetic energy of the system was the summation of the kinetic energy of links, T_l, the kinetic energy of payload mass, T_p, the kinetic

energy of rotors, T_r and the kinetic energy of hubs, T_h. Therefore,

$$T = T_l + T_p + T_r + T_h \qquad \text{(AII.3)}$$

where

$$T_l = \frac{1}{2}I_{l1}\dot{\theta}_1^2 + \frac{1}{2}m_{l1}L_{c1}^2 \cdot \dot{\theta}_1^2 + \frac{1}{2}I_{l2}\dot{\theta}_2^2 + \frac{1}{2}m_{l2}(L_1^2\dot{\theta}_1^2 + L_{c2}^2\dot{\theta}_2^2 + 2L_1L_{c2}\dot{\theta}_1\dot{\theta}_2\cos(\theta_2 - \theta_1)) \quad \text{(AII.4)}$$

$$T_p = \frac{1}{2}I_p\dot{\theta}_2^2 + \frac{1}{2}m_p(L_1^2\dot{\theta}_1^2 + L_2^2\dot{\theta}_2^2 + 2L_1L_2\dot{\theta}_1\dot{\theta}_2\cos(\theta_2 - \theta_1)) \qquad \text{(AII.5)}$$

$$T_r = \frac{1}{2}I_{r1}\dot{\theta}_3^2 + \frac{1}{2}I_{r2}\dot{\theta}_4^2 \qquad \text{(AII.6)}$$

$$T_h = \frac{1}{2}I_{h2}\dot{\theta}_1^2 + \frac{1}{2}m_{h2}L_1^2\dot{\theta}_1^2 \qquad \text{(AII.7)}$$

In equations (AII.4)-(AII.7), for $i = 1,2$, m_{l_i} is the mass of link i; m_p is the mass of the manipulator's tip; m_{h_i} is the mass of the hub i; L_i is the length of link i; L_{c_i} is the distance of the center of mass of link i from joint i axis. Parameters I_{l_i}, I_p, I_{h_i} and I_{r_i} are respectively mass moments of inertia of link i, manipulator's tip, hub of joint i, and rotor of joint i. Derivatives of the kinetic and potential energies of TRLFJ were determined as

$$\frac{d}{dt}\left(\frac{\partial T}{\partial \dot{\theta}_1}\right) = I_{l1}\ddot{\theta}_1 + m_{l1}L_{c1}^2\ddot{\theta}_1 + m_{l2}[L_1^2\ddot{\theta}_1 + L_1L_{c2}\ddot{\theta}_2\cos(\theta_2 - \theta_1) - L_1L_{c2}\dot{\theta}_2(\dot{\theta}_2 - \dot{\theta}_1)\sin(\theta_2 - \theta_1)]$$
$$+ m_p[L_1^2\ddot{\theta}_1 + L_1L_2\ddot{\theta}_2\cos(\theta_2 - \theta_1) - L_1L_2\dot{\theta}_2(\dot{\theta}_2 - \dot{\theta}_1)\sin(\theta_2 - \theta_1)] + I_{h2}\ddot{\theta}_1 + m_{h2}L_1^2\ddot{\theta}_1 \qquad \text{(AII.8)}$$

$$\frac{d}{dt}\left(\frac{\partial T}{\partial \dot{\theta}_2}\right) = I_{l2}\ddot{\theta}_2 + m_{l2}[L_{c2}^2\ddot{\theta}_2 + L_1L_{c2}\ddot{\theta}_1\cos(\theta_2 - \theta_1) - L_1L_{c2}\dot{\theta}_1(\dot{\theta}_2 - \dot{\theta}_1)\sin(\theta_2 - \theta_1)]$$
$$+ I_p\ddot{\theta}_2 + m_p[L_2^2\ddot{\theta}_2 + L_1L_2\ddot{\theta}_1\cos(\theta_2 - \theta_1) - L_1L_2\dot{\theta}_1(\dot{\theta}_2 - \dot{\theta}_1)\sin(\theta_2 - \theta_1)] \qquad \text{(AII.9)}$$

$$\frac{d}{dt}\left(\frac{\partial T}{\partial \dot{\theta}_3}\right) = I_{r1}\ddot{\theta}_3 \qquad \text{(AII.10)}$$

$$\frac{d}{dt}\left(\frac{\partial T}{\partial \dot{\theta}_4}\right) = I_{r2}\ddot{\theta}_4 \qquad \text{(AII.11)}$$

$$\frac{\partial T}{\partial \theta_1} = m_{l2}[L_1 L_{c2}\dot{\theta}_1\dot{\theta}_2 \sin(\theta_2 - \theta_1)] + m_p[L_1 L_2\dot{\theta}_1\dot{\theta}_2 \sin(\theta_2 - \theta_1)] \qquad \text{(AII.12)}$$

$$\frac{\partial T}{\partial \theta_2} = m_{l2}[-L_1 L_{c2}\dot{\theta}_1\dot{\theta}_2 \sin(\theta_2 - \theta_1)] + m_p[-L_1 L_2\dot{\theta}_1\dot{\theta}_2 \sin(\theta_2 - \theta_1)] \qquad \text{(AII.13)}$$

$$\frac{\partial T}{\partial \theta_3} = 0 \qquad \text{(AII.14)}$$

$$\frac{\partial T}{\partial \theta_4} = 0 \qquad \text{(AII.15)}$$

$$\frac{\partial}{\partial \theta_1} U = k_1(\theta_1 - \theta_3) \qquad \text{(AII.16)}$$

$$\frac{\partial}{\partial \theta_2} U = k_2(\theta_2 - \theta_4) \qquad \text{(AII.17)}$$

$$\frac{\partial}{\partial \theta_3} U = -k_1(\theta_1 - \theta_3) \qquad \text{(AII.18)}$$

$$\frac{\partial}{\partial \theta_4} U = -k_2(\theta_2 - \theta_4) \qquad \text{(AII.19)}$$

Combining equations (AII.8)-(AII.19) and (AII.1) led to the Lagrange's equations of the system

$$I_{l1}\ddot{\theta}_1 + m_{l1}L_{c1}{}^2\ddot{\theta}_1 + I_{l2}\ddot{\theta}_1 + m_{l2}[L_1{}^2\ddot{\theta}_1 + L_{c2}{}^2\ddot{\theta}_1 + L_1 L_{c2}\ddot{\theta}_2 \cos(\theta_2 - \theta_1) - L_1 L_{c2}\dot{\theta}_2{}^2 \sin(\theta_2 - \theta_1)]$$
$$+ I_p\ddot{\theta}_2 + m_p[L_1{}^2\ddot{\theta}_1 + L_2{}^2\ddot{\theta}_1 + L_1 L_2\ddot{\theta}_2 \cos(\theta_2 - \theta_1) - L_1 L_2\dot{\theta}_2 \sin(\theta_2 - \theta_1)] + I_{r2}\ddot{\theta}_4 + I_{h2}\ddot{\theta}_1 + \qquad \text{(AII.20)}$$
$$m_{h2}L_1{}^2\ddot{\theta}_1 + k_1(\theta_1 - \theta_3) = 0$$

$$I_{l2}\ddot{\theta}_2 + m_{l2}[L_{c2}{}^2\ddot{\theta}_2 + L_1 L_{c2}\ddot{\theta}_1 \cos(\theta_2 - \theta_1) + L_1 L_{c2}\dot{\theta}_1{}^2 \sin(\theta_2 - \theta_1)] + I_p\ddot{\theta}_2 +$$
$$m_p[L_2{}^2\ddot{\theta}_2 + L_1 L_2\ddot{\theta}_1 \cos(\theta_2 - \theta_1) + L_1 L_2\dot{\theta}_1{}^2 \sin(\theta_2 - \theta_1)] + k_2(\theta_2 - \theta_4) = 0 \qquad \text{(AII.21)}$$

$$I_{r1}\ddot{\theta}_3 - k_1(\theta_1 - \theta_3) = 0 \qquad \text{(AII.22)}$$

$$I_{r2}\ddot{\theta}_4 - k_2(\theta_2 - \theta_4) = 0 \tag{AII.23}$$

Equations (AII.20)-(AII.23) were then rewritten in the matrix form as

$$M(\overset{\theta.\theta}{~}) + C(\overset{\theta.\theta.\theta}{~,~}) + K = \tau \tag{AII.24}$$

where M, C and K represented the mass matrix, the centripetal and centrifugal matrix and the stiffness matrix, respectively. The 4×4 square matrices M, C and K matrices and 4×1 vector of applied torques τ were

$$M = \begin{bmatrix} M_{11} & M_{12} & 0 & 0 \\ M_{21} & M_{22} & 0 & 0 \\ 0 & 0 & I_{r1} & 0 \\ 0 & 0 & 0 & I_{r2} \end{bmatrix}, C = \begin{bmatrix} 0 & C_{12} & 0 & 0 \\ C_{21} & 0 & 0 & 0 \\ 0 & 0 & 0 & 0 \\ 0 & 0 & 0 & 0 \end{bmatrix}, K = \begin{bmatrix} k_1 & 0 & -k_1 & 0 \\ 0 & k_2 & 0 & -k_2 \\ -k_1 & 0 & k_1 & 0 \\ 0 & -k_2 & 0 & k_2 \end{bmatrix}, \tau = \begin{bmatrix} -\tau_2 \\ 0 \\ \tau_1 \\ \tau_2 \end{bmatrix}$$

where components of these matrices were

$$M_{11} = I_{l_1} + m_{l_1}L_{c_1}^2 + m_{l_2}L_1^2 + m_pL_1^2 + I_{h_2} + m_{h_2}L_1^2, \tag{AII.25}$$

$$M_{12} = m_{l_2}L_1L_{c_2}\cos(\theta_2 - \theta_1) + m_pL_1L_2\cos(\theta_2 - \theta_1), \tag{AII.26}$$

$$M_{21} = M_{12}, \tag{AII.27}$$

$$M_{22} = I_{l_2} + m_{l_2}L_{c_2}^2 + I_p + m_pL_2^2 \tag{AII.28}$$

$$C_{12} = -\left(m_{l_2}L_1L_{c_2} + m_pL_1L_2\right)\sin(\theta_2 - \theta_1)\dot{\theta}_2 \tag{AII.29}$$

$$C_{21} = \left(m_{l_2}L_1L_{c_2} + m_pL_1L_2\right)\sin(\theta_2 - \theta_1)\dot{\theta}_1 \tag{AII.30}$$

Some properties were noted about the dynamic equation of the system. First, the matrices M and C were functions of generalized coordinates θ_1 and θ_2, and their derivatives $\dot{\theta}_1$ and $\dot{\theta}_2$. Second, the matrices M and K were symmetric; that is $M_{ij} = M_{ji}$ and $K_{ij} = K_{ji}$ where $i = 1,2,3,4$.

AII.2. Simulation results for dynamic equations of TRLFJ

Exact dynamic modeling of the system was carried out using Matlab software. The dynamic equations of the system were solved using the Rung-Kutta method. The time step was fixed as $\Delta t = 0.0001\,\mathrm{sec}$. and the simulation was performed during two seconds and the constant torques were $\tau_1 = 0.3\,N.m$ and $\tau_2 = 0.1\,N.m$. Both links similarly had $0.5\,m$ length, cross section $0.01 \times 0.01\,m^2$ and density $7800\,kg/m^3$. The payload mass and the payload inertia were $0.2\,kg$ and $0.001\,kg.m^2$. The inertias of the rotors of both motors were $0.001\,kg.m^2$ and inertias of the stators of both motors were $0.0003\,kg.m^2$. Also, the spring constants were selected as $k_1 = k_2 = 30\,N.m/rad$.

The developed dynamic model based on the Lagrage's method (LM model) was verified using ANSYS finite element analysis software. Links were modeled by 3-DOF element "Beam3". The mass and inertias were modeled using 6-DOF element "Mass21". To model the torsional springs, 1-DOF element "Combin14" was used. The elasticity module was set to $E = 210 \times 10^{12}\,Pa$ (1000 times stiffer than steel) in order to have the rigid links. The rotations of links as well as rotations of motors are shown in Figs. AII.1-AII.4. According to these figures, the results obtained using Lagrange's method (LM) were found to be in good agreements with the results of FEA.
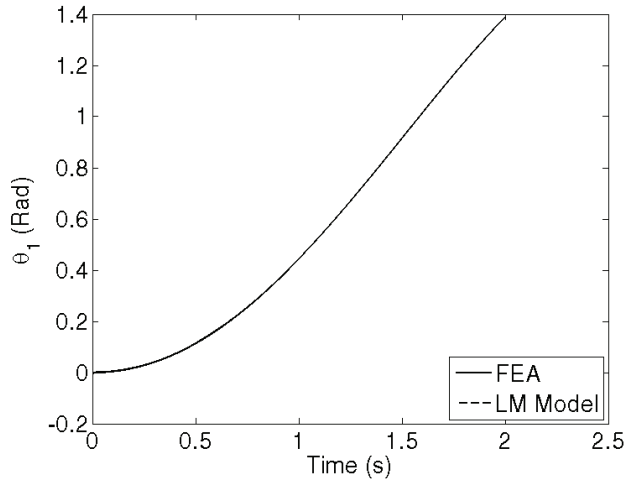
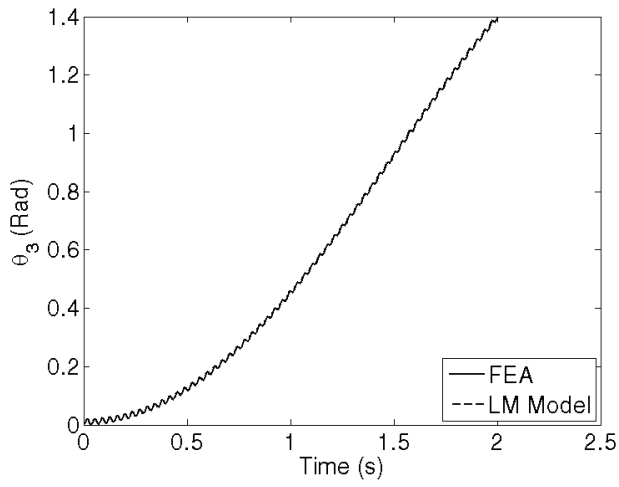Figure AII.1. Rotation of the shoulder link of TRLFJ

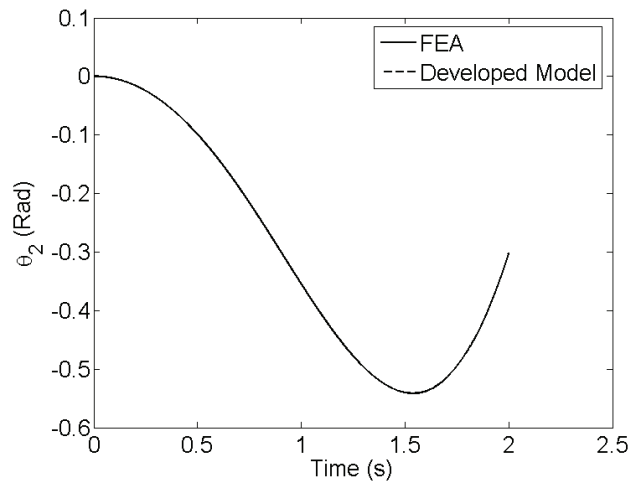Figure AII.2. Rotation of the shoulder motor of TRLFJ

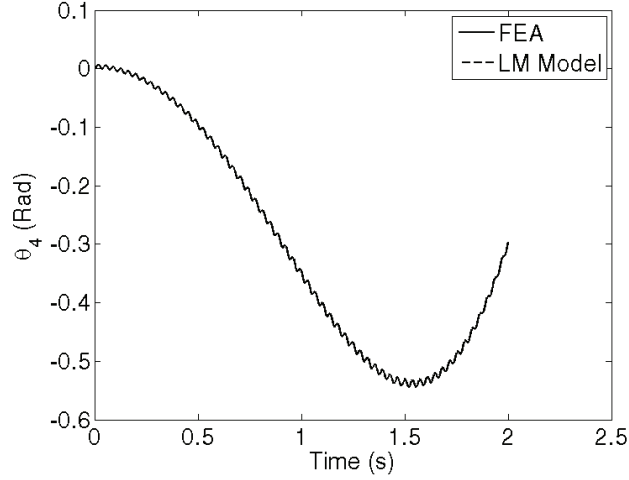Figure AII.3. Rotation of the elbow link of TRLFJ

168

Figure AII.4. Rotation of the elbow joint of TRLFJ

AII.3. Dynamic modelling of TFLFJ

For the dynamic modeling of two-flexible-link flexible-joint (TFLFJ), a combination of the Lagrange's method and assumed mode shapes method (LAMM) was employed. The modeling procedure was similar to the one that was used in the previous section for the TRLFJ. However, for TFLFJ, eight degrees of freedom contributed to the dynamics of the system. Based on the assumed mode shapes method, the deflection of each link was modeled using two clamped-free mode shapes. Therefore, four DOF represented the flexibility of two links. Also, two DOF's (θ_1, θ_2) were related to the rotations of the links, and other two DOF's (θ_3, θ_4) represented the rotations of rotors.

To employ the Lagrange's equations, the kinetic and potential energies were first derived for the links, payload mass, hubs and rotors. According to equation (1) in Chapter 6, the velocity of an arbitrary point along the first link of the manipulator, $\bar{V}_p^{(1)}$, was written as

$$\bar{V}_p^{(1)} = \bar{V}_o^{(1)} + \bar{\omega}_1 \times \bar{r}_1 + \bar{V}_{rel}^{(1)} \qquad (AII.31)$$

For the first link, velocity of the coordinate system (x_1, y_1) was zero (See Fig. AII.5); that is $\bar{V}_o^{(1)} = 0$, and the angular velocity of (x_1, y_1) was $\bar{\omega}_1 = \dot{\theta}_1 \hat{k}$. The vector $\bar{r}_1$, which indicated the

169

coordinates of point p_1, was $\bar{r}_1 = x_{p1}\hat{\imath} + y_{p1}\hat{\jmath}$, and the relative velocity of point p_1 with respect

to the coordinate system (x_1, y_1) was $\bar{V}_{rel}^{(1)} = \dot{y}_{p1}\hat{\jmath}$. After substituting these parameters in

(AII.31), the velocity of point p_1 was determined as

$$\bar{V}_p^{(1)} = (\dot{y}_{p1} + x_{p1}\dot{\theta}_1)\hat{\jmath} + (-y_{p1}\dot{\theta}_1)\hat{\imath} \tag{AII.32}$$
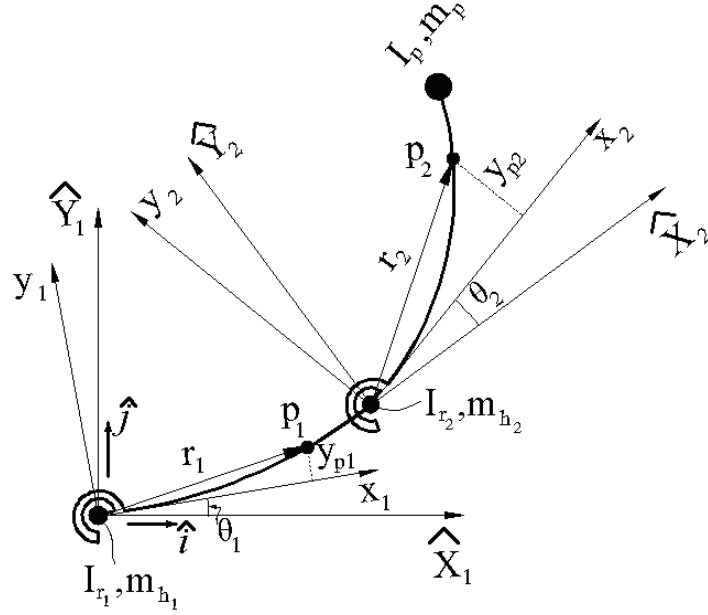

Figure AII.5. Schematic of TFLFJ

The velocity of an arbitrary point p_2 along the second link of the manipulator was

similarly identified as

$$\bar{V}_p^{(2)} = \bar{V}_o^{(2)} + \bar{\omega}_2 \times \bar{r}_2 + \bar{V}_{rel}^{(2)} \tag{AII.33}$$

The terms in the right-hand side of (AII.33) were

$$\bar{V}_o^{(2)} = \begin{bmatrix} 1 & -y'_{p1}(l_1) \\ y'_{p1}(l_1) & 1 \end{bmatrix} \begin{bmatrix} \cos\theta_2 & -\sin\theta_2 \\ \sin\theta_2 & \cos\theta_2 \end{bmatrix} \begin{bmatrix} y_{p1}\dot{\theta}_1 \\ \dot{y}_{p1}(l_1) + l_1\dot{\theta}_1 \end{bmatrix} \tag{AII.34}$$

$$\bar{\omega}_2 = \left[\dot{\theta}_1 + \left(\frac{\partial \dot{y}_{p1}}{\partial x}\right)_{x_1 = l_1} + \dot{\theta}_2\right]\hat{k} \tag{AII.35}$$

$$\bar{r}_2 = x_{p2}\hat{\imath} + y_{p2}\hat{\jmath} \tag{AII.36}$$

170

$$\bar{V}_{rel}^{(2)} = \dot{y}_{p2}\hat{j} \tag{AII.37}$$

where $y'_{p1}(l_1)$ is the derivative of the deflection of first link with respect to x_1, and is measured at $x_1 = l_1$. Substituting (AII.34)-(AII.37) into (AII.33) led to

$$\bar{V}_p^{(2)} = \bar{V}_{p_x}^{(2)}\hat{i} + \bar{V}_{p_y}^{(2)}\hat{j} \tag{AII.38}$$

where

$$\bar{V}_{p_x}^{(2)} = y_{p1}(l_1)\dot{\theta}_1\big[y'_{p1}(l_1)(\sin\theta_2 - \cos\theta_2) - (\sin\theta_2 + \cos\theta_2)\big] + \dot{y}_{p1}(l_1)\big[-y'_{p1}(l_1)\cos\theta_2 - $$
$$\sin\theta_2\big] - y_{p2}\big[\dot{\theta}_1 + \dot{y}_{p1}(l_1) + \dot{\theta}_2\big] \tag{AII.39}$$

$$\bar{V}_{p_y}^{(2)} = -y_{p1}(l_1)\dot{\theta}_1\big[-y'_{p1}(l_1)(\sin\theta_2 + \cos\theta_2) - (\sin\theta_2 - \cos\theta_2)\big] + \dot{y}_{p1}(l_1)\big[-y'_{p1}(l_1)\cos\theta_2 + $$
$$\sin\theta_2\big] + \dot{y}_{p2} + x_{p2}\big[\dot{\theta}_1 + \dot{y}_{p1}(l_1) + \dot{\theta}_2\big] \tag{AII.40}$$

The kinetic energy of the links was obtained by substituting velocity of the second link, equations (AII.39) and (AII.40), and velocity of the first link, equation (AII.37) into equation (8) in Chapter 6. That is,

$$T_l = \frac{1}{2}\int_0^{l_1} \rho_1\left\{\big[-y_{p1}\dot{\theta}_1\big]^2 + \big[\dot{y}_{p1} + x_{p1}\dot{\theta}_1\big]^2\right\}^{1/2} dx + \frac{1}{2}\int_0^{l_2} \rho_2\left\{\Big[y_{p1}(l_1)\dot{\theta}_1\big[y'_{p1}(l_1)(\sin\theta_2 - \right.$$

$$\cos\theta_2) - (\sin\theta_2 + \cos\theta_2)\big] + \dot{y}_{p1}(l_1)\big[-y'_{p1}(l_1)\cos\theta_2 - \sin\theta_2\big] - y_{p2}\big[\dot{\theta}_1 + \dot{y}_{p1}(l_1) + \dot{\theta}_2\big]\Big]^2 + $$

$$\Big[-y_{p1}(l_1)\dot{\theta}_1\big[-y'_{p1}(l_1)(\sin\theta_2 + \cos\theta_2) - (\sin\theta_2 - \cos\theta_2)\big] + \dot{y}_{p1}(l_1)\big[-y'_{p1}(l_1)\cos\theta_2 + $$

$$\left. \sin\theta_2\big] + \dot{y}_{p2} + x_{p2}\big[\dot{\theta}_1 + \dot{y}_{p1}(l_1) + \dot{\theta}_2\big]\Big]^2\right\}^{1/2} dx \tag{AII.41}$$

Other terms of the kinetics energy were determined from equations (5)-(7) in Chapter 6. Also, the potential energy was found using equation (9) in Chapter 6; that is,

$$U = \frac{1}{2}\int_0^{l_1}(EI)_1\left[\frac{d^2 y_{p1}(x_{p1})}{dx_{p1}^2}\right]^2 dx + \frac{1}{2}\int_0^{l_2}(EI)_2\left[\frac{d^2 y_{p2}(x_{p2})}{dx_{p2}^2}\right]^2 dx + \frac{1}{2}k_1(\theta_1 - \alpha_1)^2 + \frac{1}{2}k_2(\theta_2 - \alpha_2)^2$$

$$\tag{AII.42}$$

where α_1 and α_2 are the rotations of shoulder and elbow joints, respectively. The Lagrange's equations were then used to obtain the general form of the dynamic equations for TFLFJ. The components of matrices M, C, and K are given in the following in the MATLAB code written by the candidate. In this program, the physical properties of the shoulder and elbow links, tip-mass and the joints were identified in the first part, and the components of the matrices were defined in the next part of the code. This code was employed in a Simulink file for the simulation of the dynamics of TFLFJ manipulator. The schematic of the Simulink file is shown in Figs. AII.5 and AII.6.

```matlab
%This program solves the dynamics of two flexible link-flexible joint
%two mode shapes are considered for each link and Lagrange method was used,
% this system has 8 degrees of freedom: q(1):first link rotation,
% q(2):second link rotation, q(3),q(4) represent the deflection of the
% first link (two mode shapes) and q(5),q(6) represent the deflection of the
% second link (two mode shapes),q(7) and q(8) represent the rotation of the
% motors.

function y=two_FLFJ_sym(q);
clc

% Physical properties of the shoulder link
l(1)=0.5;
ru(1)=8000;
thick(1)=2e-3;
width(1)=2.5e-2;
mh(1)=0;
Ir(1)=0.01;
% Physical properties of the elbow link
l(2)=0.5;
ru(2)=8000;
thick(2)=2e-3;
width(2)=2.5e-2;
mh(2)=0.5;
Ih(2)=0;
Ir(2)=0.01;
% Specifications of the tip-mass
mp=0.1;
Ip=5e-4;

d=0.5*l;
A=width.*thick;
I=(1/12).*width.*thick.^3;
ml=l.*ru.*A;
Il=(1/3).*ml.*l.^2;
ro=ru.*A;

% Specifications of the joint flexibities
k(1)=20;
k(2)=20;

freqs_link=[1.2220 4.5214;3.6762 24.8624];
v=[0.0259 0.0413;0.0840 0.1186];
w=[0.0096 0.0138;0.0307 0.0323];
Phi=[0.3695 0.2971;1.1366 -0.2776];
Phi_d=[1.2476 -1.4762;3.3582 -12.8776];

%%%%%%%%%%%%%%%%%%%%%%%%%%%%%%%%%%%%%%%%%%%%%%%%%%%%%%%%%
%%%%%%%%%%%%%%%%%%%%%%%%%%%%%%%
% Assembling of matrices
%%%%%%%%%%%%%%%%%%%%%%%%%%%%%%%%%%%%%%%%%%%%%%%%%%%%%%%%%%%%%%
%%%%%%%%%%%%%%%%%%%%%%%%%%%%%%
% t components
```

```
t11=Phi(1,1)-l(1)*Phi_d(1,1);
t12=Phi(1,2)-l(1)*Phi_d(1,2);
t21=v(2,1)+mp*Phi(2,1);
t22=v(2,2)+mp*Phi(2,2);
t31=Phi_d(1,1);
t32=Phi_d(1,2);


t1=t11*q(3)+t12*q(4);
t2=t21*q(5)+t22*q(6);
t3=t31*q(3)+t32*q(4);
```

% b components
```
b111=Ih(2)+Ir(2)+Il(1)+Il(2)+mh(2)*l(1)^2+ml(2)*l(1)^2+Ip+mp*(l(1)^2+l(2)^2);
b112=2*(ml(2)*d(2)+mp*l(2))*l(1);
b113=2*(ml(2)*d(2)+mp*l(2));
b114=-2*l(1);


b121=Il(2)+Ip+mp*l(2)^2;
b122=(ml(2)*d(2)+mp*l(2))*l(1);
b123=ml(2)*d(2)+mp*l(2);
b124=-l(1);


b131=w(1,1)+(Ih(2)+Ir(2)+Il(2)+Ip+mp*l(2)^2)*Phi_d(1,1)+(mh(2)+ml(2)+mp)*l(1)*Phi(1,1);
b132=(ml(2)*d(2)+mp*l(2))*(Phi(1,1)+l(1)*Phi_d(1,1));
b133=-(Phi(1,1)+l(1)*Phi_d(1,1));
b134=-(ml(2)*d(2)+mp*l(2))*(Phi(1,1)*Phi_d(1,2)-Phi(1,2)*Phi_d(1,1));


b141=w(1,2)+(Ih(2)+Ir(2)+Il(2)+Ip+mp*l(2)^2)*Phi_d(1,2)+(mh(2)+ml(2)+mp)*l(1)*Phi(1,2);
b142=(ml(2)*d(2)+mp*l(2))*(Phi(1,2)+l(1)*Phi_d(1,2));
b143=-(Phi(1,2)+l(1)*Phi_d(1,2));
b144=-(ml(2)*d(2)+mp*l(2))*(Phi(1,2)*Phi_d(1,1)-Phi(1,1)*Phi_d(1,2));


b151=w(2,1)+Ip*Phi_d(2,1)+mp*l(2)*Phi(2,1);
b152=(v(2,1)+mp*Phi(2,1))*l(1);
b153=v(2,1)+mp*Phi(2,1);


b161=w(2,2)+Ip*Phi_d(2,2)+mp*l(2)*Phi(2,2);
b162=(v(2,2)+mp*Phi(2,2))*l(1);
b163=v(2,2)+mp*Phi(2,2);


b181=Ir(2);


b221=Il(2)+Ip+mp*l(2)^2;
b231=(Il(2)+Ip+mp*l(2)^2)*Phi_d(1,1);
b232=(ml(2)*d(2)+mp*l(2))*Phi(1,1);
b233=-Phi(1,1);
b234=-(ml(2)*d(2)+mp*l(2))*Phi(1,1);


b241=(Il(2)+Ip+mp*l(2)^2)*Phi_d(1,2);
b242=(ml(2)*d(2)+mp*l(2))*Phi(1,2);
b243=-Phi(1,2);
b244=-(ml(2)*d(2)+mp*l(2))*Phi(1,2);


b251=w(2,1)+Ip*Phi_d(2,1)+mp*l(2)*Phi(2,1);
```

174

```matlab
b261=w(2,2)+Ip*Phi_d(2,2)+mp*l(2)*Phi(2,2);

b331=ml(1);
b332=2*(ml(2)*d(2)+mp*l(2))*Phi(1,1)*Phi_d(1,1);
b333=-2*Phi(1,1)*Phi_d(1,1);
b341=0;
b342=(ml(2)*d(2)+mp*l(2))*(Phi(1,1)*Phi_d(1,2)+Phi(1,2)*Phi_d(1,1));
b343=-(Phi(1,1)*Phi_d(1,2)+Phi(1,2)*Phi_d(1,1));
b351=(w(2,1)+Ip*Phi_d(2,1)+mp*l(2)*Phi(2,1))*Phi_d(1,1);
b352=(v(2,1)+mp*Phi(2,1))*Phi(1,1);
b353=-(v(2,1)+mp*Phi(2,1))*Phi(1,1);
b361=(w(2,2)+Ip*Phi_d(2,2)+mp*l(2)*Phi(2,2))*Phi_d(1,1);
b362=(v(2,2)+mp*Phi(2,2))*Phi(1,1);
b363=-(v(2,2)+mp*Phi(2,2))*Phi(1,1);
b381=Ir(2)*Phi_d(1,1);               % Added terms

b441=ml(1);
b442=2*(ml(2)*d(2)+mp*l(2))*Phi(1,2)*Phi_d(1,2);
b443=-2*Phi(1,2)*Phi_d(1,2);
b451=(w(2,1)+Ip*Phi_d(2,1)+mp*l(2)*Phi(2,1))*Phi_d(1,2);
b452=(v(2,1)+mp*Phi(2,1))*Phi(1,2);
b453=-(v(2,1)+mp*Phi(2,1))*Phi(1,2);
b461=(w(2,2)+Ip*Phi_d(2,2)+mp*l(2)*Phi(2,2))*Phi_d(1,2);
b462=(v(2,2)+mp*Phi(2,2))*Phi(1,2);
b463=-(v(2,2)+mp*Phi(2,2))*Phi(1,2);
b481=Ir(2)*Phi_d(1,2);               % Added terms

b551=ml(2);
b561=0;
b661=ml(2);
%%%%%%%%%%%%%%%%%%%%%%%%%%%%%%%%%%%%%%%%%%%%%%%%%%%%%%%%%
%%%%%%%%%%%%%%%%%%%%%%%%%%%%%
% h components
h101=-2*(ml(2)*d(2)+mp*l(2))*l(1);
h102=2*(ml(2)*d(2)+mp*l(2))*(Phi(1,1)-l(1)*Phi_d(1,1));
h103=2*(ml(2)*d(2)+mp*l(2))*(Phi(1,2)-l(1)*Phi_d(1,2));
h104=-2*(v(2,1)+mp*Phi(2,1))*l(1);
h105=-2*(v(2,2)+mp*Phi(2,2))*l(1);
h106=-(ml(2)*d(2)+mp*l(2))*l(1);
h107=-(ml(2)*d(2)+mp*l(2))*l(1)*Phi_d(1,1);  %%%My comment
h108=-2*(ml(2)*d(2)+mp*l(2))*l(1)*Phi_d(1,2);
h109=-2*(v(2,1)+mp*Phi(2,1))*l(1);
h110=-2*(v(2,2)+mp*Phi(2,2))*l(1);
h111=-2*(v(2,1)+mp*Phi(2,1))*l(1)*Phi_d(1,1);
h112=-2*(v(2,2)+mp*Phi(2,2))*l(1)*Phi_d(1,1);
h113=-2*(v(2,1)+mp*Phi(2,1))*l(1)*Phi_d(1,2);
h114=-2*(v(2,2)+mp*Phi(2,2))*l(1)*Phi_d(1,2);
h115=2*(ml(2)*d(2)+mp*l(2));
h116=ml(2)*d(2)+mp*l(2);
h117=-(v(2,1)+mp*Phi(2,1));
h118=-(v(2,2)+mp*Phi(2,2));
h119=-2*l(1);
h120=-l(1);
h121=-(Phi(1,1)+l(1)*Phi_d(1,1));
h122=-(Phi(1,2)+l(1)*Phi_d(1,2));
```

```
h123=-(ml(2)*d(2)+mp*l(2))*(Phi(1,1)*Phi_d(1,2)-Phi(1,2)*Phi_d(1,1));
h124=-(ml(2)*d(2)+mp*l(2))*(Phi(1,2)*Phi_d(1,1)-Phi(1,1)*Phi_d(1,2));


h201=(ml(2)*d(2)+mp*l(2))*l(1);
h202=2*(ml(2)*d(2)+mp*l(2))*Phi(1,1);
h203=2*(ml(2)*d(2)+mp*l(2))*Phi(1,2);
h204=-(ml(2)*d(2)+mp*l(2));
h205=-(v(2,1)+mp*Phi(2,1));
h206=-(v(2,2)+mp*Phi(2,2));
h207=l(1);
h208=Phi(1,1)+l(1)*Phi_d(1,1);
h209=Phi(1,2)+l(1)*Phi_d(1,2);
h210=(ml(2)*d(2)+mp*l(2))*(Phi(1,1)*Phi_d(1,2)-Phi(1,2)*Phi_d(1,1));
h211=(ml(2)*d(2)+mp*l(2))*(Phi(1,2)*Phi_d(1,1)-Phi(1,1)*Phi_d(1,2));
h212=Phi(1,1)*Phi_d(1,1);
h213=Phi(1,1)*Phi_d(1,2)+Phi(1,2)*Phi_d(1,1);
h214=(v(2,1)+mp*Phi(2,1))*Phi(1,1);
h215=(v(2,2)+mp*Phi(2,2))*Phi(1,1);
h216=Phi(1,2)*Phi_d(1,2);
h217=(v(2,1)+mp*Phi(2,1))*Phi(1,2);
h218=(v(2,2)+mp*Phi(2,2))*Phi(1,2);


h301=-(ml(2)*d(2)+mp*l(2))*(Phi(1,1)-l(1)*Phi_d(1,1));
h302=-2*(ml(2)*d(2)+mp*l(2))*Phi(1,1);
h303=2*(ml(2)*d(2)+mp*l(2))*(Phi(1,2)*Phi_d(1,1)-Phi(1,1)*Phi_d(1,2));
h304=-2*(v(2,1)+mp*Phi(2,1))*Phi(1,1);
h305=-2*(v(2,2)+mp*Phi(2,2))*Phi(1,1);
h306=-(ml(2)*d(2)+mp*l(2))*Phi(1,1);
h307=-2*(ml(2)*d(2)+mp*l(2))*Phi(1,1)*Phi_d(1,1);
h308=-2*(ml(2)*d(2)+mp*l(2))*Phi(1,1)*Phi_d(1,2);
h309=-2*(v(2,1)+mp*Phi(2,1))*Phi(1,1);
h310=-2*(v(2,2)+mp*Phi(2,2))*Phi(1,1);
h311=-2*(v(2,1)+mp*Phi(2,1))*Phi(1,1)*Phi_d(1,1);
h312=-2*(v(2,2)+mp*Phi(2,2))*Phi(1,1)*Phi_d(1,1);
h313=-2*(v(2,1)+mp*Phi(2,1))*Phi(1,1)*Phi_d(1,2);
h314=-2*(v(2,2)+mp*Phi(2,2))*Phi(1,1)*Phi_d(1,2);
h315=-(Phi(1,1)+l(1)*Phi_d(1,1));
h316=-Phi(1,1);
h317=-2*Phi(1,1)*Phi_d(1,1);
h318=-(Phi(1,1)*Phi_d(1,2)+Phi(1,2)*Phi_d(1,1));
h319=-(ml(2)*d(2)+mp*l(2))*Phi(1,1);
h320=-(v(2,1)+mp*Phi(2,1))*Phi(1,1);
h321=-(v(2,2)+mp*Phi(2,2))*Phi(1,1);
h322=-(ml(2)*d(2)+mp*l(2))*(Phi(1,1)*Phi_d(1,2)-Phi(1,2)*Phi_d(1,1));


h401=-(ml(2)*d(2)+mp*l(2))*(Phi(1,2)-l(1)*Phi_d(1,2));
h402=-2*(ml(2)*d(2)+mp*l(2))*Phi(1,2);
h403=2*(ml(2)*d(2)+mp*l(2))*(Phi(1,1)*Phi_d(1,2)-Phi(1,2)*Phi_d(1,1));
h404=-2*(v(2,1)+mp*Phi(2,1))*Phi(1,2);
h405=-2*(v(2,2)+mp*Phi(2,2))*Phi(1,2);
h406=-(ml(2)*d(2)+mp*l(2))*Phi(1,2);
h407=-2*(ml(2)*d(2)+mp*l(2))*Phi(1,2)*Phi_d(1,1);
h408=-2*(ml(2)*d(2)+mp*l(2))*Phi(1,2)*Phi_d(1,2);
h409=-2*(v(2,1)+mp*Phi(2,1))*Phi(1,2);
h410=-2*(v(2,2)+mp*Phi(2,2))*Phi(1,2);
```

```
h411=-2*(v(2,1)+mp*Phi(2,1))*Phi(1,2)*Phi_d(1,1);
h412=-2*(v(2,2)+mp*Phi(2,2))*Phi(1,2)*Phi_d(1,2);
h413=-2*(v(2,1)+mp*Phi(2,1))*Phi(1,2)*Phi_d(1,1);
h414=-2*(v(2,2)+mp*Phi(2,2))*Phi(1,2)*Phi_d(1,2);
h415=-(Phi(1,2)+l(1)*Phi_d(1,2));
h416=-Phi(1,2);
h417=-(Phi(1,1)*Phi_d(1,2)+Phi(1,2)*Phi_d(1,1));
h418=-2*Phi(1,2)*Phi_d(1,2);
h419=-(ml(2)*d(2)+mp*l(2))*Phi(1,2);
h420=-(v(2,1)+mp*Phi(2,1))*Phi(1,2);
h421=-(v(2,2)+mp*Phi(2,2))*Phi(1,2);
h422=-(ml(2)*d(2)+mp*l(2))*(Phi(1,2)*Phi_d(1,1)-Phi(1,1)*Phi_d(1,2));


h501=(v(2,1)+mp*Phi(2,1))*l(1);
h502=2*(v(2,1)+mp*Phi(2,1))*Phi(1,1);
h503=2*(v(2,1)+mp*Phi(2,1))*Phi(1,2);
h504=v(2,1)+mp*Phi(2,1);
h505=-(v(2,1)+mp*Phi(2,1))*Phi(1,1);
h506=-(v(2,1)+mp*Phi(2,1))*Phi(1,2);


h601=(v(2,2)+mp*Phi(2,2))*l(1);
h602=2*(v(2,2)+mp*Phi(2,2))*Phi(1,1);
h603=2*(v(2,2)+mp*Phi(2,2))*Phi(1,2);
h604=v(2,2)+mp*Phi(2,2);
h605=-(v(2,2)+mp*Phi(2,2))*Phi(1,1);
h606=-(v(2,2)+mp*Phi(2,2))*Phi(1,2);


%%%%%%%%%%%%%%%%%%%%%%%%%%%%%%%%%%%%%%%%%%%%%%%%%%%%%%%%%%%%%%
%%%%%%%%%%%%%%%%%%%%%%%%%%%%%%%%
% Mass matrix
c=cos(q(2));
s=sin(q(2));

M=zeros(8,8);
M(1,1)=b111+b112*c+(b113*t1+b114*t2)*s;
M(1,2)=b121+b122*c+(b123*t1+b124*t2)*s;
M(1,3)=b131+b132*c+(b133*t2+b134*q(4))*s;
M(1,4)=b141+b142*c+(b143*t2+b144*q(3))*s;
M(1,5)=b151+b152*c+b153*t1*s;
M(1,6)=b161+b162*c+b163*t1*s;
M(1,8)=b181;

M(2,2)=b221;
M(2,3)=b231+b232*c+(b233*t2+b234*t3)*s;
M(2,4)=b241+b242*c+(b243*t2+b244*t3)*s;
M(2,5)=b251;
M(2,6)=b261;

M(3,3)=b331+b332*c+b333*t2*s;
M(3,4)=b341+b342*c+b343*t2*s;
M(3,5)=b351+b352*c+b353*t3*s;
M(3,6)=b361+b362*c+b363*t3*s;
M(3,8)=b381;
```

```matlab
M(4,4)=b441+b442*c+b443*t2*s;
M(4,5)=b451+b452*c+b453*t3*s;
M(4,6)=b461+b462*c+b463*t3*s;
M(4,8)=b481;

M(5,5)=b551;
M(5,6)=b561;

M(6,6)=b661;
M(7,7)=Ir(1);    %1st Rotor

M(8,8)=Ir(2);    %2nd Rotor
for j=8:-1:1
    for i=1:8
        M(j,i)=M(i,j);
    end
end

% H matrix

H(1)=((h101*q(10)+h102*q(11)+h103*q(12)+h104*q(13)+h105*q(14))*q(9)+...
    (h106*q(10)+h107*q(11)+h108*q(12)+h109*q(13)+h110*q(14))*q(10)+...
    (h111*q(13)+h112*q(14))*q(11)+(h113*q(13)+h114*q(14))*q(12))*s+...
    ((h115*q(9)+h116*q(10)+h117*q(13)+h118*q(14))*t1+...
    (h119*q(9)+h120*q(10)+h121*q(11)+h122*q(12))*t2+...
    h123*q(4)*q(11)+h124*q(3)*q(12))*q(10)*c;
H(2)=(h201*q(9)+h202*q(11)+h203*q(12))*q(9)*s+...
    (((h204*q(9)+h205*q(13)+h206*q(14))*t1+...
    (h207*q(9)+h208*q(11)+h209*q(12))*t2+...
    h210*q(4)*q(11)+h211*q(3)*q(12))*q(9)+...
    ((h212*q(11)+h213*q(12))*t2+(h214*q(13)+h215*q(14))*t3)*q(11)+...
    (h216*q(12)*t2+(h217*q(13)+h218*q(14))*t3)*q(12))*c;
H(3)=((h301*q(9)+h302*q(10)+h303*q(12)+h304*q(13)+h305*q(14))*q(9)+...
    (h306*q(10)+h307*q(11)+h308*q(12)+h309*q(13)+h310*q(14))*q(10)+...
    (h311*q(13)+h312*q(14))*q(11)+(h313*q(13)+h314*q(14))*q(12))*s+...
    ((h315*q(9)+h316*q(10)+h317*q(11)+h318*q(12))*t2+...
    (h319*q(10)+h320*q(13)+h321*q(14))*t3+...
    h322*q(4)*q(9))*q(10)*c;
H(4)=((h401*q(9)+h402*q(10)+h403*q(11)+h404*q(13)+h405*q(14))*q(9)+...
    (h406*q(10)+h407*q(11)+h408*q(12)+h409*q(13)+h410*q(14))*q(10)+...
    (h411*q(13)+h412*q(14))*q(11)+(h413*q(13)+h414*q(14))*q(12))*s+...
    ((h415*q(9)+h416*q(10)+h417*q(11)+h418*q(12))*t2+...
    (h419*q(10)+h420*q(13)+h421*q(14))*t3+...
    h422*q(3)*q(9))*q(10)*c;
H(5)=(h501*q(9)+h502*q(11)+h503*q(12))*q(9)*s+...
    (h504*t1*q(9)+(h505*q(11)+h506*q(12))*t3)*q(10)*c;
H(6)=(h601*q(9)+h602*q(11)+h603*q(12))*q(9)*s+...
    (h604*t1*q(9)+(h605*q(11)+h606*q(12))*t3)*q(10)*c;
H(7)=0;
H(8)=0;

K=zeros(8,8);
Wn=2*pi*freqs_link;
```

```
K(1,1)=k(1);
K(1,7)=-k(1);
K(2,2)=k(2);
K(2,8)=-k(2);
K(3,3)=Wn(1,1)^2*ml(1);
K(4,4)=Wn(1,2)^2*ml(1);
K(5,5)=Wn(2,1)^2*ml(2);
K(6,6)=Wn(2,2)^2*ml(2);
K(7,1)=-k(1);
K(7,7)=k(1);
K(8,2)=-k(2);
K(8,8)=k(2);

U=zeros(8,1);
U(7,1)=q(17);
U(8,1)=q(18);
%H;
%M;
%Eig=eig(M);
H=H';
y=inv(M)*(U-H-K*[q(1);q(2);q(3);q(4);q(5);q(6);q(7);q(8)]);
```
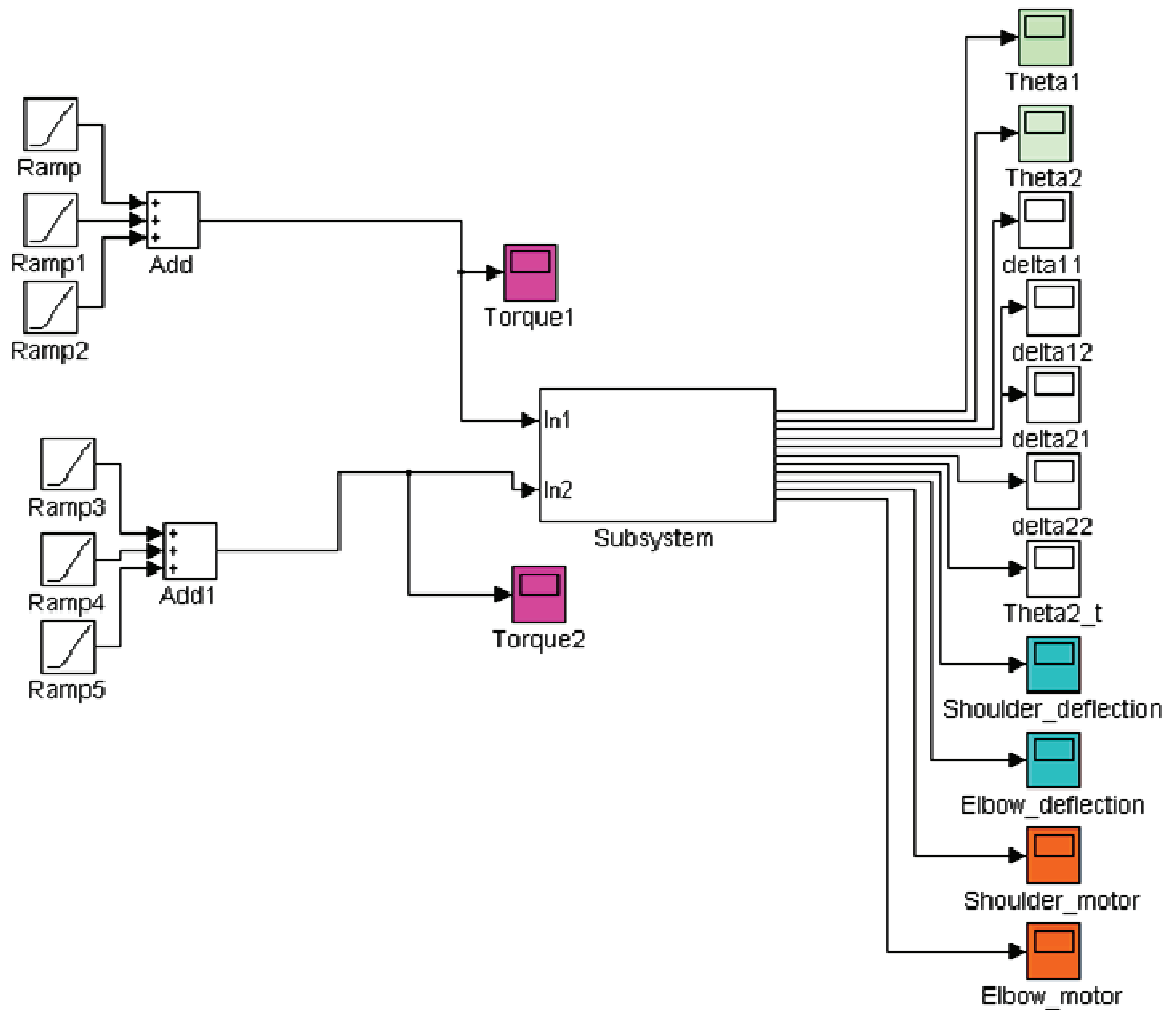
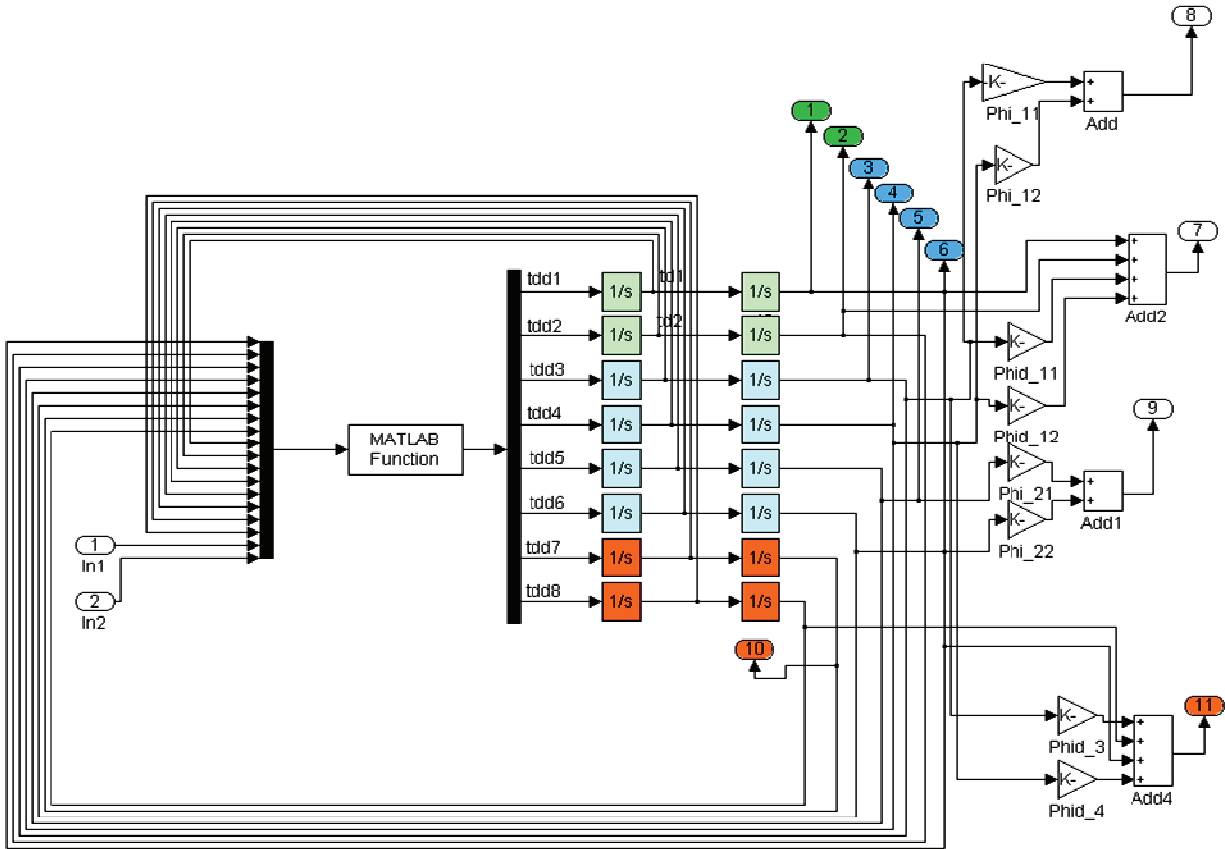Figure AII.6. Schematic of the Simulink file used for the dynamic modeling of TFLFJ

Figure AII.7. Details of the subsystem shown in Fig. AII.6

The developed dynamic model for TFLFJ was then verified with finite element analysis (FEA). Figures AII.8-AII.11 compare the simulation results of LAMM with FEA for the rotations of the joints and links. The deflection observed at the end of the shoulder link is also compared in Fig. AII.12. According to these figures, the results obtained using FEA confirm LAMM approach.
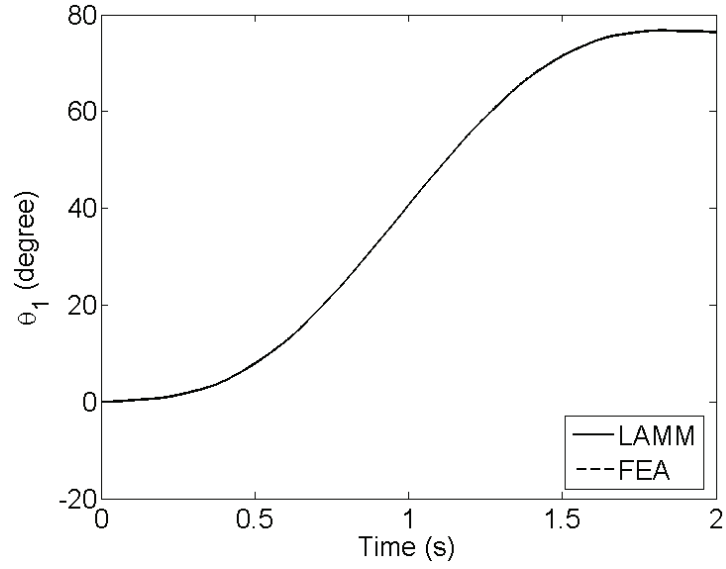
Figure AII.8. Rotation of the shoulder joint of TFLFJ
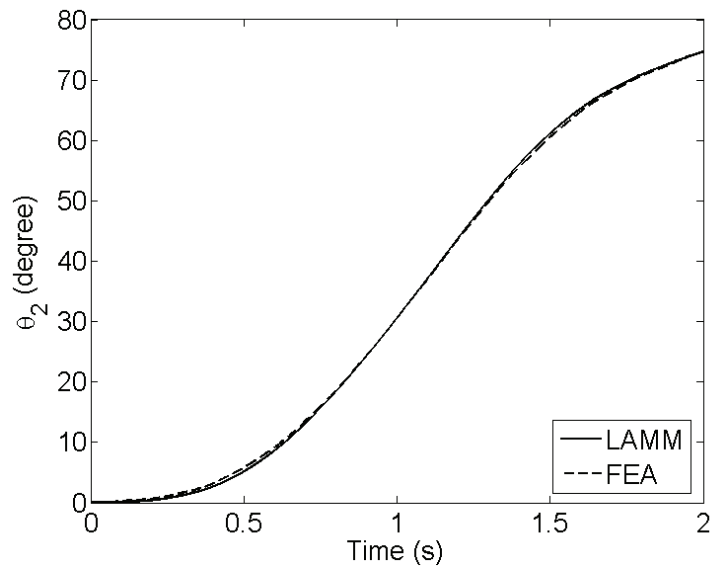
Figure AII.9. Rotation of the elbow joint of TFLFJ
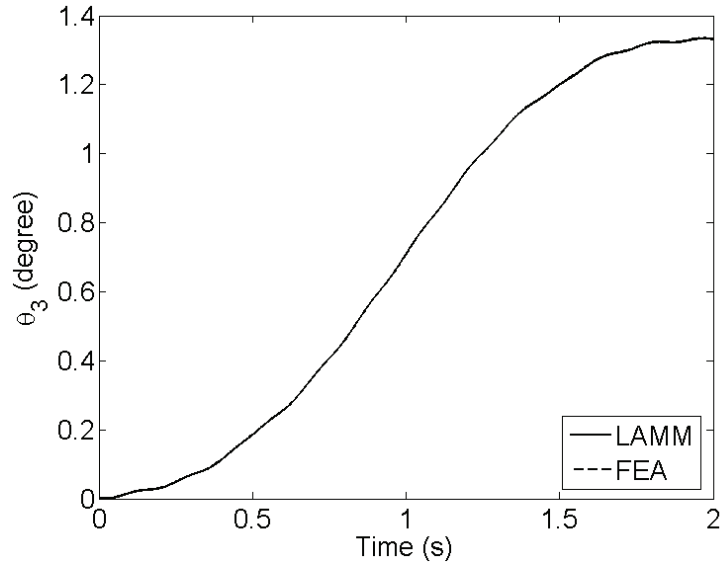
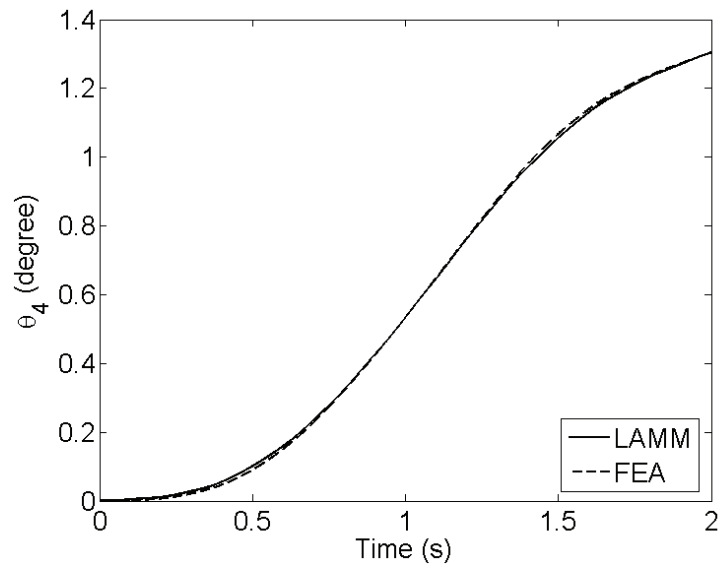Figure AII.10. Slope of the shoulder link at shoulder joint for TFLFJ

Figure AII.11. Slope of the elbow link at elbow joint for TFLFJ
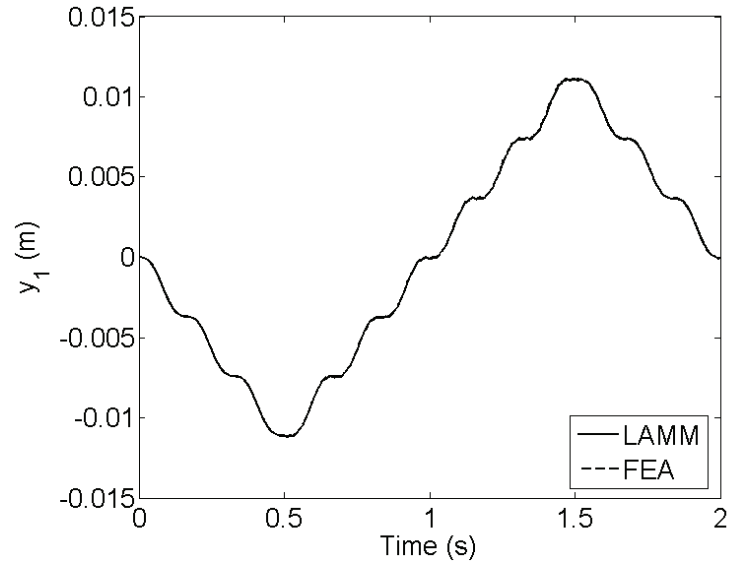
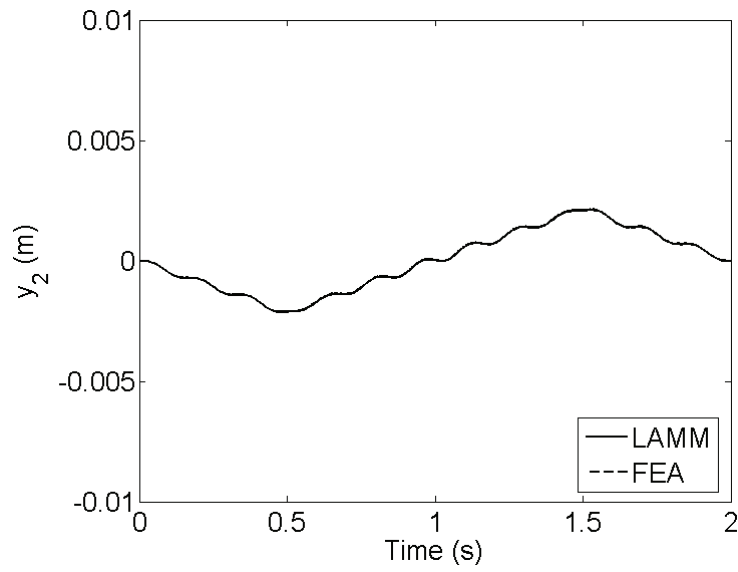Figure AII.12. Deflection of the end of shoulder link ($y_1 = y_{p1}(L_1)$ in Fig. AII.5) for TRLFJ

Figure AII.13. Deflection of the end of shoulder link ($y_2 = y_{p2}(L_2)$ in Fig. AII.5) for TRLFJ